核理研研究報告　第37巻　2004年

ISSN 0385-2105

TOHOKU

RESEARCH REPORT OF LABORATORY OF NUCLEAR SCIENCE

Vol.37　2004

TOHOKU UNIVERSITY

Editors

TAMAE, Tadaaki

OHTSUKI, Tsutomu

HAMA, Hiroyuki

Laboratory of Nuclear Science

Tohoku University

1-2-1 Mikamine, Taihaku, Sendai 982-0826

Japan

Pone: +81, 22-743-3400

Fax: +81, 22-743-3401

Web site: http://www.lns.tohoku.ac.jp/

982-0826 仙台市太白区三神峯1-2-1

東北大学大学院理学研究科

附属原子核理学研究施設

電話 022-743-3400

Fax 022-743-3401

Preface

This issue of Research Report of Laboratory of Nuclear Science reports research activities of the LNS performed in the 2003 academic/fiscal year (April 2003 - March 2004). Major research activities are based on the electron accelerator complex consisting of the 300-MeV LINAC and the 1.2-GeV STB ring. The accelerators have altogether provided a beam time of about 2,800 hours for various experiments through the year.

In this year, the measurement of the C(γ,K^0) reaction with the NKS spectrometer was finished, and that of the D(γ,K^0) reaction has successively started by using GeV tagged photon at the experimental hall 2. The construction of another tagged photon beam line for a new experimental hall (GeV γ-ray experimental hall) was a little bit behind the schedule, and the experiment on (γ,η) reactions by using a new tagging system has finally started at the end of March. The measurements on (e,e'p) and (e,e'α) reactions have also been performed at the experimental hall 2 by using a 200-MeV stretched beam extracted from the STB ring. Also performed were experiments on coherent radiation using a pulsed electron beam below 200 MeV as well as radioactive isotope production.

We hope that this Report will serve as a quick overview of the present LNS activities over a variety of nuclear research fields.

Jirohta KASAGI
Director

Research Report of Laboratory of Nuclear Science
Volume 37, 2004

Contents

核理研研究報告　第37巻　目　次

Ⅰ．原子核物理

Ⅰ. Nuclear Physics

(LNS Experiment : # 2449)

Comparison of the ^{16}O(e, e′p) Cross Section at Low Momentum Transfer with Relativistic Calculations Including MEC

Y. Hayashi[1], T. Tamae[1], K. Abe[2], R. Hashimoto[1], K. Hirose[2], T. Ishikawa[1], H. Kanda[2], O. Konno[3], K. Maeda[2], H. Miyase[2], M. Nanao[1], I. Nishikawa[1], T. Ohtsuki[1], Y. Sato[1], K. Takahashi[2], T. Takahashi[3], H. Tsubota[2], M. Wakamatsu[2], and H. Yamazaki[1].

[1]*Laboratory of Nuclear Science, Tohoku University, Mikamine, Taihaku-ku, Sendai 982-0826*
[2]*Department of Physics, Graduate School of Science, Tohoku University, Aramaki, Aoba-ku, Sendai 980-8578*
[3]*Department of Electrical Engineering, Ichinoseki National College of Technology, Hagiso, Ichinoseki 021-8511*

The (e, e′p_0) cross section of ^{16}O was measured at an energy transfer of 60 MeV and a momentum transfer of 105.2 MeV/*c*, using a 199.53 MeV continuous electron beam. The result is compared with theoretical calculations based on the relativistic distorted-wave impulse approximation (RDWIA). The theoretical values overestimate the experimental ones by a factor of two. The contribution of meson exchange current (MEC) effects is important in the high missing momentum region.

§ 1. Introduction

Recently experiments of the (e, e′p) reaction in the quasi-elastic region and of the (γ, p) reaction above the giant resonance region have been investigated in the relativistic framework [1-3]. The relativistic effects, contribution of meson-exchange currents (MEC), and the choice of the one-body current operator are discussed in the investigations.

In previous reports [4, 5], we compared the reduced cross section obtained from the ^{12}C(e, e′p_0) experiment performed at ω = 60 MeV in the low momentum transfer region with theoretical calculations based on the RDWIA, and found the relativistic calculations overestimate the experimental data by a factor of about two. This enhancement factor is same as that of the ^{12}C(γ, p_0)^{11}B reaction at the same energy. A large contribution of the two-body seagull term was observed at the high missing momentum region.

In order to further investigate the reaction mechanism, we chose ^{16}O as a target of the second experiment, for which the RDWIA is able to give a good and consistent description of (e, e′p) data in the quasi-elastic region and of (γ, p) data [2, 3], different from ^{12}C.

§ 2. Experimental Procedure

The experiment was performed using a 199.53 MeV continuous electron beam from a stretcher-booster ring (STB). Electrons scattered with a 78.5 mg/cm^2-thick beryllium-oxide were analyzed with a large dipole magnetic spectrometer (LDM) at 30°, and detected with a vertical drift chamber (VDC) in the focal plane and three layers of plastic scintillators. A missing energy was set at ω = 61±3 MeV. A

corresponding momentum transfer was 105.2 MeV/c. Ejected protons were measured with SSD counter telescopes composed of three 1mm-thick SSD's at eight angles out of the scattering plane ($\phi_p = 90°$). A 6 mm-thick aluminum disk was installed in front of each telescope, in order to degrade the energy of protons.

The normalization of the cross section was performed from elastic scattering by comparing the result with that of Ref. [6]. We made a measurement at $\theta_e = 62.4°$ using a 199.53 MeV beam. The momentum transfer corresponds to that at 32.0° with a beam energy of 374.5 MeV in Ref. [6].

§ 3. Results and Discussion

The present data are compared with RDWIA calculations [7]. The RDWIA treatment is the same as in Ref. [2, 3]. The bound state wave function is a solution of the relativistic Hartree-Bogoliubov equation using parameters of the set NLSH [8]. The EDAD1 optical potential parameters [9] are used for the scattering wave function. The spectroscopic factor Z(p1/2) = 0.71 has been applied, which was obtained from the analysis of the quasi-elastic (e, e′p_0) reaction [2, 3].

As the choice of the electromagnetic operator is, to some extent, arbitrary and no rigorous justification exists, three current operators (cc1, cc2 and cc3) [2, 3] are used in the calculation in order to assess the effect.

The measured cross section is listed in Table 1. The present data are compared with calculations based on the RDWIA without and with MEC effects in Figs. 1 and 2, respectively. Only the contribution due to the seagull diagram is included in the calculation. In Fig. 1 the calculations are multiplied by 0.35, 0.45 and 0.52 for cc1, cc2, and cc3 one-body currents, respectively, in order to normalize them to the present data at the lowest missing momentum. In Fig. 2 the calculations are multiplied by 0.4, 0.53 and 0.63. These fixed numbers indicate that the calculations overestimate the experimental data by a factor of about 2 at low missing momentum.

Table 1. Differential cross section of the ^{16}O(e, e′p_0) reaction.

θ_p [deg]	p_m [MeV/c]	Cross section [nb/MeV/sr^2]
12	197.27	3.6806 ± 0.1405
24	206.87	2.6170 ± 0.1216
36	221.45	1.1703 ± 0.0578
48	239.49	0.6143 ± 0.0657
60	259.49	0.2392 ± 0.0318
72	280.19	0.0856 ± 0.0344
84	300.59	0.0635 ± 0.0258
96	319.93	0.0558 ± 0.0237

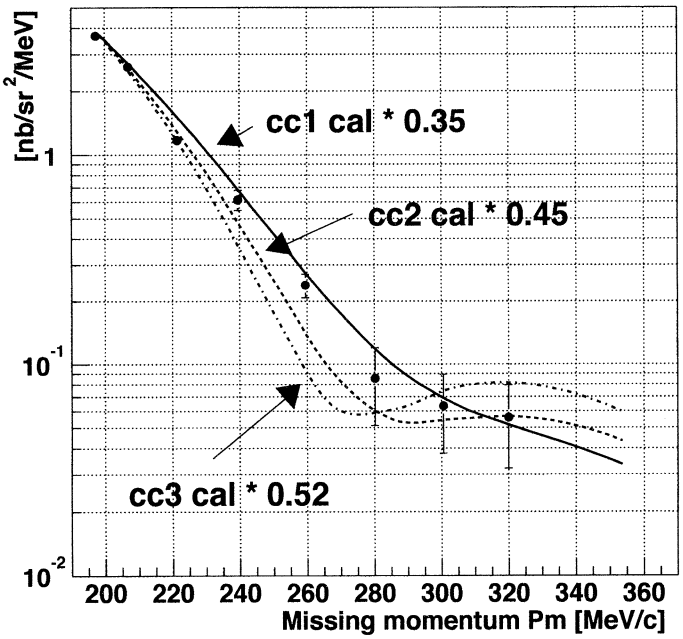

Fig.1. The cross section of the present $^{16}O(e, e'p_0)$ measurement, compared with the RDWIA results calculated without MEC. Closed circles show the results of the present $^{16}O(e, e'p_0)$ experiment. Solid, dashed, and dashed-dotted lines represent the RDWIA results with cc1, cc2, and cc3 prescriptions for the one-body current, respectively. Calculations are multiplied by 0.35, 0.45, and 0.52, respectively.

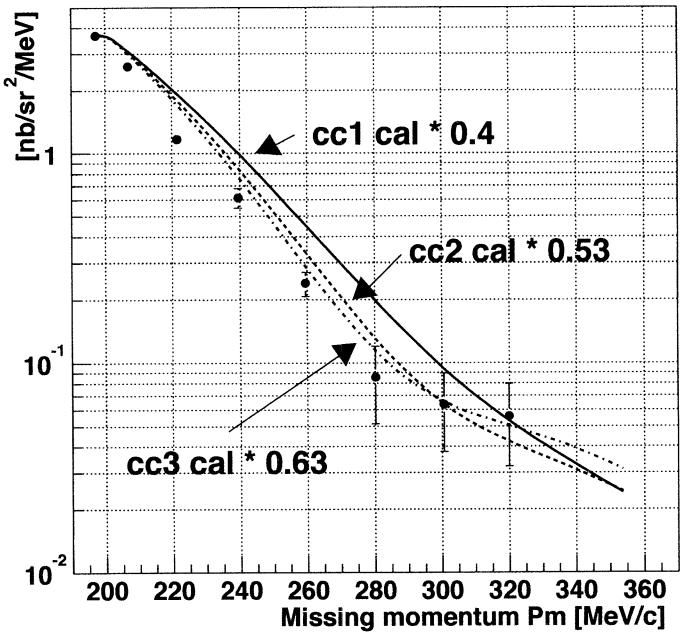

Fig.2. The cross section of the present $^{16}O(e, e'p_0)$ measurement, compared with the RDWIA results calculated with MEC. Closed circles show the results of the present $^{16}O(e, e'p_0)$ experiment. Solid, dashed, and dashed-dotted lines represent the RDWIA results with cc1, cc2, and cc3 prescriptions for the one-body current, respectively. Calculations are multiplied by 0.4, 0.53, and 0.63, respectively.

In Fig. 1 the curves calculated without MEC effects have a bump around 280 MeV/c, which gets larger in order of cc1, cc2 and cc3. The bump shrinks through the contribution due to the seagull term as shown in Fig.2. The effect of the seagull term is contrary to the case of the $^{12}C(e, e'p_0)$ reaction, in which the seagull term enhances the cross section at high missing momentum. The source of the difference is a subject in future studies.

All of calculations with three different one-body current operators (cc1, cc2, cc3) with and without MEC overestimate the experimental data, however, the slope of the calculations with MEC is closer to data than the calculations without MEC. However, we don't assert that the calculations with MEC are correct, because they overestimate the experimental values about twice.

The authors would like to thank C. Giusti and A. Meucci for their relativistic calculations for our data. They also thank the accelerator group, the computer group and Mr. Matsuda for their assistance during the measurement. This work has been supported by Grant-in-Aid for Scientific Research (KAKENHI) (No. 14540239) from Japan Society for the Promotion of Science (JSPS).

References

[1] J.I. Johansson, H. S. Sherif, and G. M. Lotz: Nucl. Phys. **A605** (1996) 517.

[2] A. Meucci, C. Giusti, and F. D. Pacati: Phys. Rev. C **64** (2001) 064615.

[3] A. Meucci, C. Giusti, and F. D. Pacati: Phys. Rev. C **66** (2002) 034610.

[4] Y. Sato *et al.* : Research Report of LNS, Tohoku Univ., **33** (2000) 7.

[5] T. Tamae *et al.* : Research Report of LNS, Tohoku Univ., **36** (2003) 19.

[6] I. Sick and J.S. McCarthy: Nucl. Phys. **A150** (1970) 631.

[7] C. Giusti and A. Meucci: private communication.

[8] M. M. Shaema, M. A. Nagarajan, and P. Ring: Phys. Lett. B **312** (1993) 377.

[9] E. D. Cooper *et al.* : Phys. Rev. C **47** (1993) 297.

(LNS Experiment : # 2375, # 2431)

A Quasi-free Photo-production of Neutral Kaons on ^{12}C in the Threshold Region

T. Takahashi[1a]*, T. Watanabe[1], P. Bydžovský[2], K. Dobashi[1], S. Endo[3], Y. Fujii[1], O. Hashimoto[1], T. Ishikawa[4], K. Itoh[1], H. Kanda[1], M. Katoh[1], T. Kinoshita[4], O. Konno[5], K. Maeda[1], A. Matsumura[1], F. Miyahara[4], H. Miyase[1], T. Miyoshi[1†], K. Mizunuma[1], Y. Miura[1], S.N. Nakamura[1], H. Nomura[1], Y. Okayasu[1], T. Osaka[1], M. Oyamada[1], A. Sasaki[3], T. Satoh[3], H. Shimizu[4], M. Sotona[2], T. Tamae[4], H. Tamura[1], H. Terasawa[4], H. Tsubota[1], K. Tsukada[1], M. Ukai[1], M. Wakamatsu[1], H. Yamauchi[1], and H. Yamazaki[4],

[1]*Department of Physics, Tohoku University, Sendai, 980-8578*
[2]*Nuclear Physics Institute, 25068, Řež, Czech Republic*
[3]*Department of Electrical and Electronic Engineering, Akita University, Akita, 010-8502*
[4]*Laboratory of Nuclear Science, Tohoku University, Sendai, 982-0826*
[5]*Department of Electrical Engineering, Ichinoseki National College of Technology, Ichinoseki, 021-8511*

A quasi-free photo-production of neutral kaons on ^{12}C has been measured in the threshold region. Neutral kaons were identified by the invariant mass of two charged pions after $K_S \to \pi^+\pi^-$ decay outside the target. The obtained cross section is almost the same magnitude as that of K^+. The data are also compared with the calculation using the elementary kaon photo-production model. The results are the first information on $n(\gamma, K^0)\Lambda$ reaction which is necessary to improve the models.

§ 1. Introduction

A strangeness photo-production is interested in recent year in the context with the investigation of the resonances which may couple not with πN but with $K\Lambda$ or $K\Sigma$ channels. Total and differential cross sections as well as hyperon polarizations on $\gamma + p \to K^+ + \Lambda$ and $\gamma + p \to K^+ + \Sigma^0$ were measured with high statistics by SAPHIR collaboration [1]. Theoretical analysis in the framework of the isobar model showed that the observed structure around 1900 MeV is explained well by including a new D_{13} resonance of 1895 MeV [2]. The parameters of this resonance including the existence, however, is not determined yet. S. Janssen *et al.* pointed out that the values of the extracted resonance parameters are strongly influenced by the treatment of background processes, namely, the choice of the meson and

[a] Corresponding author, Tel: + 81-22-217-6424; Fax: + 81-22-217-6455

Email address: toshiyuki. takahashi@kek.jp (T. Takahashi)

*Present address: Institute of Particle and Nuclear Studies (IPNS), High Energy Accelerator Research Organization (KEK), Japan

† Present address: University of Houston, Houston, TX 77204-5506, USA.

hyperon resonances in t- and u-channels, the adopted recipes for the phenomenological hadronic form factors [3]. The CLAS data [4] recently measured at JLab shows a more complex structure around 1900 MeV than that of SAPHIR. No model could explain such behaviors. A lot of new experimental data on such as spin observables and other isospin channels are necessary in order to improve the theoretical models and to obtain the conclusive results on the resonances.

In the viewpoint of the isobar model, the reaction $\gamma + n \rightarrow K^0 + \Lambda$ in the threshold region has following features. (1) Since no charge is involved, t-channel Born term does not contribute. (2) It is a mirror reaction to $\gamma + p \rightarrow K^+ + \Lambda$. A coupling constant, $g_{K\Sigma N}$, changes its sign because of the isospin symmetry, $g_{K^0\Sigma^0 N_n} = -g_{K^0+\Sigma^0 p}$, resulting the different interference effect. This holds for u-channel isovector hyperon resonance exchange terms. (3) Number of resonances to be considered is small in the threshold region. Therefore, this reaction is suitable to investigate the background contribution for the photo-production of strangeness, which is the basis for further investigation of the resonance terms.

In this paper, we present the results of photo-production of neutral kaons on ^{12}C near the threshold. The experiment aims at obtaining the information on $n(\gamma, K^0)\Lambda$ channel using a quasi-free production process.

§ 2. Experiment

The experiment was performed at the internal tagged photon beam facility [6] of Laboratory of Nuclear Science, Tohoku University (LNS). The experimental setup is shown in Fig.1.

The photons with the energy from 0.8 to 1.1 GeV were bombarded to a natural carbon target with the thickness of 12 mm or 2.1 g/cm^2, which was located at the center of the Neutral Kaon Spectrometer (NKS). Photon energy was calibrated with an accuracy within 10 MeV by measuring the momenta of

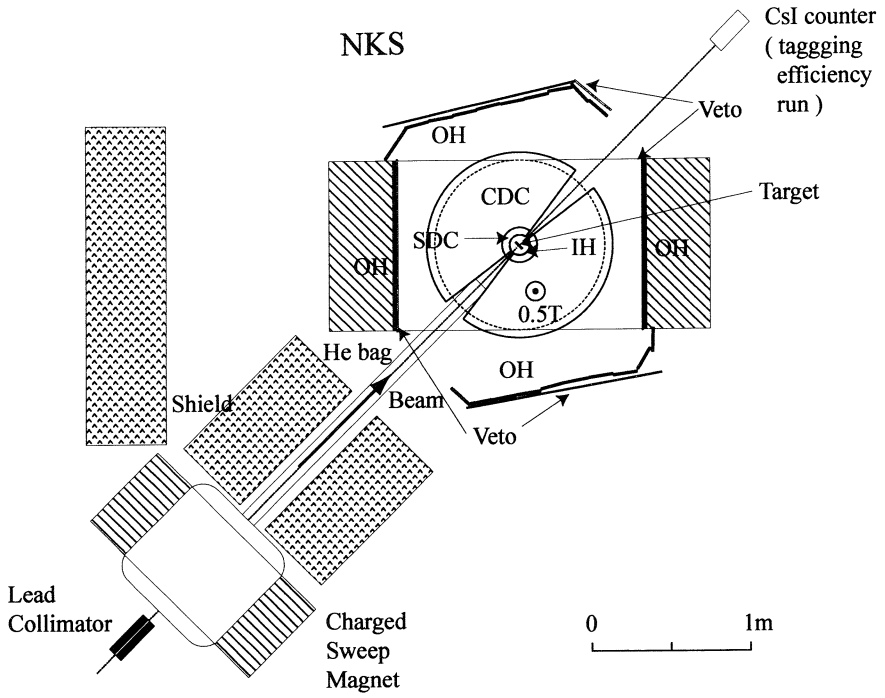

Fig.1. Experimental setup. Photon beam comes from left bottom to right right upper.

the electron-positron pair from the conversion with a pair magnetic spectrometer system. A collimator of 8 mmϕ, which is made of 30 cm-long lead block, was installed in the photon line in order not only to define the beam size but also to eliminate the halo which caused huge backgrounds. Charged particles produced at the extraction window of the accelerator ring or the collimator were swept out by a sweep magnet. The beam line downstream the sweep magnet was filled with helium to reduce the conversion which also caused huge background triggers. The tagging efficiency in this setup was measured to be 80 ± 2 % using a CsI counter located downstream of the NKS in separated runs of low intensity beams. Typical tagged photon intensity was 2.5×10^6 /sec.

Neutral kaons were measured with the NKS by detecting and reconstructing $K_S \rightarrow \pi^+\pi^-$ decay. The NKS was used as TAGX spectrometer [7] at INS-ES. Detector elements are the same as the original TAGX; It comprises a dipole magnet of 107 cmϕ pole and 60 cm gap, straw (SDC) and cylindrical (CDC) drift chambers in the magnetic field of 0.5 Tesla, inner (IH) and outer (OH) plastic scintillator hodoscopes, and veto plastic counters (Veto) in the beam plane. A trajectory projected in the horizontal plane and horizontal momentum of a charged particle was reconstructed by the hits of SDC and CDC using the field map calculated by TOSCA. Time of flight was measured between the IH and the OH, whose distance is about 1m. Each segment of the OH has two phototubes (PMT) at the top and bottom ends. The vertical position was measured from the time difference between two PMT signals.

The vertical direction of the trajectory was calculated by assuming a vertical position at the target was the same as that of the beams. These detectors are separated in two parts against the beam line and cover 25% of whole solid angle. In trigger level, we required more than two charged particles; more than one both in the left and right arms in coincidence with the tagger signal. Since there were many background triggers due to the conversion process occurred along the beam line, veto plastic scintillators of 4 cm height at the beam height were used as veto counters to suppress e^+e^- triggers. Even then, a portion of the background triggers was more than a half of the trigger rates of 100-200 Hz. These background events were due to accidental coincidence between the mis-vetoed NKS trigger and the tagger signal and could be easily rejected by offline analysis.

§ 3. Analysis

Particle identification was done by the reconstructed momentum and velocity. Time of flight resolution was 0.6 ns in rms, which was sufficient to separate pions from protons below 0.7 GeV/*c*, the maximum momentum of the decayed pions in the present kinematics. The e^+e^- events were removed by rejecting the events of which the vertex position was upstream the target.

Figure 2 (a) shows the vertex points of $\pi^+\pi^-$ events. An opening angle (η) cut, $\cos\eta > -0.8$, was applied in order to keep a good vertex resolution. The vertex resolution was estimated to be 1.7 mm. Most of the events were originated in the target area denoted by TG. These events are background events such as a multi-pion production, N^*, and ρ^0. No peak was observed in the invariant mass spectrum for these events as shown in Fig.2 (b). Since K_S has relatively long lifetime of $c\tau$ = 2.68 cm and decays in flight, it is expected to be enhanced by selecting the events of which the vertex were outside the production point, namely, the target region. Figure 2 (c) shows the invariant mass spectrum gated

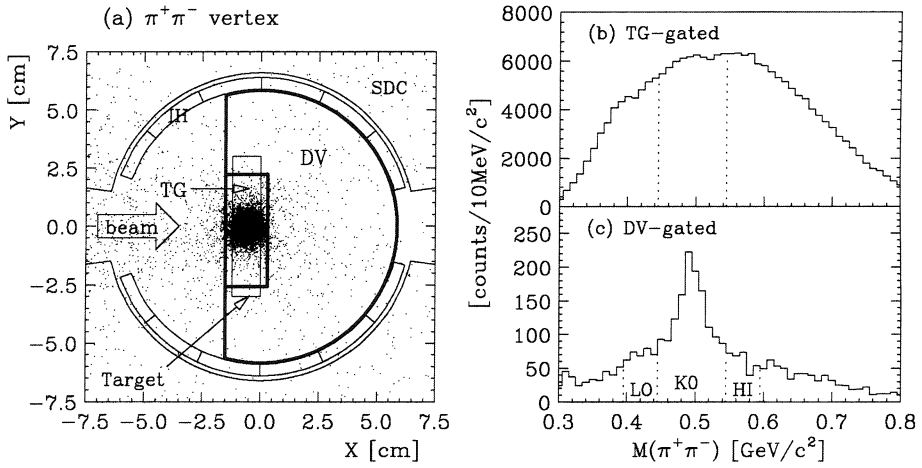

Fig.2. (a) A vertex distribution for $\pi^+\pi^-$ events. The figure is a top view of the target area. Beam comes from left to right (X-axis). The Y-axis means horizontal direction perpendicular to the beam. Events come mainly from the target region denoted by TG. (b) An invariant mass spectrum of $\pi^+\pi^-$ events gated that the vertex is in the target region (TG-gated). (c) An in-variant mass spectrum of $\pi^+\pi^-$ events gated that the vertex is outside the target denoted by DV. The K_S peak is clearly seen.

that the vertex was in the decay volume region (DV), downstream of 4 mm from the target surface. In addition to the vertex position cut, the kinematical consistency between the vertex position and the two-body momentum direction was required in order to reject the events which were not correctly reconstructed. The K_S peak was clearly observed as seen in the figure.

In order to obtain momentum spectra, we defined following three regions in the invariant mass spectrum,

$$\text{K0} : 0.445 : < M(\pi^+\pi^-) < 0.545 \text{ GeV}/c^2,$$
$$\text{LO} : 0.395 : < M(\pi^+\pi^-) < 0.445 \text{ GeV}/c^2,$$
$$\text{HI} : 0.545 : < M(\pi^+\pi^-) < 0.595 \text{ GeV}/c^2.$$

Momentum distributions for K^0 were obtained each in photon energy and angular bins from the K0-gated spectra by subtracting the background contributions. For the background subtraction, we compared following three methods. In the first method, the ratio of the K^0 and background was obtained by fitting the invariant mass spectrum with a Gaussian for K_S and 3rd order polynomial function for the background. The momentum distribution for the background was taken from the spectra gated in LO and HI regions. In the second one, the ratio is the same as that of the first one. But the momentum distribution was taken from the TG-gated spectrum. The third one is more complicated method as follows. Taking into account of the possibility that an uncorrelated π^+ and π^- could be mixed in the DV-gated spectrum by the accidental coincidence, the invariant spectrum was fitted with a Gaussian, the contamination of the target originated spectrum, and the accidental $\pi^+\pi^-$ spectrum. The target originated spectrum was taken from the TG-gated events. The accidental spectrum was made by picking up pions from the different events. According to the fitted coefficients, the momentum spectra

were obtained. The obtained spectra with these three methods agree well each other except for the high momentum region at the forward angle. The difference of the methods is included in errors.

The spectrometer acceptance was calculated by the Monte Carlo simulation code, Geant4 [8], without hadronic interaction processes. In the simulation, the position and time resolutions of the detectors were taken into. Various analysis cut efficiencies were also estimated in the simulation except for the tracking efficiency. The tracking efficiency including the intrinsic and the track-finding algorithm was estimated to be 66% together with the left and right arms using two protons produced events.

The numbers of the irradiated photons were counted with scalers by individual tagger segments. The corrections of the cluster hits and the analysis cuts were performed using the tagger trigger data taken in the same beam condition.

§ 4. Results and Discussion

The obtained momentum spectra of K^0 are shown in Fig.3 (a) - (d). The displayed errors include only statistics, the subtraction of the background, and the uncertainty of the acceptance. In the high momentum region at the forward angle, the errors are large due to the large contribution of the background and the correction with the small acceptance. Angular distributions of the momentum-integrated cross sections are shown in Fig.3 (e) and (f). The integrated momentum range was chosen so as to cover the kinematically allowed region for the quasi-free process, namely, from 0.15 to 0.7 GeV/c for $0.9 < E_\gamma < 1.0$ GeV and from 0.15 to 0.8 GeV/c for $1.0 < E_\gamma < 1.1$ GeV, where 0.15 GeV/c is the detection threshold due to the vertex position cut.

The obtained spectra were compared with the calculations described below. A cross section of the quasi-free kaon photo-production process accompanying with a hyperon (Y) in the laboratory frame is obtained by the incoherent sum of the elementary production process, $\gamma + N \rightarrow K + Y$, with the bound nucleon. Because of the production near the threshold, we do not employ the factorization approximation but treat the two-body kinematics exactly.

$$\frac{d^2\sigma}{d\Omega dp_K} = \frac{1}{(4\pi)^2}\int d\vec{p}_N \rho(\vec{p}_N)\frac{|F(s,t,\tilde{m}_N)|^2}{4p_\gamma \cdot p_N}\times\frac{p^2_K}{E_K E_Y}\delta(E_\gamma+\tilde{E}_N-E_K-E_Y) \quad (1)$$

$$=\int d\vec{p}_N \rho(\vec{p}_N)\frac{d\sigma^*}{d\Omega}(W,\cos\theta^*_{\gamma K},\tilde{m}_N)\frac{p^*_\gamma}{p^*_K}\times\frac{W^2}{p_\gamma \cdot p_N}\frac{p^2_K}{E_K E_Y}\delta(E_\gamma+\tilde{E}_N-E_K-E_Y), \quad (2)$$

where F is the invariant amplitude for the elementary process, p, $\vec{p}$ and p are 4-momentum vector, 3-momentum vector and its magnitude, respectively. The center-of-mass energy of the incoming photon and the bound nucleon is denoted by W. Variables denoted by * are those in the center-of-mass frame of the photon and the nucleon. A momentum distribution of the bound nucleons, $\rho(\vec{p}_N)$, is normalized to an effective proton (Z_{eff}) or neutron (N_{eff}) number of the target nucleus A, by which attenuation effects in the initial photons and the final kaons are taken into. The value of Z_{eff} was obtained to be 4.2 from $^{12}C(\gamma, K^+)$ experiment in the same energy region [9]. We assumed the same value for N_{eff}. The distribution was assumed to be the Fermi gas with k_F = 0.22 GeV/c, for simplicity.

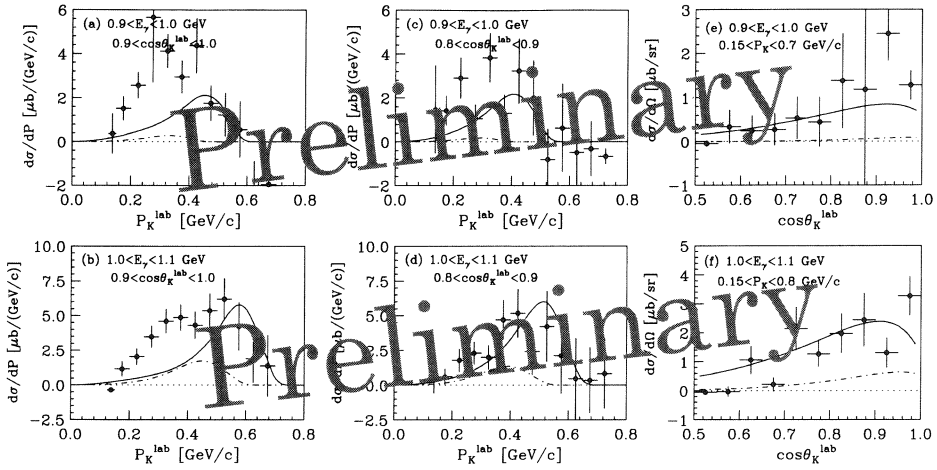

Fig.3. (a) - (d): Momentum spectra for K^0. The integrated photon energy and angular ranges are displayed in the figures. (e) and (f): Angular distributions for momentum-integrated cross sections. The integrated ranges are also displayed in the figures. Data are plotted by closed circles. The error does not include the overall normalization error. Solid curves show calculations using Kaon-MAID (kMAID) [2] elementary amplitude for $n(\gamma, K^0)\Lambda$ reaction, while dot-dashed curves are sum of $n(\gamma, K^0)\Sigma^0$ and $p(\gamma, K^0)\Sigma^+$ processes by kMAID.

Energy and momentum conservations are required not only in the elementary process but also in the total nuclear system.

$$E_\gamma + M_A = E_K + E_Y + E_{A-1}, \tag{3}$$

$$\vec{p}_\gamma = \vec{p}_K + \vec{p}_Y + \vec{p}_{A-1} \tag{4}$$

$$E_{A-1}^2 - P_{A-1}^2 = M_{A-1}^2, \tag{5}$$

where M_A is the mass of the target nucleus, E_{A-1} and $\vec{p}_{A-1}$ are energy and momentum of the residual nucleus of mass M_{A-1}, respectively. Thus, the energy of the initial nucleon is not on-mass-shell but off-mass-shell. Using spectator approximation, $\vec{p}_{A-1} = -\vec{p}_N$, it is written as,

$$\tilde{E}_N = M_A - \sqrt{M_{A-1}^2 + P_N^2} \tag{6}$$

For $K^0\Lambda$ production on ^{12}C, the mass of the bound nucleon decreases by 2.0% at p_n = 0 GeV/c and 5.1% at p_n= 0.22 GeV/c. This mass change makes the two-body center-of-mass energy lower and the kinematical range for integration smaller, resulting smaller cross sections in the threshold region than that from the on-mass-shell approximation, $\tilde{E}_N = E_N = \sqrt{P_N^2 + m_N^2}$, (kinematical off-mass-shell effect). In addition to the kinematical off-mass-shell effect, a dynamical off-mass-shell effect should be considered. The elementary amplitude is constructed from parameters such as coupling constants, resonance's mass and width by Feynman diagram technique. Thus, the change of the nucleon mass leads to the change of the amplitude not only by the s-channel Born term but also by other terms through complicated relations among the kinematical variables.

For the elementary cross sections, the Kaon-MAID (kMAID) model [2] is the only model to predict the $\gamma + n \rightarrow K^0 + \Lambda$ channel so far. Other models have adjustable parameters for $K^0\Lambda$ production,

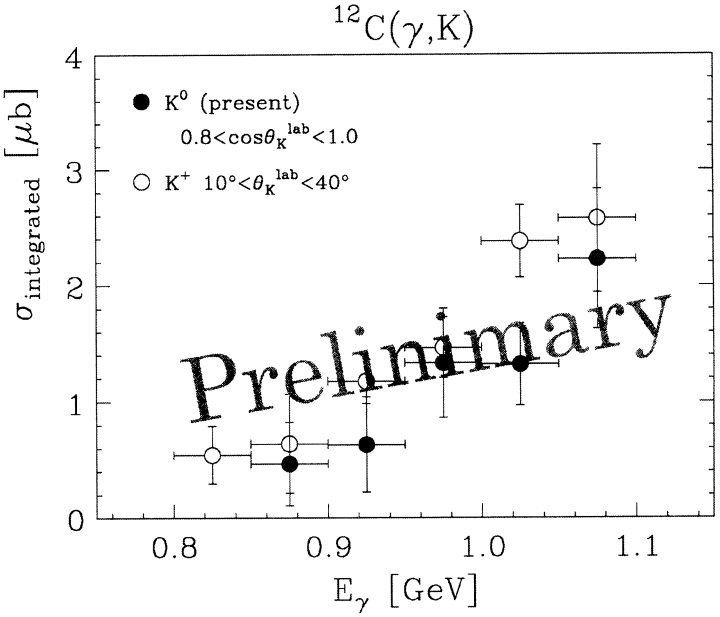

Fig.4. The incident photon energy dependence of the integrated cross sections for the quasi-free kaon photo-production on ^{12}C. Closed circles show the present data for K_0, integrated over the range, $0.8 < \cos\theta_K^{lab} < 1.0$. Open ones show K^+ data integrated from 10° to 40°, which are taken from Ref. [9].

since the ratios of the electromagnetic transition densities between the charged or neutral meson and baryon resonances are unknown. Strictly speaking, kMAID is also ambiguous for $K^0\Lambda$ channel; The transition densities of the D_{13} nucleon resonance, so-called "missing resonance", are unknown. The effect of this resonance, however, is expected to be small in the present case, since the pole energy of the D_{13} is 1895 MeV [2], far from the threshold region. The calculations using the kMAID amplitude are drawn by the solid curves in Fig.3. The calculations reproduce the measured spectra fairly well both in magnitude and shape.

The energy dependence for K^0 photo-production on ^{12}C is shown in Fig.4 together with the K^+ data[9]. The integrated momentum and angular range is displayed in the figure. The cross sections for K^0 and K^+ are almost the same in magnitude.

Finally it is worth to see the contribution of Σ production processes, $\gamma + n \rightarrow K^0 + \Sigma^0$ and $\gamma + p \rightarrow K^0 + \Sigma^+$, since they might affect the obtained spectra sizably. The calculation results are drawn by the dot-dashed curves in Fig.3. In the photon energy less than 1 GeV, the Σ contribution is negligibly small. But in the energy greater than 1 GeV, it is as large as the Λ production. The bump around 0.3 GeV/c in Fig.3 (b) might be due to the Σ productions.

§5. Summary

We measured the $^{12}C(\gamma, K^0)$ reaction at photon energies below 1.1 GeV, by reconstructing $K_S \rightarrow \pi^+ \pi^-$ decay. The cross section is almost the same in magnitude as the of $^{12}C(\gamma, K^+)$. The calculations using the elementary amplitude predicted by Kaon-MAID model reproduces the present data. The present data give the information on $n(\gamma, K^0)\Lambda$ reaction, for the first time, which is necessary to

improve the electromagnetic strangeness production models.

Acknowledgement

The authors thank the scientific and technical staffs of LNS for the operation of the accelerator, various supports of the detector setup, and beam time arrangements. They are grateful to Prof. K. Maruyama and Prof. H. Okuno for their helps to make over the TAGX spectrometer to Tohoku University. They also thank Dr. T. Mart for the useful discussion and offering the program code. This work is supported by Grant-In-Aid for Scientific Research from The Ministry of Education of Japan, Nos. 09304028, 12002001, and 14740150.

References

[1] M. Q. Tran *et al.*: Phys. Lett. B **445** (1998) 20.

[2] T. Mart and C. Bennhold: Phys. Rev. C **61** (2000) 012201(R).

[3] Stijn Janssen, Jan Ryckebusch, Dimitri Debruyne, and Tim Van Cauteren: Phys. Rev. C **65** (2001) 015201.

[4] J.W.C. McNabb *et al.*: nucl-ex/0305028.

[5] R.G. Zegers *et al.*: Phys. Rev. Lett. **91** (2003) 092001.

[6] H. Yamazaki *et al.*: to be published in Nucl. Instr. and Meth. A.

[7] K. Maruyama *et al.*: Nucl. Instr. and Meth. A **376** (1996) 335.

[8] S. Agostinelli *et al.*: Nucl. Instr. and Meth. A **506** (2003) 250.

[9] H. Yamazaki *et al.*: Phys. Rev. C **51** (1995) R1074.

New GeV-γ Beam Line

H. Shimizu[1], T. Ishikawa[1], J. Kasagi[1], T. Kinoshita[1], F. Miyahara[1], T. Nakabayashi[1], M. Nanao[1], K. Okamura[1], Y. Saito[1], K. Sato[1], M. Sengoku[1], K. Suzuki[1], S. Suzuki[1], Y. Tajima[2], T. Takahashi[3], H. Yamazaki[1], and H.Y. Yoshida[2]

[1]*Laboratory of Nuclear Science, Tohoku University, Sendai 982-0826*
[2]*Department of Physics, Yamagata University, Yamagata 990-8560*
[3]*Department of Physics, Tohoku University, Sendai 980-8578*

A new γ beam line has been constructed at Laboratory of Nuclear Science, to deliver a tagged photon beam to GeV-γ Experimental Hall built in the summer of 2002. The photon beam is produced by means of Bremsstrahlung of electrons stored in the 1.2 GeV STB ring. A thin carbon fiber of 11 μm in diameter is employed as an internal radiator which is movable toward the center of the circulating electrons. The beam line starts from the internal radiator placed 303 mm upstream of the entrance of the bending magnet BM5 in the STB ring and ends at the beam dump in GeV-γ Experimental Hall as shown in Fig.l. The total length of the beam line is 23 m from the internal radiator to the beam dump. The energy of Bremsstrahlung photons is tagged with a new tagging system recently installed in the inner vacant space of the C-type BM5 return yoke. The geometry of the beam line is depicted in Fig.2. Two lead collimators are placed on the beam line at the distance of 4.15 m and 12.22 m, respectively, from the internal radiator. The thickness of the first collimator located in Experimental Hall 2 is 200

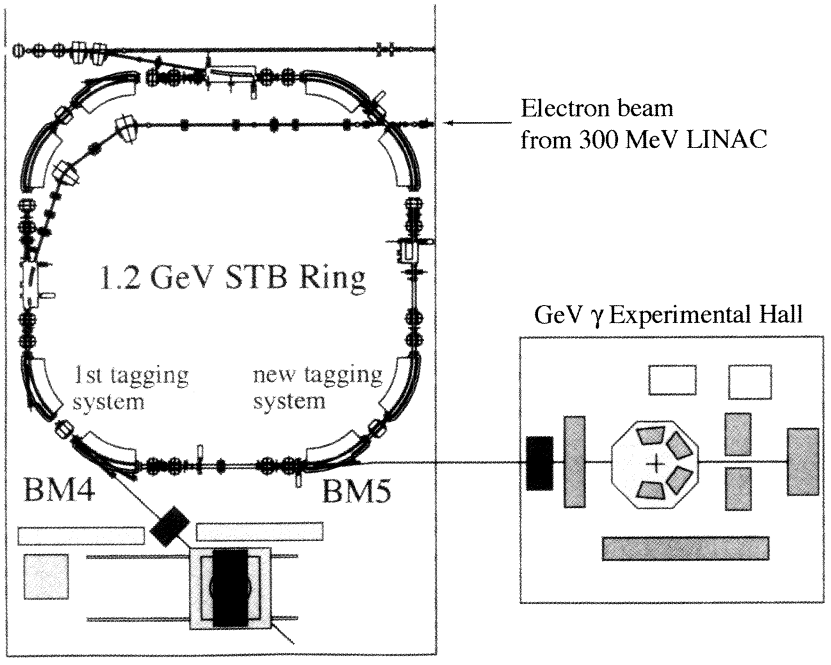

Fig.1. Plan view of the STB ring and GeV-γ Experimental Hall.

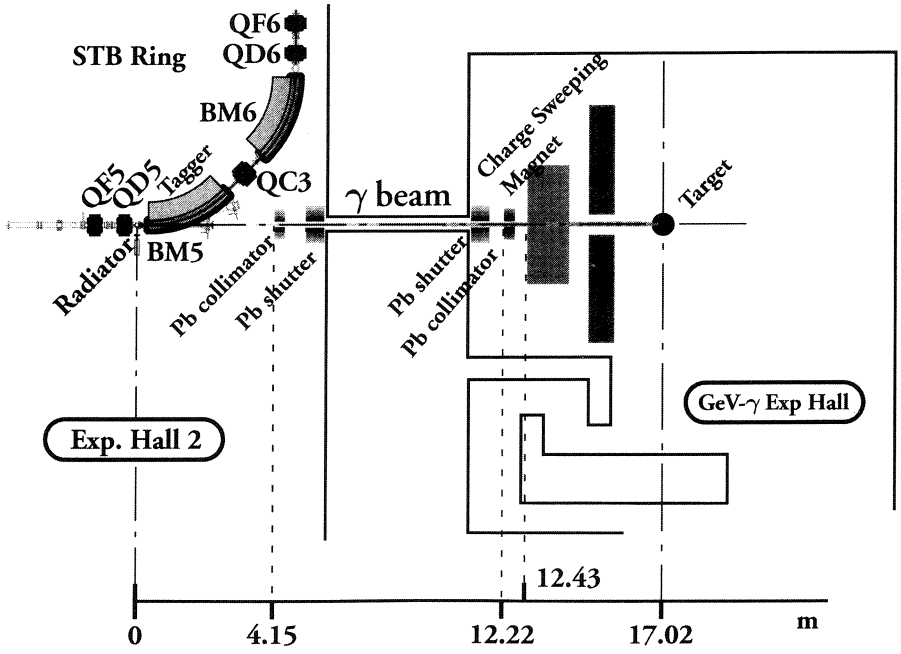

Fig.2. Geometry of the new GeV-γ beam line.

mm, and that of the second one placed in GeV-γ Experimental Hall measures 100 mm. The distance from the radiator to the target is 17.02 m.

The γ beam produced with the internal radiator goes straight through the BM5 magnet and comes out of a 2 mm thick Al window on the end flange of the vacuum duct. Then the γ beam runs 10.3 m in the air from the exit of the vacuum duct of BM5 to the second collimator located at the entrance of GeV-γ Experimental Hall. Just after the second collimator, there is a charge sweeping magnet equipped with a vacuum chamber having a 50 μm thick Mylar window for the γ beam passing through. A vacuum pipe connects the vacuum chamber of the sweeping magnet and the target chamber placed downstream. Therefore the collimated beam runs in a vacuum up to the target. This configuration has been working very well in reducing background events due to the beam itself.

The charge sweeping magnet came from the storeroom at Cyclotron and Radioisotope Center and used to be a switching magnet over there. The size of the return yoke is 1265 mm wide, 760 mm high, and 635 mm long along the beam. The gap of the pole tips has been changed from 40 mm to 60 mm to make things simple at the first stage in the construction of the new beamline. The field strength of the charge sweeping magnet under the present configuration is represented by

$$\int Bdl = 0.52 \text{ [tesla} \cdot \text{ m]}, \tag{1}$$

which corresponds to the bending power

$$\Delta\theta = \frac{0.16}{p} \text{ [rad]} \tag{2}$$

for a charged particle with momentum p (GeV/c).

The intensity of circulating electrons in the STB ring is going down when the internal radiator

starts operation. This happens because the circulating electrons are disturbed by the radiator moving close to the center of the electron orbit. The number of electrons lost by Bremsstrahlung coming about at the radiator is small compared to the case by other disturbance due to the radiator. Most of scattered electrons by the radiator of the thin carbon fiber fade out from the center orbit and sometimes hit the radiator frame, which then becomes another thick radiator for Bremsstrahlung at a wrong place. Therefore the frame of the radiator should be kept far away from the electron orbit as much as possible

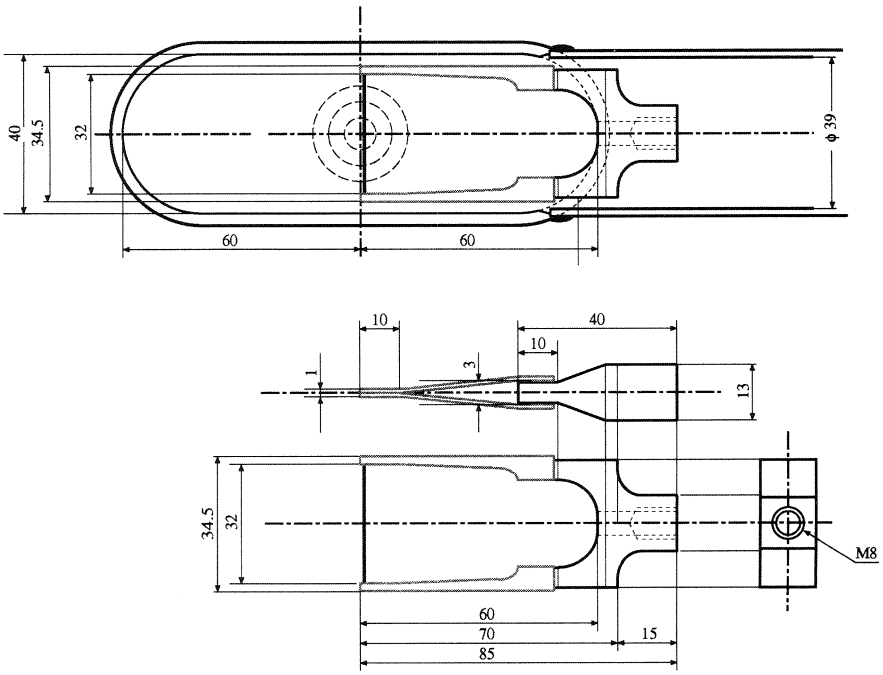

Fig.3. Radiator frame.

and also be made of some light material. Taking this situation into consideration, the radiator frame is designed by improving previously used one at the first tagging station [1]. The carbon fiber of the internal radiator is mounted on the new light Al frame with small tension. The size of the radiator frame is indicated in Fig. 3. The frame itself is drawn in the lower part of the figure. The upper part shows a position of the radiator where Bremsstrahlung takes place, together with the vacuum duct. The internal radiator starts moving just after the electrons are boosted up to the flat top energy, 1.2 GeV, and the moving speed is controlled so as to provide a uniform intensity of the γ beam. This method has been developed at LNS [2].

The transmission rate of the tagged γ beam has been measured with a lead glass counter placed at the beam dump in GeV-γ Experimental Hall. The size of the lead glass is 150 × 150 × 300 mm^3 corresponding to 11.8 radiation lengths along the beam direction. A 5-inch photomultiplier tube, HAMAMATSU R1250, is employed to detect Cherenkov lights due to the electromagnetic showers originated by an incident photon on the lead glass. The beam intensity is reduced in this measurement so that the counting rate of the lead glass counter becomes about 60 kHz with $V_{TH} = -30$ mV. The transmission rate T is defined as

$$T = \frac{N_L \otimes N_T}{N_T} \qquad (3)$$

where N_L and N_T are the number of photons detected with the lead glass at the beam dump and that of tagged photons, respectively. The background events without the radiator are measured independently and are taken into account for N_L and N_T . Intensive work has been made by the accelerator group of LNS to get a beam of good quality and a higher transmission rate [3]. The overall average value of 80 % is obtained for the transmission rate without any collimators, after the function of the STB accelerator has been improved for this purpose. The new GeV-γ beam line is now ready for experiments.

References

[1] K. Hirota *et al.*: Research Report of LNS, Tohoku Univ. **33** (2000) 33.

[2] H. Yamazaki *et al.*: Research Report of LNS, Tohoku Univ. **34** (2001) 22, **36** (2003) 44.

[3] F. Hinode *et al.*: " *Proceedings of the 1st Annual Meeting of Particle Accelerator Society of Japan and the 29th Linear Accelerator Meeting in Japan*", August 4-6, 2004, Funabashi, Japan, p206-208.

Development of a New Tagging System for GeV-γ Beam at LNS

T. Nakabayashi[1], T. Ishikawa[1], J. Kasagi[1], T. Kinoshita[1], F. Miyahara[1], A. Miyamoto[1], K. Okamura[1], Y. Saitou[1], K. Satou[1], M. Sengoku[1], K. Suzuki[1], S. Suzuki[1], Y. Tajima[2], T. Takahashi[3], H. Yamazaki[1], H. Yonemura[1], H.Y. Yoshida[2], and H. Shimizu[1]

[1]*Laboratory of Nuclear Science, Tohoku University, Mikamine, Taihakuku, Sendai 982-0826*
[2]*Department of Physics, Yamagata University, Yamagata 990-8560*
[3]*Department of Physics, Tohoku University, Sendai 980-8578*

We have developed a new tagging system, STB-Tagger II, for the recently constructed GeV-γ beamline at LNS. STB-Tagger II consists of 232 channel scintillating fibers coupled to 29 multi-anode photomultiplier tubes. The tagging system has been installed in the inner vacant space of BM5, one of the C-type bending magnets in the STB ring. An iron fence is employed as a magnetic shield to reduce the strength of the magnetic field in the inner space where the photomultiplier tubes of the tagging system are placed. The energy of the photon beam tagged by STB-Tagger II covers from 0.74 to 1.14 GeV with the RMS energy resolution ranging from 3.5 to 0.5 MeV.

§ 1. Introduction

A series of meson photo-production experiments to study N^* physics has been performed since 2000, using a tagged photon beam at LNS. The in-medium properties of nucleon resonances, especially $S_{11}(1535)$ strongly coupling to the $N\eta$ channel, have been studied via η photo-production at INS [1] and LNS [2]. The elementary process of the H(γ, η) reaction has recently been measured at Mainz [3], GRAAL [4] and JLab [5], and then the $S_{11}(1535)$ resonance parameters have been extracted. On the other hand, there does not exist precise data of the total cross section of the (γ, η) reaction on the deuteron for the incident photon energy covering the whole resonance region. We are preparing for a ^{2}H(γ, η) experiment to study isospin properties, the electromagnetic coupling strength, and resonance parameters of $S_{11}(1535)$ excited from the neutron as well as from the proton.

New GeV-γ Experimental Hall was built in July 2002 at LNS and a GeV-γ beamline was constructed. Then we started developing a new tagging system, STB-Tagger II. We planned the new tagging system having wider energy range, especially in the higher energy side from 740 MeV to 1140 MeV, to cover the $S_{11}(1535)$ resonance region. (The tagging energy range of the existing STB-Tagger I is from 750 MeV up to 1060 MeV [6].) We designed it to be compact so as to install it into the inner space of a dipole magnet in the 1.2 GeV STB ring.

Figure 1 illustrates the experimental setup for GeV-γ experiments. A Bremsstrahlung radiator of a carbon fiber [7,8], 11 μm in diameter, is employed in the STB ring. Circulating electrons at the very

edge of the beam spot strike the radiator. Then Bremsstrahlung takes place and the Bremsstrahlung photons go straight to the GeV-γ Experimental Hall, where the target is placed just 17 m downstream from the radiator. The target is surrounded by the γ detector SCISSORS II.

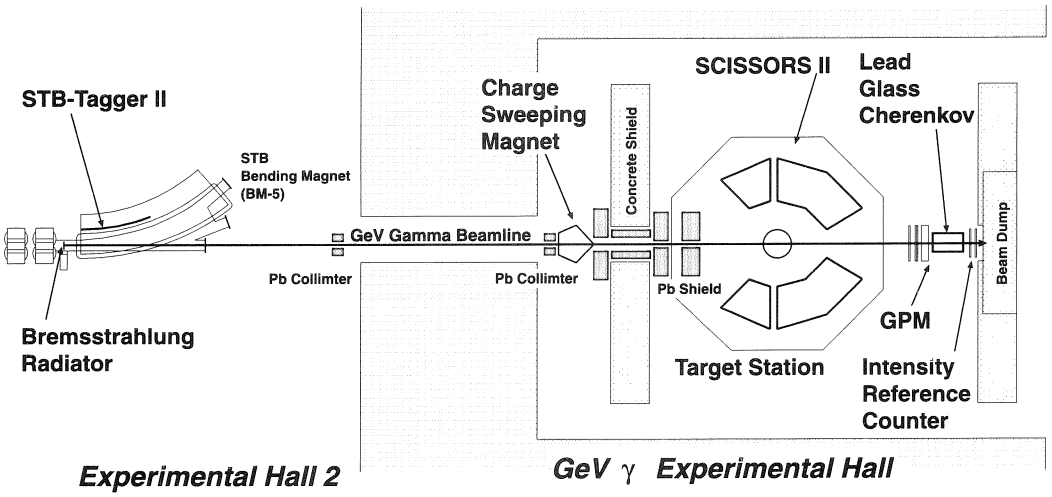

Fig.1. Schematic layout of the GeV-γ beamline and the location of the beamline components.

The recoil electrons traveling 303 mm go into the magnetic field of the dipole magnet and are detected by the STB-Tagger II. The contamination of electromagnetic shower in the tagged photon beam is excluded by a charge sweeping magnet and shielded by lead blocks and concrete walls in the GeV-γ Experimental Hall. The profile of the photon beam is measured by a γ beam profile monitor, GPM [9], which consists of a 16 × 16 scintillating fiber array located downstream of the target station. A lead glass Čerenkov detector is employed behind GPM to measure the transmission rate of the tagged photon beam during the empty target run.

§ 2. Tagging System

The requirements for the STB-Tagger II is as follows:

1. An internal radiator will be used in the 1.2 GeV STB ring to have a Bremsstrahlung beam.
2. The maximum energy of the tagged photon beam should be at least 1.1 GeV, although the background effect due to Möller scattering would not be negligible. Figure 2 shows the differential cross sections of Bremsstrahlung and background Möller scattering and their ratio, which suggests that the background contribution of Möller scattering increases inversely with respect to the energy of recoil electrons. However, the background contribution would be smaller than that indicated in Fig.2. Low energy electrons originated from Möller scattering at the radiator go into the magnetic field of the dipole magnet with some incident angles unlike the case of Bremsstrahlung. Therefore, the Möller scattering effect can be reduced if the direction of recoil electrons is defined as well as possible with tagging counters.
3. One of the dipole magnets in the STB ring is used as a momentum analyzer for recoil electrons of Bremsstrahlung. The detector system must be compact so that the whole tagging system can

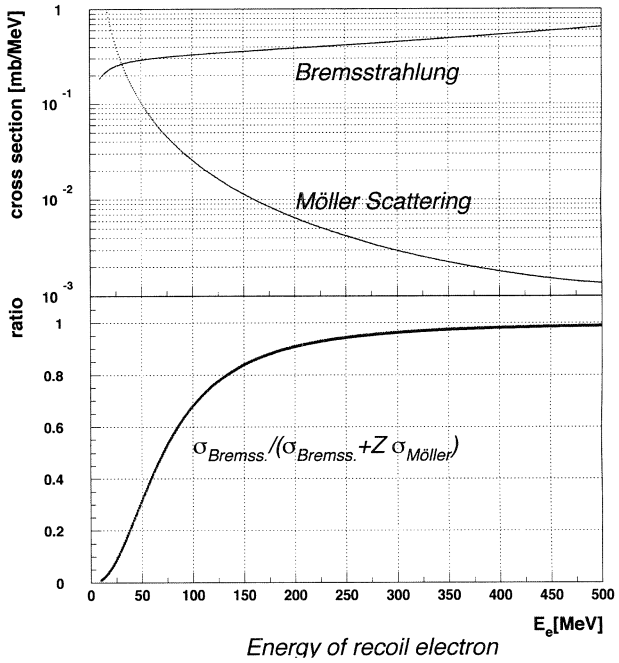

Fig.2. The differential cross sections of Bremsstrahlung [10] and Möller scattering for Z=6 as a function of the recoil electron energy (upper part), and the effect of Möller scattering (lower part).

be installed into the vacant space in the C-type return yoke of the magnet. The space available for the detector setup is 10 cm wide and 35 cm high along the inner curved surface of the return yoke.

4. The tagging counters would be scintillating fibers with photomultiplier tubes, taking into account high counting rates. Moreover, the scintillating fiber should be directly connected to a photomultiplier tube to collect relatively weak scintillation lights efficiently.

5. There are strong magnetic fields around the tagging detector region. Therefore, we need to reduce the leakage flux of the magnetic field up to the level where photomultiplier tubes work well, and/or we must use photomultiplier tubes which have a well magnetic tolerance.

We designed a new tagging system from these considerations.

2.1 Tagging counters

We employ scintillating fibers and multi-anode photomultiplier (MPM) tubes, Hamamatsu H8711-10, as recoil electron counters. It becomes easy by using the MPM tubes to align the fibers efficiently in a narrow space of the C-type dipole magnet. This is one of the reasons why the MPM tube was selected. Figure 3 shows the size of the MPM tube (A) and one unit of the tagging counters (B). The trigger logic diagram is also shown in the same figure (C). The H8711-10 has a rectangular shape of 30 mm × 30 mm × 45 mm and has 16 channel anode outputs. The size of each independent photocathode surface is 4.2 mm × 4.2 mm, which is just fit for scintillating fibers in a rectangular shape of 4 mm × 4 mm × 70 mm. We utilize only 8 channel photocathodes to realize simply four pairs of coincidence signals from corresponding fiber scintillators. Namely, 8 channel fibers are bunched together into a 4 × 2 hodoscope array with 0.5 mm thick partition spacers. The scintillating fibers are directly glued with optical cement to photocathode surfaces without lightguides.

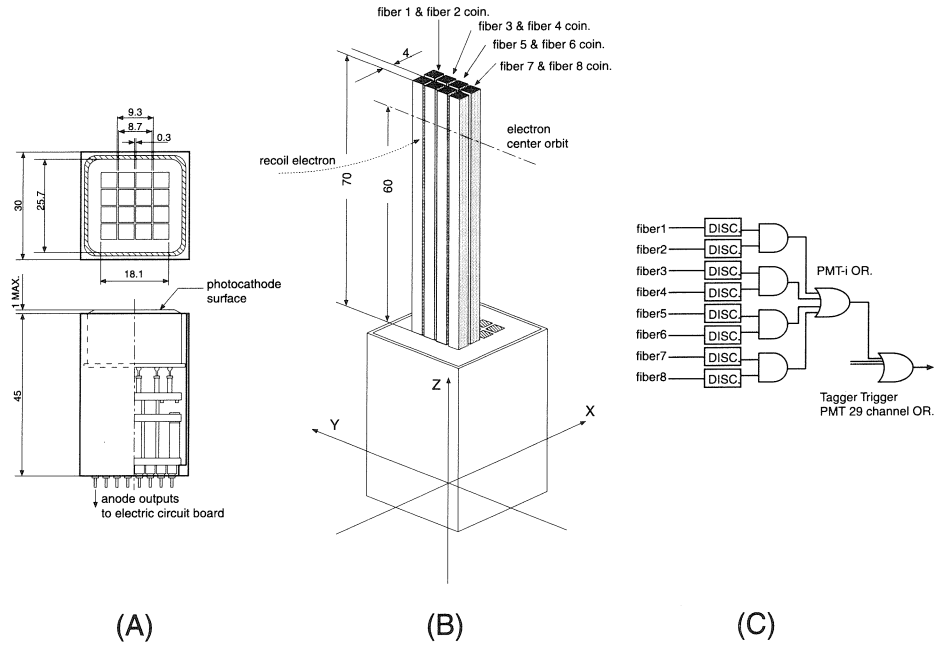

Fig.3. Single scintillator/photomultiplier unit of STB Tagger II. The H8711-10 has 16 channel independent photocathode surfaces (A). The 8 channel scintillating fibers are coupled directly to each photocathode surface with partition spacers of 0.5 mm in thickness (B). The coincidence signals are collected from 29 channel photomultiplier tubes and form the Tagger trigger (C).

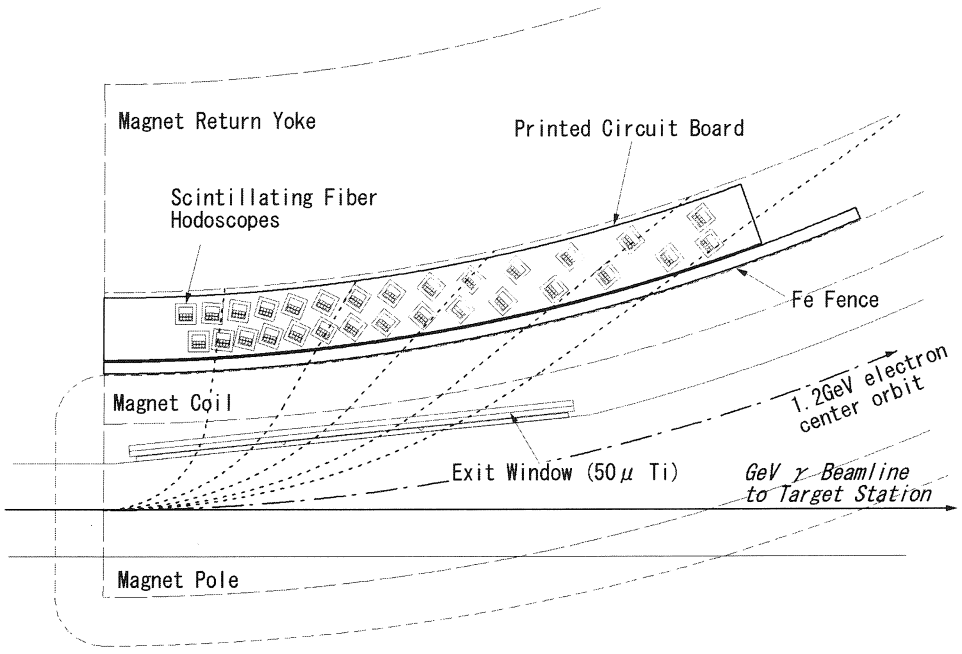

Fig.4. The scintillating fiber allocation of STB-Tagger II.

The 8-channel anode outputs from a single photomultiplier tube are connected to a printed circuit board, which is placed horizontally in such a way that the photocathode surfaces are located 60 mm below from the height of the electron center orbit because the leakage flux of the magnetic field is smaller there. Each MPM tube is placed on the printed circuit board so that recoil electrons from the Bremsstrahlung radiator pass through the $(2i\text{-}1)$-th and the $2i$-th (upstream and downstream) fibers, as

illustrated in Fig.3(B) and (C). The linear output from each fiber is shaped to generate a NIM pulse of 20 ns in width. The coincidence signal of two corresponding fibers, $(2i\text{-}1)$ and $2i$, produces a tagging signal, the width of which is 50 ns. This configuration helps to reduce the background events due to Möller scattering having different passes for low energy recoil electrons. The STB-Tagger II consists of 232 scintillating fibers with 29 MPM tubes. The coincidence signals of 116 channels are used as the tagging signal. A plan view of the whole tagging detectors is illustrated in Fig.4. The Bremsstrahlung photons generated in the internal radiator are delivered to the target station at GeV-γ Experimental Hall. The associated recoil electrons pass through the exit window of 50 μm thick Ti foil of the vacuum chamber and are detected with the scintillating fiber hodoscopes.

2.1.1 Magnetic tolerence of H8711

The new tagging counter system is supposed to be installed where the magnetic field is not negligible. The H8711-10 has 12 layers of metal channel dynodes. The first dynode is located 1 mm away from the photocathode surface and the distance between dynodes is 0.5 mm. The total length of dynode parts is approximately 20 mm. This configuration gives a better magnetic tolerance because of a short electron-cascade length. We have investigated magnetic properties of the H8711-10 with uniform magnetic fields of a dipole magnet. The result indicates that the output is not symmetric around the z-axis. The axes of the magnetic field are defined in Fig.3(B). When the magnetic field of B_x is induced, the relative output for a radioactive source goes down to about 40% at $B_x \simeq 50$ G. On the other hand, with respect to B_y, the relative output decreases more gradually to about 50% at $B_y \simeq 100$ G. It is confirmed that the H8711-10 works very well with no problem in the magnetic field less than 30 G for both x and y directions. We have not measured the z-component dependence because the gap of the magnet we used is smaller than the height of the scintillator/photomultiplier unit. It is reported, however, that the dependence on the z-component of the magnetic field is almost same as that on the x-component. Therefore, we require the leakage flux of the magnetic field should be less than 20 G for the place where the tagging counters is installed.

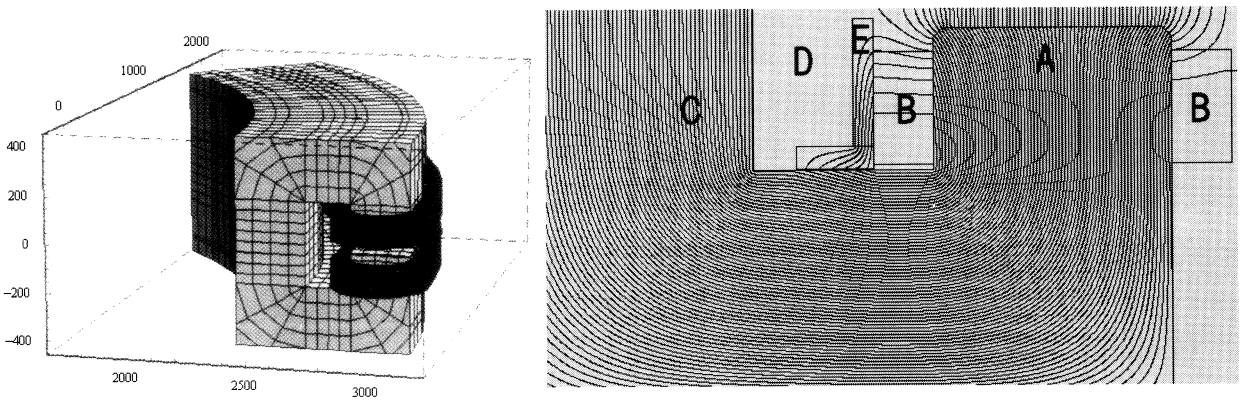

Fig.5. Dipole magnet (left) in the STB ring and its cross sectional view (right). Symbols in the right figure denote, A: pole peace of the magnet, B: coil, C: return yoke, D: detector region, and E: iron fence.

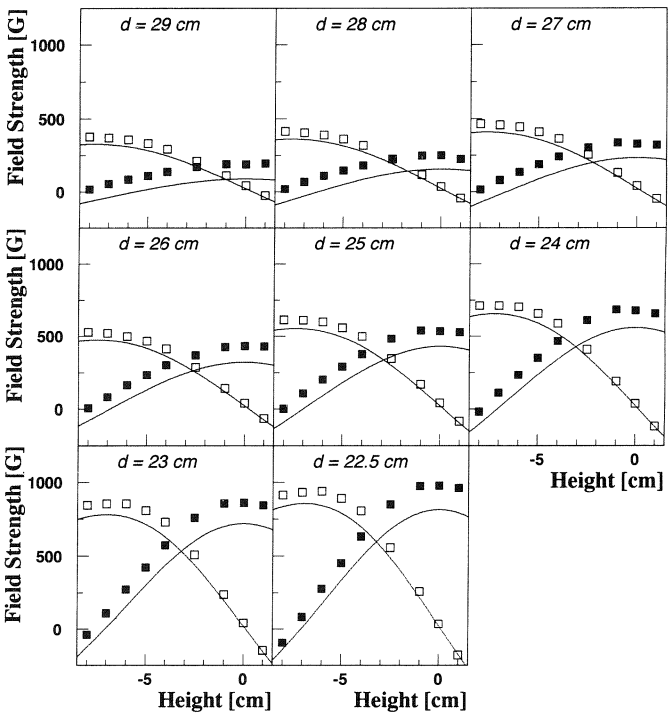

Fig.6. Magnetic field distributions in the detector region without the iron fence. The open (closed) squares indicate the $x(z)$ component of the field and solid lines show the results of the POISSON calculation.

§3. Magnetic Shield

The dipole magnet where the STB-Tagger II is installed is illustrated in Fig.5. A cross sectional view of the lower half of the magnet is also shown in the right side. The MPM tubes are placed in the detector region (D), where the strength of the magnetic field must be less than 20 G.

At first, we measured the distribution of the magnetic field using a Hall gauge around the detector region without any magnetic shield. The result is shown in Fig.6. The measurement was performed for the region from +1 cm to -8 cm along the z direction, the height with respect to the electron beam orbit, and from d = +22.5 cm to d = +29 cm along the x direction which corresponds to the distance from the electron orbit. The closed squares indicate B_z, and open squares denote B_x. These field components are too strong for photomultiplier tubes to work.

Some tests of the magnetic shield were made. A shield box of 5 mm thick iron reduced the leakage flux in the detector region down to $B_x \simeq B_z \simeq$ 150 G, which was, however, still too strong. Then a shield with double boxes of iron was tested, giving a good result of $B_x \simeq$ 20 G and $B_z \simeq$ 15 G, which was acceptable for the operation of the H8711 photomultiplier tube. But the iron shield of the double boxes was a little bit inconvenient in mounting and dismounting the tagging counters with a lot of cables.

We tried to find a simpler shield. In order to design such a shield, field calculations were carried out using a two-dimensional computer code, POISSON. The main components of the field flux giving a great influence upon the tagging detectors can be classified into two parts. The one component is a leakage flux from the yoke due to saturation of the magnetic flux in the iron material. The leakage flux returns to the coil through the minimum path. The other is an extension of the fringe field from the pole piece of the dipole magnet. These two cause strong horizontal and vertical fields where the tagging

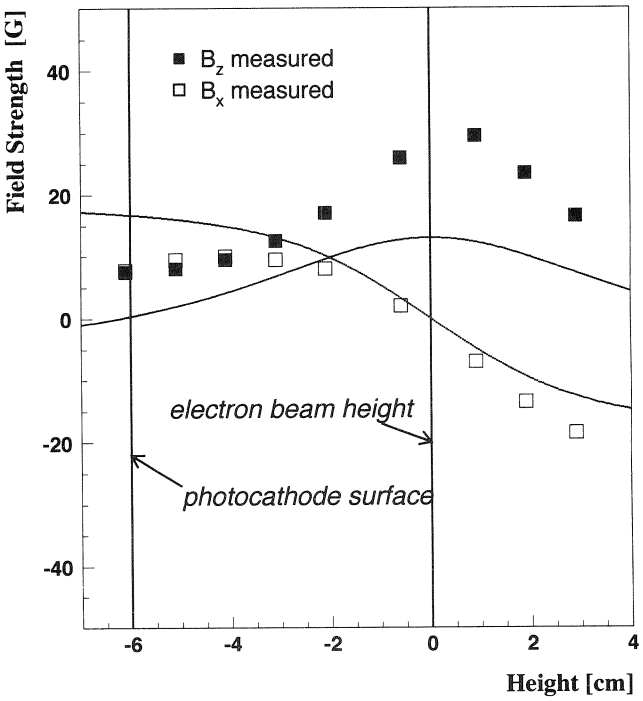

Fig.7. Calulated and measured magnetic fields in the detector region with the iron fence.

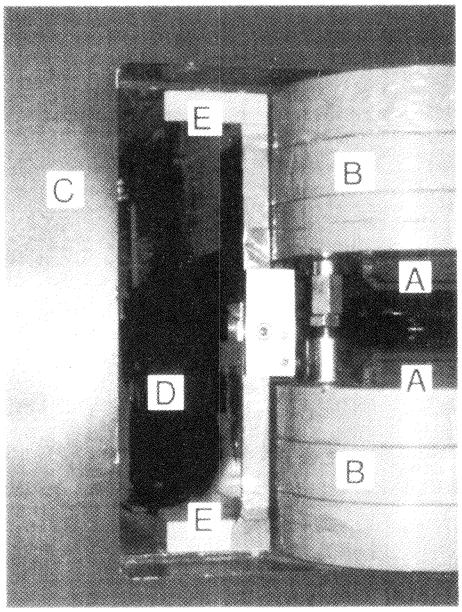

Fig.8. Photograph of the entrance of the dipole magnet equipped with an iron fence. The symbols are same in Fig. 5.

detectors are placed. We employ a thick iron fence which acts like a small return yoke generating a new loop flux around the coil so as to reduce the saturation effect. It can inhale the saturated flux and also screen the strong fringe field from the pole piece. Thus we have optimized the geometry and configuration of iron materials under the condition that (1) the field strength around the photomultiplier tubes should be at most 20 G and (2) the disturbance of the field around the electron center orbit must be less than 0.2%, which is a limit for stable operation of the STB ring. The obtained solution is indicated in Fig.5.

We measured the field map with a Hall gauge and found the field strength reduced from several hundred G to less than 20 G in the detector region. The field strength at the electron orbit went down because of the existence of the iron fence by 0.15% in an average for a 45° bending magnet. It did not give any serious problem for a stable operation of the ring. Consequently, the iron shield of L-type fence, 22mm in thickness, was installed permanently in the inner space of the dipole magnet. Figure 7 plots the field distribution as a function of the vertical direction. The closed (open) squares indicate the measured field B_z (B_x) and the curves are the results of the calculation. Small deviations at most 10 G between measurement and calculation may come from inaccurate inputs for the magnetic permeability of the iron material and from simplicity of the two-dimensional calculation.

Figure 8 shows a photograph viewing the inner space of the C-type dipole magnet equipped with the iron fence. The iron fence is separated to upper and lower parts with a gap of 30 mm. Each part is identical and has the shape of L. The thickness of the vertical fence is 22 mm and that of the horizontal is 24 mm. Brass supports between upper and lower parts are used at both ends of the fence to put the parts together and to push them toward the return yoke to have a good magnetic contact with the yoke.

§4. Operation

4.1 Energy resolution

The tagged photon energy E_γ is determined by

$$E_\gamma = E_0 - E, \tag{1}$$

where E_0 and E are the energy of the circulating electrons and that of the recoil electrons, respectively. The geometrical configuration of the STB Tagger II gives information on the tagging energy and the energy resolution for each pair of the tagging counters.

The tagging range defined by the STB Tagger II is from 0.74 to 1.14 GeV [E_γ= (0.62−0.95) E_0]. However, there are some more factors to be taken into account for the estimation of the effective energy resolution, such as multiple Coulomb scattering at the exit window of Ti foil, and the electron beam emittance in the STB ring. The energy resolution for the photons tagged by the i-th tagging counter is defined as a variance of the recoil electron energies E^i. Namely,

$$\sigma_{E_\gamma^i}{}^2 = \frac{1}{N-1}\sum_{j=1}^{N}(E^i_j - \langle E^i\rangle)^2, \tag{2}$$

where E^i_j means the j-th energy of the recoil electrons detected by the i-th tagging counter and $\langle E^i\rangle$ denotes the mean value of E^i. The estimated energy resolutions are σ_{E_γ}= 3.5 MeV at 0.74 GeV to σ_{E_γ} = 0.5 MeV at 1.14 GeV, respectively.

4.2 Transmission rate of tagged photon

The transmission rate of tagged photons is defined as the ratio of the number of Bremsstrahlung photons to that of recoil electrons detected by the tagging counters. The transmission rate for the i-th tagging counters T^i is obtained as

$$T^i \equiv \frac{N^i_\gamma}{N^i} = \frac{N^i \otimes N^C\,(\text{on}) - N^i \otimes N^C\,(\text{off})}{N^i\,(\text{on}) - N^i\,(\text{off})}, \tag{3}$$

where N^i (on/off) is the gross count of recoil electrons at the i-th tagging counters with the radiator

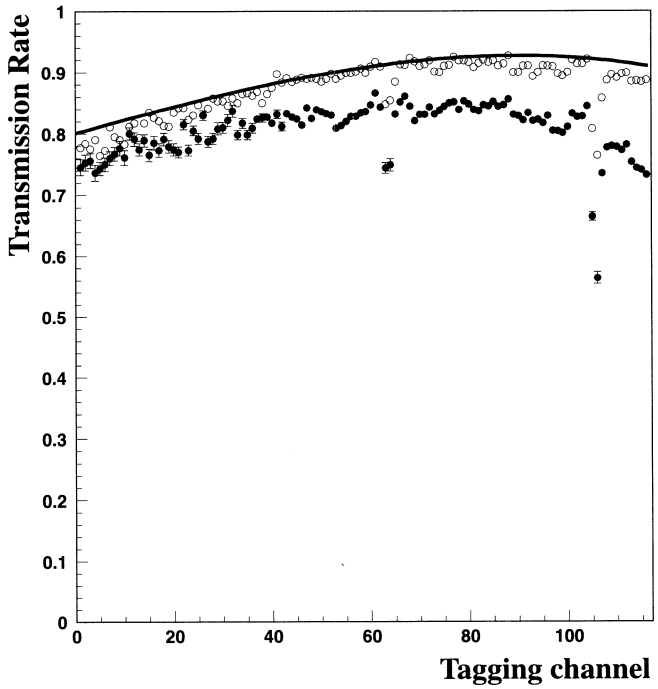

Fig.9. The measured transmission rate of the tagged photons as a function of the tagging channel. The closed (open) circles indicate the result with the lead glass Čerenkov counter set about 20 m (3 m) downstream from the Bremsstrahlung radiator. The solid line denotes a calculation result for the transmission rate at the target.

on/off, and N^C (on/off) denotes the number of photon events. A lead glass Čerenkov detector was employed to detect Bremsstrahlung photons for this purpose. The measurements of the transmission rate were made under two different setups to examine the dependence of the transmission rate on the distance from the radiator. The measured transmission rate is shown in Fig.9, where the closed (open) circles are the result when the lead glass Čerenkov counter was placed about 20 m (3 m) downstream from the radiator. The difference between these two results mainly comes from the attenuation of photons due to the air along the beamline. The solid line shows a calculation result for the transmission rate at the target, including the effect of Möller scattering at the radiator. The effect of Möller scattering reduces the transmission rate, particularly at lower energy side of the tagging channels. The mean value of the transmission rate is found to be about 80% at the target.

§5. Summary

The parameters of the STB Tagger II are summarized in Table 1. The STB-Tagger II consists of 232 scintillating fibers which form a 116 channel hodoscope of tagging counters. The multi-anode photomultiplier tubes are working very well in the vacant space of the magnet with the magnetic shield of an iron fence that reduces the leakage flux around the detector region from several hundred G to ~ 20G. The tagging range of our new tagging system is from 0.74 to 1.14 GeV, and the tagging resolution ranges from 3.5 to 0.5 MeV. We have carried out a performance study of the STB Tagger II with the typical tagged photon intensity of 2×10^6/s. The transmission rate of the tagged photons is about 80%, which has been achieved with dedicated efforts by the accelerator group at LNS.

Table 1. Parameters of STB Tagger II.

Typical Electron Energy (E_0)	1.2 GeV
Tagging Range	$(0.62 - 0.95)E_0$
Tagging Resolution (RMS)	3.5 − 0.5 MeV
Photon Transmission Rate	0.8

References

[1] T. Yorita *et al.*: Phys. Lett. B **476** (2000) 226.

[2] T. Kinoshita *et al.*: Research Report of LNS **34** (2001) 11.

[3] B. Krusche *et al.*: Phys. Rev. Lett.**74** (1995) 3736.

[4] F. Renard *et al.*: Phys. Lett. B **528** (2002) 215.

[5] M. Dugger *et al.*: Phys. Rev. Lett. **89** (2002) 222002.

[6] H. Yamazaki *et al.*: Research Report of LNS **35** (2002) 43.

[7] H. Shimizu *et al.*: in this Research Report of LNS.

[8] K. Hirota *et al.*: Research Report of LNS **33** (2000) 33.

[9] M. Nanao *et al.*: Research Report of LNS **36** (2003) 56.

[10] L.I. Schiff: Phys. Rev. **83** (1951) 252.

(LNS Experiment : #2465)

Development of a Liquid Deuterium Target System for the Neutral Kaon Spectrometer

H. Kanda[1], K. Dobashi[1], S. Endo[2], Y. Fujii[1], O. Hashimoto[1], K. Hirose[1], T. Ishikawa[3], K. Itoh[1], M. Katoh[1], T. Kinoshita[3], T. Kon[1], O. Konno[4], K. Maeda[1], A. Matsumura[1], F. Miyahara[3], H. Miyase[1], T. Miyoshi[1]*, K. Mizunuma[1], Y. Miura[1], S.N. Nakamura[1], H. Nomura[1], Y. Okayasu[1], T. Osaka[1], M. Oyamada[1], A. Sasaki[2], T. Satoh[2], H. Shimizu[3], T. Takahashi[1]†, T. Tamae[3], H. Tamura[1], T. Terasawa[3], H. Tsubota[1], K. Tsukada[1], M. Ukai[1], M. Wakamatsu[1], T. Watanabe[1], H. Yamauchi[1], and H. Yamazaki[3]

[1]*Department of Physics, Tohoku University, Sendai, 980-8578*
[2]*Department of Electrical and Electronic Engineering, Akita University, Akita, 010-8502*
[3]*Laboratory of Nuclear Science, Tohoku University, Sendai, 982-0826*
[4]*Department of Electrical Engineering, Ichinoseki National College of Technology, Ichinoseki, 021-8511*

We have developed a liquid deuterium target system to be used with the Neutral Kaon Spectrometer (NKS). We designed the system with attention to yield, background and safety. For maximizing the K^0 yield, target thickness was optimized and the density of the liquid was kept as high as possible. For minimizing the background, we tried to reduce the amount of material around the target region. For the safety operation, we adopted the LabVIEW on Linux which enabled the remote monitoring and controlling. The target cell is made of aluminum outer shell with a thickness of 1mm and beam windows of 75 μm thick polyimide film. We adopted the carbon fiber reinforced plastic (CFRP) with a thickness of 1.5mm for the material of the wall of the vacuum chamber covering the target cell. We succeeded in suppressing the boiling of the liquid deuterium and keeping the state as long as 2 weeks. The density of the liquid deuterium throughout the beam time in May 2004 was $0.1731\pm0.00007 g/cm^3$ including long term stability and short term fluctuation. The total error of the number of the target is 0.63%, which is much less than the statistical error.

*Present address : University of Houston, Houston, TX 77204-5506, USA

†Present address : Institute of Particle and Nuclear Studies (IPNS), High Energy Accelerator Resarch Organization (KEK), Ibaraki 305-0801

§ 1. Introduction

The study of K^0 photoproduction on the neutron has a unique characteristic, i.e., the reaction does not contain any obvious charge in its participants. The tagged photon with energy from 0.8 GeV to 1.1 GeV at LNS Tohoku is in the energy region of the threshold of $\gamma n \rightarrow K^0\Lambda$ reaction. The reaction in the threshold region is less affected by resonances of the nucleon, so that the mechanism of the strangeness photoproduction can be investigated with less ambiguity. We have developed the NKS spectrometer at LNS Tohoku, for the observation of K^0 from its decay products (π^+, π^-) and performed the measurement of the K^0 photoproduction cross section on carbon.

We have developed a cryogenic deuterium liquefaction system, in order to increase the density from the gaseous phase at room temperature. We use a thick target because we need not to consider the energy loss of a beam and K^0. Moreover, because the K^0 photoproduction cross section is in the order of μb, a thick and dense target and a intense beam are indispensable for the reasonably large statistics.

In designing and testing the target system, we referred to some cryogenic target systems which had been used with the TAGX spectrometer [1] at INS Tanashi, such as a liquid hydrogen target [2,3], a liquid helium-4 target [4], and a liquid helium-3 target [5].

§ 2. Cryostat and Gas Handling

A schematics of the cryostat is shown in Fig.1. The target cell is placed between the pole of the magnet but the refrigerator should be placed outside of the magnet because the space of target region is quite limited. The NKS magnet has a vertical hole with an inner diameter of 120 mm at the center of the yoke and the pole. The long cylindrical part of the cryostat is inserted in the hole. At the top of the cryostat, a 2-Stage Gifford-McMahon refrigerator (Sumitomo Heavy Industry RD-208B) is placed. The ultimate temperatures of the first and the second stage were measured as 9.2 K and 38.1 K, respectively, in the manufacturer's examination. The cooling powers of the two stages are 20 W at 50 K and 8 W at 20 K, respectively. At the second stage of the refrigerator, an oxygen-free copper rod with a diameter of 25 mm and length of 941.5 mm is attached. Two heat exchangers (a condenser and a recondenser) are located at the end of the copper rod. The deuterium gas is supplied from the inlet port and refrigerated down to 40 K in the winding pipe around the 1st stage of the refrigerator. The deuterium is liquefied at the condenser and then drops into the target cell. The recondenser serves for liquefying the evaporated deuterium from the "hot" cell during the liquefaction period and for heat-exchanging of the convecting liquid during the liquid preserving period. The refrigeration power of the 1st stage of the refrigerator is used to cool the thermal shield made of aluminum alloy. The heat transfer to the radiation shield was estimated to be 3.7 W in the condition that the ambient temperature was 300 K, the temperature of the shield was 50 K, and the vacuum of the cryostat is 1.8×10^{-3} Pa. It is sufficiently smaller than the cooling power. The heat transfer to the copper rod was 0.06 W when the temperature of the rod is 18 K in the above condition.

The condenser and the recondenser is temperature-controlled so that deuterium does not solidify. A 50 W heater (LakeShore HTR-50) [6] and a temperature sensor (LakeShore Cernox sensor: CX-1050) are placed on the copper rod. A temperature controller (LakeShore Model 311) is used for feedback

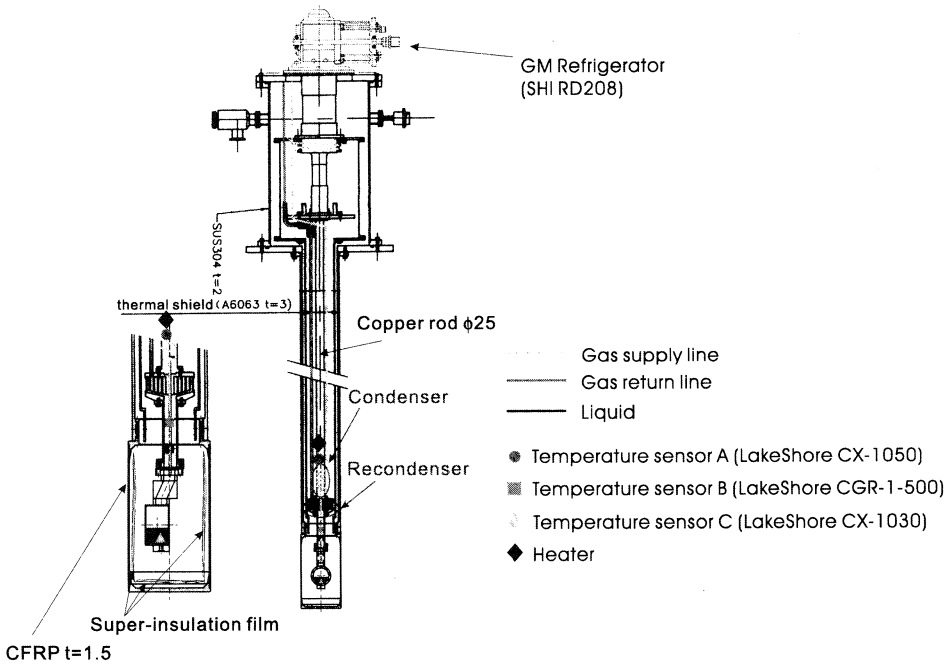

Fig.1. Schematics of the deuterium liquefaction cryostat.

control. Two more temperature sensors are placed to measure the temperature of the gas or the liquid directly. One sensor (LakeShore Carbon-Glass sensor: CGR-1-500) is placed in the pipe between the recondenser and the target cell. The other one (LakeShore CX-1030) is placed in the cell (Figs. 1 and 4). These kind of temperature sensors have low sensitivity to the magnetic field [6,7] and excellent resistance to ionizing radiations [6]. In Fig.2, the schematics of the gas handling system is shown. Positions of the heater and the temperature sensors are also shown in the figure.

The deuterium gas is filled in the buffer tank up to about 110 kPa at room temperature. We connected a cold trap to the gas line for removal of air contamination. Activated charcoal (Kuraray KURARAY-COAL 4GS-261 water washed) is filled in it and refrigerated by liquid nitrogen.

We have developed a monitoring and control system of the cryostat because access into the experimental hall is forbidden during the beam irradiation period. We used RS232C and GP-IB communication ports on all the measuring and controlling instruments. We adopted a distributed I/O system (National Instruments FieldPoint) to unify the operation of valves and the monitoring of pressure gauges. To monitor and control all the instruments, we used National Instruments LabVIEW on Linux. It enables seamless access to the GP-IB and RS232C instruments and easy development of graphical monitoring/controlling panels. Moreover, we can easily set network accessibility to the program because it works on the X11 protocol. The schematics of the remote monitoring and controlling system are shown in Fig.3 [8].

Because the deuterium is a flammable gas with flammability limits in air (STP conditions) range from 6.6 to 79.6 vol% [9], we paid attention to the safety in the treatment of the deuterium gas. We set a gas leak detector (New Cosmos XP-703D) with sensitivity of 1.0 ppm for H_2, near the gas handling system. We adopted air-operating valves in the deuterium gas lines to reduce the danger of explosion.

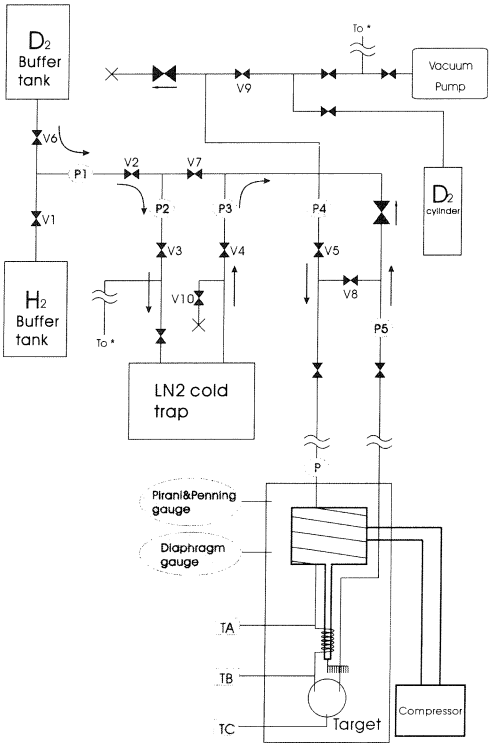

Fig.2. Schematics of gas lines.

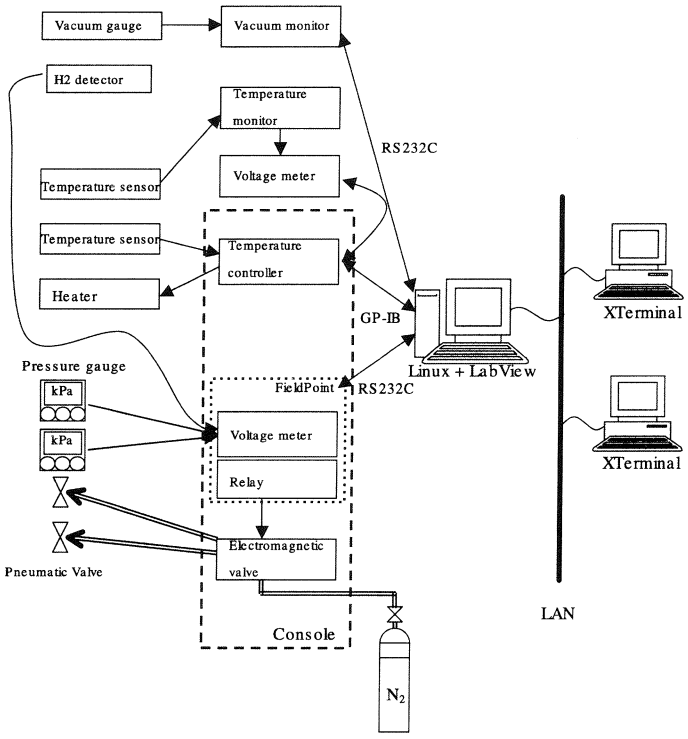

Fig.3. Schematics of the monitor and controlling system.

The target elevator was developed by modifying a hand lifter and settled on the top of the yoke of the spectrometer magnet. The cryostat was attached on the target elevator, and placed so that the axis of the cell is at the center of the magnet. The precision of the target installation on the center of the

beam was 1 mm. All the parts inside the cryostat shrink when they are at low temperature. We calculated the shrinking length as 6.42 ± 0.25 mm from the coefficients of thermal expansion and sizes of the parts. The error contains uncertainties of thermal expansion coefficients, temperature distributions, and sizes of the parts. The total precision of the target alignment was σ ~1.1 mm.

§ 3. Target Region

We made a great effort to the design and development of the target region. It is crucial to optimize contradictory conditions.

3.1 Shape of the target and the K^0 decay volume

Because of electromagnetic and hadronic background, it is almost impossible to find K^0 decay vertices inside the target cell. We require one vertex of two charged particles outside the target cell and inside the wall of the cryostat. We call the region as the K^0 decay volume. (see Fig.6(a)). The target thickness and the amount of K^0 decay volume are in the relation of trade-off. From one dimensional calculation (Fig.4), we estimated the optimum thickness of the target to be 30 mm. In order to minimize the uncertainty of the target thickness caused by the fluctuation of beam position, the curvature of the target window should be minimized. We have developed a cylindrical cell with the axis parallel to the beam (Fig.5). The cylindrical part (outer shell) of the cell was made of aluminum of 1 mm thickness for sufficiently high pressure resistance. The diameter of the beam window of the cell is 40 mm and the outer diameter of the cell is 50 mm (see Fig.5). The windows of the cell where the γ beam passes through were made of thin plastic films to reduce an electromagnetic background from the passage of the intense γ beam. We tested many kinds of super engineering plastics and adhesives for their pressure resistance at room temperature and at liquid nitrogen temperature[10]. We decided to adopt a polyimide film: Ube Industries' Upilex-S of 75 μm thickness[11], which was adhered to the aluminum shell by Stycast 1266 [12]. The maximum bursting pressure of the cell was beyond 1100 kPa at room temperature and 400 kPa at liquid nitrogen temperature. The window swells due to the pressure of the deuterium gas. We measured the pressure dependence and shape of the swelling displacement at room temperature. From the measurement, we found that the shape was sphericel and the elastic modulus of the film was 5.6 GPa and the Poisson's ratio was 0.31. We also found the individual difference of the

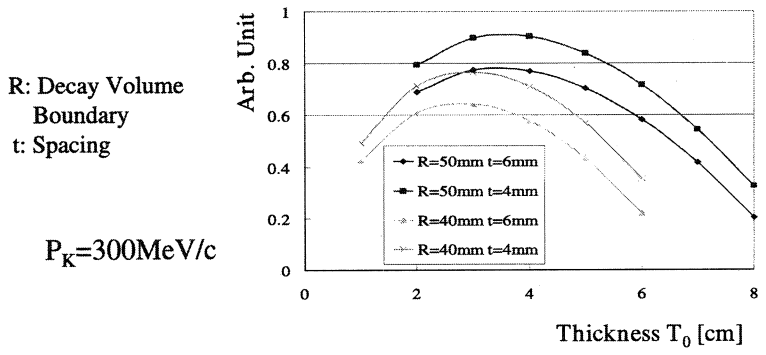

Fig.4. Yield of K^0 with various conditions on one-dimensional K^0 decay model. R is the radius of the vacuum chamber and t is the spacing between the target and the decay volume.

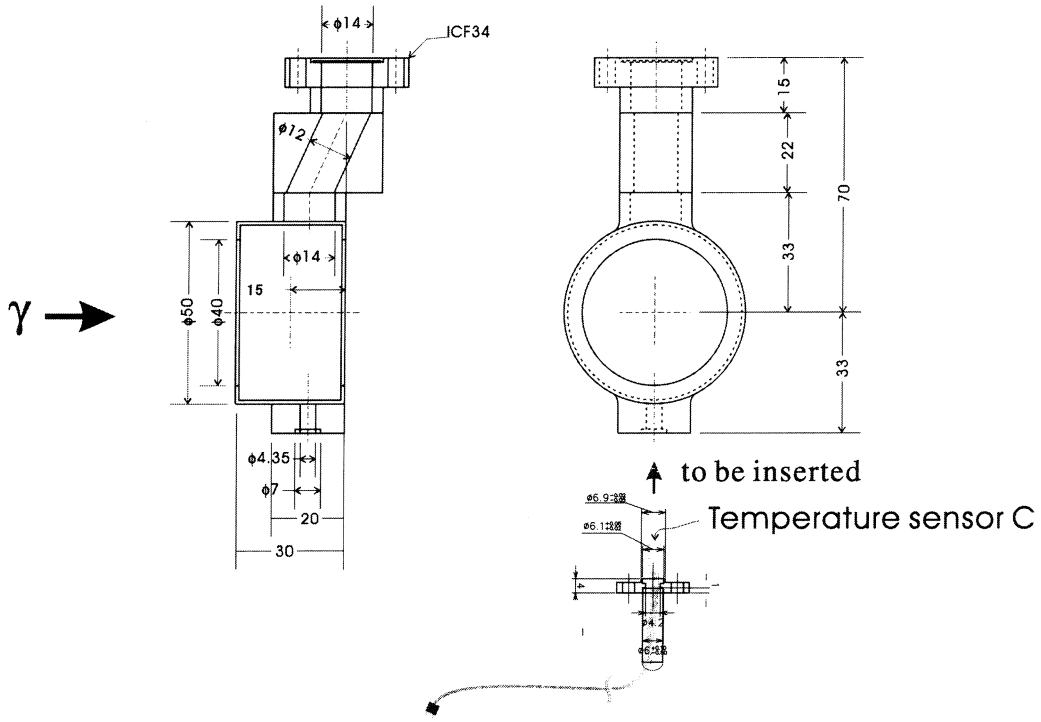

Fig.5. Schematics of the target cell. The ICF flange is used to couple the cell to the gas line. The temperature sensor C is fastened to a small flange to detach from a cell and to attach to another one.

maximum swelling displacement was 0.14 mm.

In order to estimate the swelling shape at 20 K, we used a finite element calculation program (Marc/Mentat) at Tohoku University Information Synergy Center. It is known that the elastic modulus of plastic becomes larger at cryogenic temperature than at room temperature [13,14]. The measured elastic modulus of 50 μm thick Upilex-S film was 9.3 GPa at room temperature and 12 GPa at liquid nitrogen temperature[15]. We assumed the elastic modulus of the film at 20 K is between 5.6 GPa and 12 GPa. The calculated maximum swelling displacements for various conditions are in Table 1. From these results, the possible maximum swelling displacement was 1.59 mm when the target cell was filled with the liquid deuterium. (P=50 kPa) The error of the swelling displacement was estimated to be 0.25 mm, which includes pressure ambiguity (0.02 mm), uncertainty of the elastic modulus (0.20 mm) and individual differences due to the adhesion of the films (0.14 mm). The target thickness at the center of

Table 1. The maximum swelling displacements of a 75 μm thick film in various conditions calculated with the finite element method.

Pressure	E=5.6 GPa	E=12 GPa	Mean
30 kPa	1.48 mm	1.16 mm	1.32 mm
50 kPa	1.78 mm	1.39 mm	1.59 mm
100 kPa	2.28 mm	1.74 mm	1.99 mm

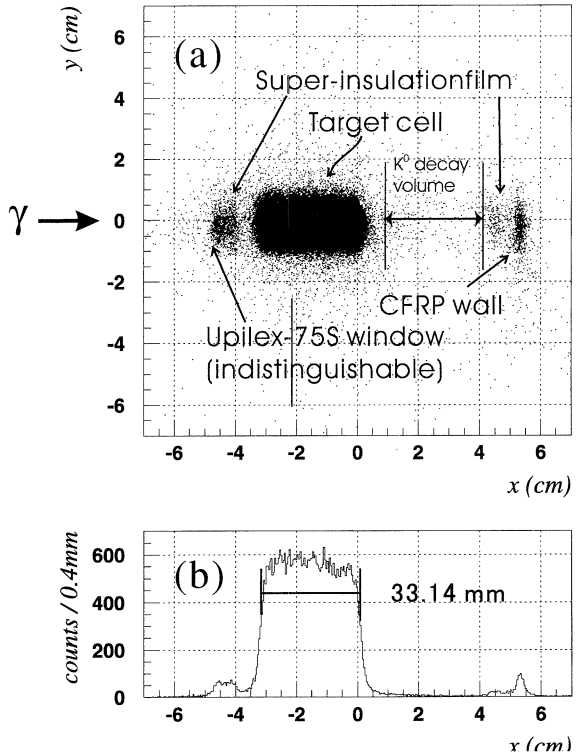

Fig.6. Distribution of reconstructed vertex in 3 charged tracks. (a) is the projection on the *xy* plane. Matters along the beam axis are visible. (b) is the projection on the *x* axis. Thickness of the target was measured as 33.14 mm.

the cell was estimated to be 33.18 ± 0.45 mm. We measured the thickness of the target from the vertices of charged particles (Fig.6). The mean value of 3 measured target thicknesses in the beam times in 2003 was 33.14 ± 0.18 mm, which was consistent with the calculated value. A weighted average of these 2 values was 33.15 ± 0.18 mm. The error of the thickness was 0.55%. We also estimated the error of the number of the neutron target due to the uncertainty of the position of the beam spot. The fluctuation of the number of the target was 0.3% at 3 mm displacement of axes of the beam, assuming the profile of the γ beam was Gaussian with $\sigma = 5$ mm, and the swelling displacement of the window was 2 mm [8]. Because the precision of target alignment was estimated to be 1.1 mm, the error in the number of the target was less than 0.3%.

3.2 Vacuum chamber covering the target cell

We detect charged pions from the decay of K^0 in the decay volume. They pass through the wall of the cryostat and suffer multiple scattering and energy loss. Though it should be strong enough to endure the pressure difference inside and outside, its thickness should be as small as possible. The mechanical properties of various materials for the wall of the cylindrical vacuum chamber are summarized in Table 2. The minimum thicknesses of the cylindrical chamber are also listed in the table. We calculated the minimum thicknesses from the equation of buckling strength for cylindrical shells:

$$\Delta P = \frac{E}{4\,(1-\sigma^2)}\left(\frac{t}{r}\right)^3,$$

where ΔP = 250 kPa and r = 50 mm [3]. We adopted the carbon fiber reinforced plastic (CFRP) for the

Table 2. Comparison of strength and thickness of the vacuum chamber of various material.

Material	Elastic modulus E [GPa]	Poisson's ratio σ	Thickness t [mm]	Radiation Length $[X_0]$
Aluminum	69	0.3	1.2	13×10^{-3}
SUS 304	206	0.3	0.82	46×10^{-3}
CFRP	137	0.26	0.95	3.5×10^{-3}

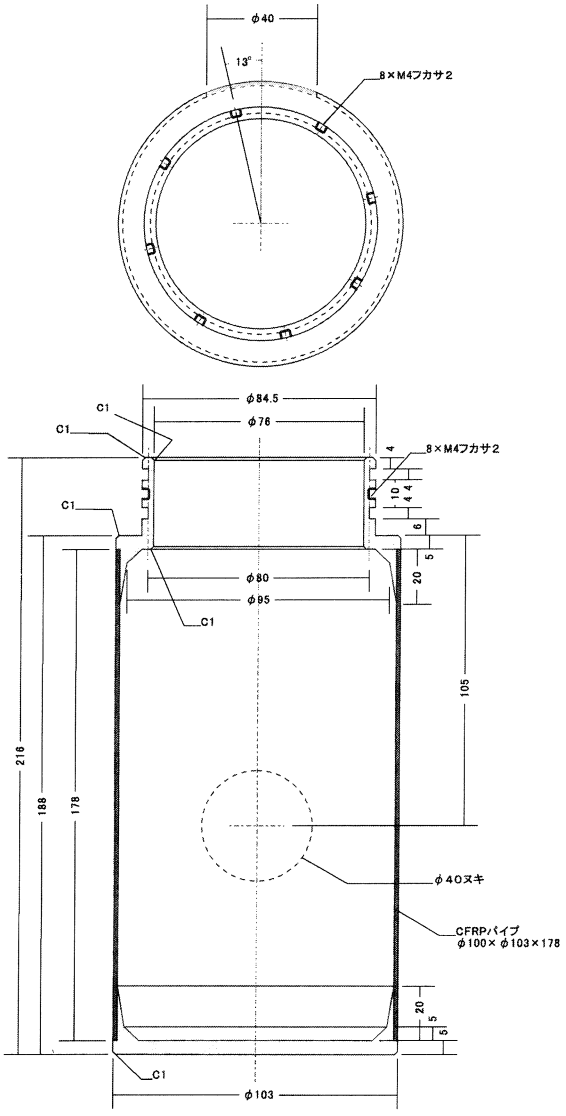

Fig.7. Schematics of the vacuum chamber at the target region.

material of the vacuum chamber covering the target cell (Fig.7). Though the thicknesses of the CFRP vacuum chamber was 1.5 mm for avoiding the air leak, the radiation was still $5.5 \times 10^{-3} X_0$. We made a beam window on the CFRP cylinder for further reduction of the background. A 75 μm thick Upilex-S film was adhered on the window.

The CFRP has an advantage in strength but a disadvantage in the large emissivity of the thermal radiation. The emissivity of the CFRP is almost 1.0 while those of the aluminum and SUS are less then 0.1. In order to suppress the thermal radiation, we adopted 10 layers of super-insulation film (corrugated aluminized mylar of 6 μ m thickness). By using 10 mid planes, the heat transfer between 2 parallel planes is reduced down to 1/11 of the one without mid planes, assuming emissivities of all the planes are the same [14]. However, our insulators were cylindrical and mutually contacting, insulation effect should be smaller than in the ideal condition. Without the super insulation the power of the thermal radiation on the target cell was calculated to be 1.2 W. We estimated the power of the thermal radiation on the target cell with super insulation films as 0.23 W assuming the inner surface of the vacuum chamber was aluminum and no insulation layers were present [8].

§ 4. Operation

The phase diagram and density of deuterium is shown in Fig.8. In the liquefaction period, we first set the temperature of the condenser to 19 K which was 0.3 K above the melting point of deuterium and then let the deuterium gas flow into the cryostat. Liquefaction of the deuterium gas naturally stopped after the cell, the condenser, and the recondenser were filled with the liquid deuterium. When the liquefaction stopped, the temperature of the liquid measured by the C sensor (see Fig.1) was ~22 K and the pressure was ~50 kPa, which means the liquid was boiling (on the saturation curve) as can be seen in Fig.9(c). The temperature of the condenser and the recondenser was carefully set down to 18.0 K, which was 0.7 K below the melting point. Then the temperature of the liquid gradually descended to 19 K. By keeping the temperature of the condenser and the recondenser at 18 K, the temperature of the

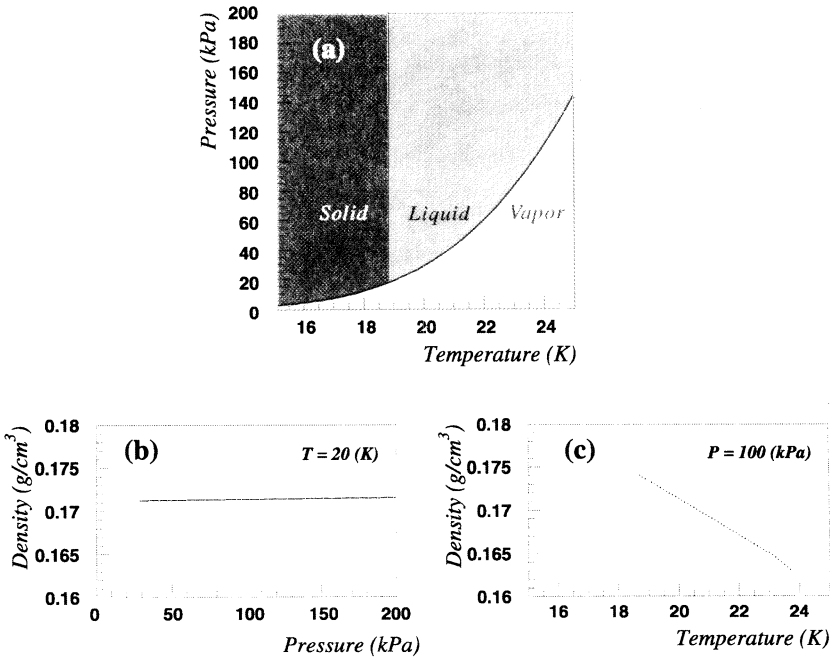

Fig.8. The properties of deuterium. (a) is the phase diagram. (b) is the pressure dependence of the compressed liquid deuterium density at 20 K. (c) is the temperature dependence of the compressed liquid deuterium density at 100 kPa.

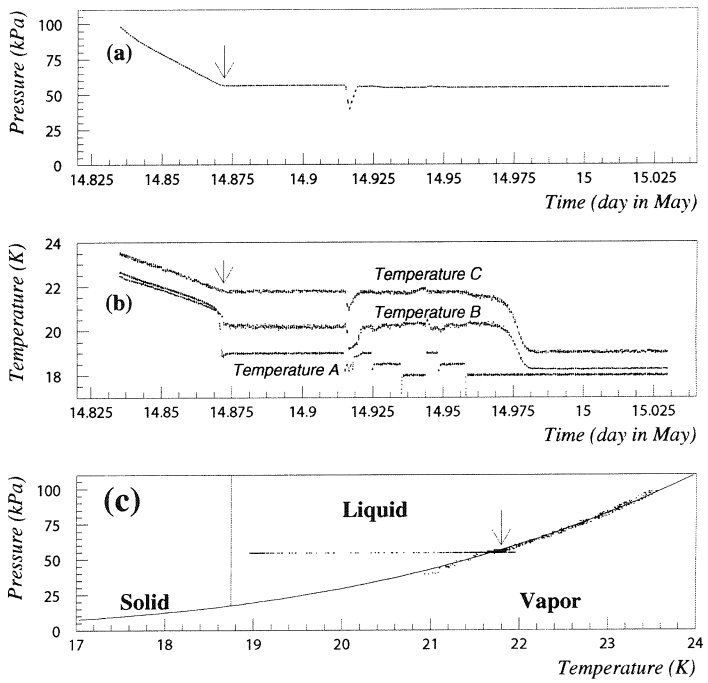

Fig.9. The status of the deuterium in the liquefaction phase. (a) is the pressure of the cell. (b) is the temperature measured by 3 temperature sensors and the set point of the condenser. (c) is the phase diagram. At the arrow point, the liquefaction completes. After changing the set point tempereture to 18 K, the tempereture of the liquid gradually goes down to ~ 19 K.

liquid could be kept for more than 2 weeks. The time course of the density and the histogram of the density is shown in Fig.10. The average density through the beam time in May 2004 was 0.1731 g/cm^3. As seen in Fig.10(a), the liguid density showed two components of fluctuation: a slow drift and a fluctuation in each measurement. These fluctuations were caused both by real temperature fluctuation and by electrical noise in measuring the temperature by the electrical resistance of the sensing substance. The total error of the liguid density was 4×10^{-4}.

The target system was also used as the liquid hydrogen target for the double pion photoproduction (LNS Experiment #2464). In the case of hydrogen, the liquefaction and the decent of liquid temperature could be realized by setting the temperature of the condenser and the recondenser 0.7 K lower than the melting point. Through 2 weeks of beam time, the density of the liquid hydrogen was 0.07671± 0.00003 g/cm^3.

§ 5. Summary

We have developed a cryogenic liquid deuterium target system. The LabVIEW on Linux enabled us of the remote monitoring and controlling. The outer shell of the target cell is made of aluminum with thickness of 1 mm. The beam window of the cell is 75 μ m thick Upilex-S film adhered on the shell with Stycast 1266 epoxy resin. The vacuum chamber covering the target cell was made of the CFRP with a thickness of 1.5 mm. We succeeded in suppressing the boiling of the liquid deuterium and keeping the state as long as 2 weeks. The density of the liquid deuterium throughout the beam time in May 2004

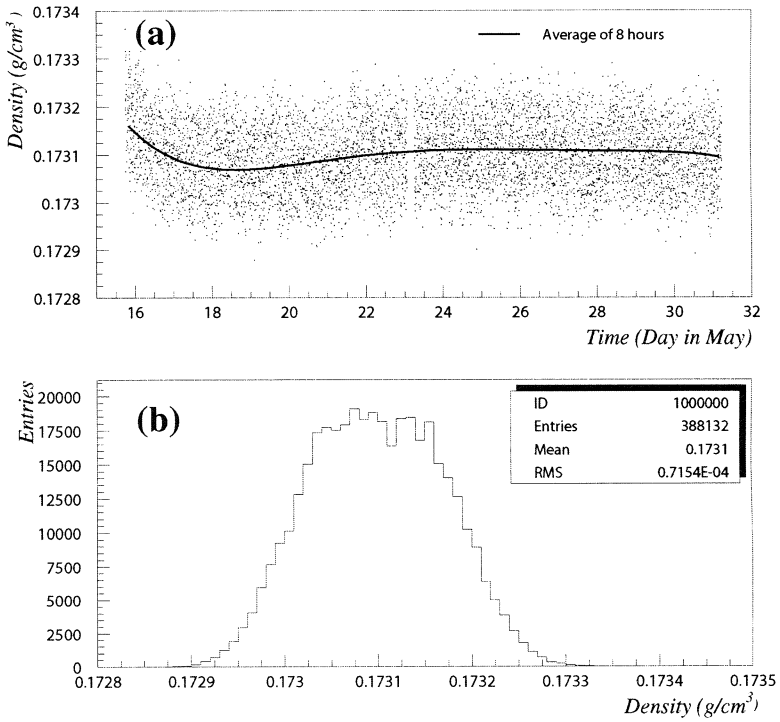

Fig.10. (a) is time course of the density of the deuterium liquid during the beam time in May 2004. (b) is the histrogram of the density.

was 0.1731±0.00007 g/cm^3 including the long term stability and short term fluctuation. The stability of the target density was 4×10^{-4}. The uncertainty of the target thickness was 0.55 %. The error of the number of the target was 0.3 % due to the fluctuation of the beam position. The total error of the target number was 0.63 %, which is less than the expected statistical error.

We also used the target system as a liquid hydrogen target. Even though the temperature was lower than the liquid deuterium, we could successfully and stably operate the liquid hydrogen target. The density of the liquid deuterium throughout the beam time in June 2004 was 0.07671±0.00003 g/cm^3.

We thank Mr. M. Takeshita of Suzukishokan Co. LTD. for designing, manufacturing, and upgrading the cryostat and the gas handling system. We also thank Mr. K. Fujioka of Cryoware Inc. for the fine fabrication of the CFRP vacuum chambers. We are grateful for Dr. H. Okuno of KEK and Mr. T. Morita of Sumitomo Heavy Industry Inc. for useful advices as an expert of former target systems for TAGX experiment. We express our gratitude to all the staffs in LNS Tohoku for their cooperation in developing, testing, and operating the target system.

References

[1] K. Maruyama *et al.* : Nucl. Instr. and Meth. A **376** (1996) 335.

[2] T. Kitami, Y. Akino, S. Kato, H. Okuno, Y. Doi, and A. Masaike : Preprint INS-TH-94, Institute for Nuclear Study, University of Tokyo (1975).

[3] M. Harada, S. Kasai, S. Kato, T. Kitami, T. Maki, K. Maruyama, T. Murata, K. Niki, C. Rangacharyulu, and A. Sasaki : Nucl. Instr. and Meth. A **276** (1988) 451.

[4] S. Kato, T. Kitami, K. Maruyama, Y. Murata, S. Endo, K. Niki, and T. Morita : Nucl. Instr. and Meth. A **290** (1990) 315.

[5] S. Kato, K. Kobayashi, K. Maruyama, H. Okuno, O. Konno, T. Suda, T. Maki, H. Asami, and T. Koizumi : Preprint INS-Rep-870, Institute for Nuclear Study, University of Tokyo (1991).

[6] *LakeShore Temperature Measurement and Control, Lake Shore Cryotronics, Inc.*, (2002).

[7] H.D. Ramsbottom, S. Ali, and D. P. Hampshire : Cyrogenics **36** (1996) 61.

[8] K. Yamauchi : Master's thesis, Physics department, Tohoku University (2004).

[9] *Safety Data Sheet*, Air Liquide Corporate (2002), MSDS Nr: 039_AL Deuterium, URL:http://www.airliquide.com/safety/msds/en/039_AL_EN.pdf.

[10] M. Wakamatsu : Master's thesis, Physics department, Tohoku University (2003).

[11] UPILEX-S *Ube Ultra-High Heat-Resistant Polyimide Film*, Ube Industries Ltd.(2002).

[12] STYCAST 1266 A/B Two Component, Low Viscosity, Epoxy Encapsulant, Emerson & Cuming, (1999) 1755-1266/11-99.

[13] J. Gerhold : Cryogenics **38** (1998)1063.

[14] T. Shigi, ed.: Handbook for Superconduction and Cryogenic Engineering (in Japanese), (Cryogenic Association of Japan, Tokyo, 1993).

[15] H. Yamaoka, K. Miyata, and O. Yano : Cryogenics 35 (1995) 787.

[16] *Mylar Product Information Chemical properties*, DuPont Teijin Films (1995), reorder No.: H-37250-1.

[17] T.Tsuru, S.Ishimoto, and S. Suzuki : URL http://www-ps.kek.jp/benkeh2t/.

[18] S. Ishimoto : URL http://ishimotopc2.kek.jp/LHeIIT/.

(LNS Experiment : #2466, #2482)

Study of Radiation Damage of CCD Sensors by Electron Beam Irradiation

K. Abe[1], T. Aso[2], K. Fujiwara[3], G. Iwai[3], A. Miyamoto[4], Y. Sugimoto[4], H. Takayama[3], N. Tamura[3], T. Terasawa[5], and H. Yamazaki[5]

[1]*Department of Physics, Tohoku Gakuin University, Sendai 980-8578*
[2]*Computer Engineering Department, Toyama National College of Maritime Technology, Toyama 933-0293*
[3]*Department of Physics, Niigata University, Niigata 950-2181*
[4]*High Energy Accelerator Research Organization (KEK), Ibaraki 305-0801*
[5]*Laboratory of Nuclear Science, Tohoku University, Mikamine, Sendai 982-0826*

CCD pixel sensors are expected to have very high performance as a charged particle tracking device because of the excellent spatial resolution and the very thin material thickness of the sensitive layer. One disadvantage of CCD sensors is its relatively low radiation hardness. We have exposed CCD samples to 140 MeV electron beam of LNS and studied their radiation tolerance. Comparing with the results of ^{90}Sr irradiation test, the energy dependence of the radiation damage has been clearly seen.

§ 1. Introduction

At the future e^+e^- linear collider experiment [1, 2, 3] the vertex detector has a great importance for physics analysis through b-quark, c-quark, τ, and gluon jet tagging. CCD pixel sensors are thought to be one of the primary candidates of the vertex detector. CCDs have advantages of the excellent spatial resolution through charge spread among adjacent pixels, and thin active layer thickness which reduces multiple scattering effects. One possible disadvantage of CCDs is their relatively low radiation tolerance. At the linear collider experiment, a large number of e^+ and e^- beam background, called pair background, is created through the beam-beam interaction at the collision point. The estimated background rate is larger than 1×10^{11}/cm^2/year at the innermost layer of the vertex detector located at R = 24 mm. So the study of radiation tolerance of CCDs is the most urgent issue for the application to the vertex detector at the linear collider experiment.

So far, we have studied the radiation damage effect of CCDs by ^{90}Sr β ray irradiation [4, 5]. However, the energy of the pair background hitting the vertex detector peaks at around 20 MeV, which is much higher than the energy of ^{90}Sr β ray. Bulk damage in Si is thought to be proportional to non-ionizing energy loss (NIEL). Figure 1 shows model calculations of NIEL [6, 7]. As can be seen from this figure, NIEL has a strong energy dependence below 100 MeV. Since extrapolation of the ^{90}Sr irradiation results to 20 MeV has a large ambiguity, we have directly measured the damage effect by high energy electrons [8].

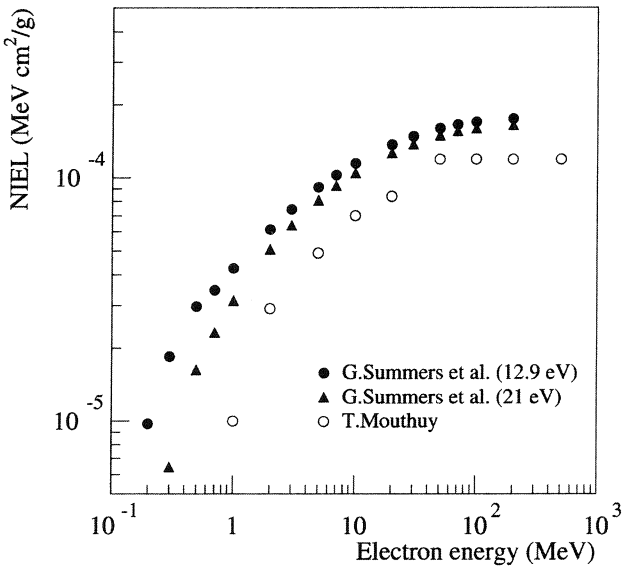

Fig.1. Model calculations of non-ionizing energy loss (NIEL) [6, 7]. The estimation by Summers *et al.* assumes two different threashold energies required for lattice dislocation.

§ 2. Irradiation Experiment

The electron beam irradiation was carried out at Laboratory of Nuclear Science, Tohoku University (LNS). A 140 MeV pulsed electron beam from the linac was fed into Stretcher Booster ring [9] and extracted as a quasi-DC beam. The beam was transported into BL-V beamline [10] and hit an aluminum frame of a foil-radiator which is usually used for tagged photon experiments. The beam was broadened by multiple scattering by the aluminum frame, bent by a dipole magnet, and irradiated CCDs uniformly.

The CCDs irradiated with the electron beam are special variants of S5466 made by Hamamatsu Photonics. They have 256 × 256 active pixels, and the pixel size is 24 μm.

We have irradiated the CCD step by step up to the dose of $5 \times 10^{11}/cm^2$. The characteristics of the CCD were measured after irradiation of $0.5 \times 10^{11}/cm^2$, $1.0 \times 10^{11}/cm^2$, $2.0 \times 10^{11}/cm^2$, and $5.0 \times 10^{11}/cm^2$, as well as before the irradiation. The irradiation was performed at the room temperature with all pins of the CCD grounded.

The irradiation dose was measured by a two-dimensional array of Si PIN photodiodes placed just downstream of the sample CCD. The photodiodes were placed at 10.16 mm pitch. The current induced by

electrons passing through the photodiodes was converted to voltage, and the voltage for each photodiode was measured by multi-channel digital multi meter (DMM). The measured voltages were readout by a computer through RS-232C interface every 5 seconds, and recorded as a file. The time constant of this measurement circuit is longer than the time structure of the beam bunches. Therefore, we measured the averaged beam intensity. From the distribution of the beam intensity in the two-dimensional array, we observed the uniformity of the irradiation over the CCD area. We also used RadFETs [11] as an integrated dose monitor for the cross-check. Both measurements were consistent with each other.

§ 3. Measurement of Characteristics of CCDs

After the irradiation of a certain dose, the sample was brought back to KEK and its characteristics were measured to see the radiation damage effects.

The CCD sample was put inside of a cryostat using liquid nitrogen, and the temperature was controlled between −100°C and +20°C during the measurements. The CCD was read out at a clock rate of 250 kpix/s and the analog output of the CCD was fed into a correlated double sampling circuit, an amplifier, and read out by a VME ADC.

We measured dark current and charge transfer inefficiency (CTI) of the sample CCD as a function of temperature. The CTI was derived from the position dependence of the peak of Mn-K_α line (5.9 keV) of ^{55}Fe. The X-ray exposure was controlled using a mechanical shutter and the CCD was read out after the shutter was closed. The cycle time of the exposure and readout was two seconds.

§ 4. Results and Discussions

4.1 Dark current

The sample CCDs can be operated in multi-pinned phase (MPP) mode (or inverted mode). If the low level of the clock pulse exceeds some value, the CCD gets into MPP mode from normal mode. In MPP mode, the surface dark current is strongly suppressed and the bulk current dominates. After the irradiation, an increase of the dark current was observed. In MPP mode, the dark current at 10°C increased from ~ 40 electrons/pixel/s to ~ 200 electrons/pixel/s after 1×10^{11}/cm^2 irradiation of the high

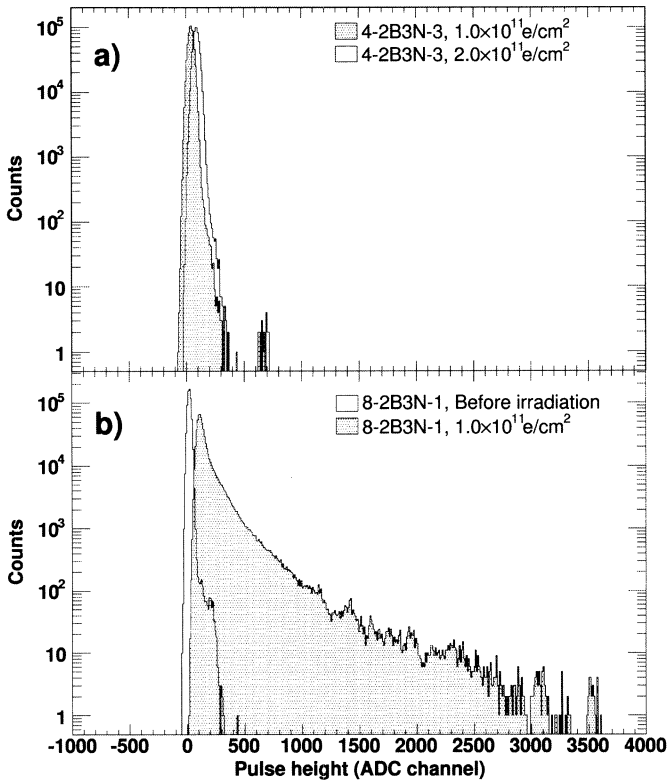

Fig.2. Distribution of dark current of CCDs (a) after irradiation of 1×10^{11}/cm^2 and 2×10^{11}/cm^2 β ray of ^{90}Sr and (b) before and after 1×10^{11}/cm^2 140 MeV electron beam irradiation [8].

energy electrons. In the readout cycle time of 6.7 ms at GLC [1], this dark current is not a problem at all.

We observed a large difference in the distribution of the dark current between the beam-irradiated CCD and the β-ray-irradiated CCD as shown in Fig.2. The beam-irradiated CCD shows a long tail of hot pixels which can not be seen in the β-ray-irradiated one. These hot pixels are presumably due to cluster-defects which cannot be created by low energy β ray [7, 12].

In MPP mode, we observed the spurious dark current, which is generated during clocking and thought to be due to impact ionization by holes trapped in Si-SiO_2 interface levels. The beam-irradiated CCD showed larger spurious dark current than β-ray-irradiated one at higher temperature. For the CCD irradiated with $1 \times 10^{11}/cm^2$ beam electrons, the spurious dark current of about 100 electrons/pixel was observed at 10 °C.

Surface damage of CCDs causes shift of operating voltage (gate clock voltage), called as flat-band voltage shift. The flat-band voltage shift of the sample CCDs is measured as the shift of the transition voltage from normal node to MPP mode. At the dose level of $2 \times 10^{11}/cm^2$, no significant flat-band voltage shift was observed for the sample CCDs.

4.2 Charge transfer inefficiency

The measured CTI in the vertical (parallel) register as a function of temperature is shown in Fig.3 both for the electron-beam irradiated sample and for the β-ray-irradiated sample. From this figure, it can be seen that the high energy electron beam has about 3 times larger effect than β ray of ^{90}Sr in creating the CTI.

The CTI is expected to be reduced by injecting extra charge which fills up trap centers. This technique is called 'fat-zero charge' injection. We have measured the effect of this fat-zero charge injection. The fat-zero charge was injected by illuminating the CCD continuously with LEDs. The CTI with the fat-zero charge injection is also plotted in Fig.3. Suppression of the CTI by the fat-zero charge

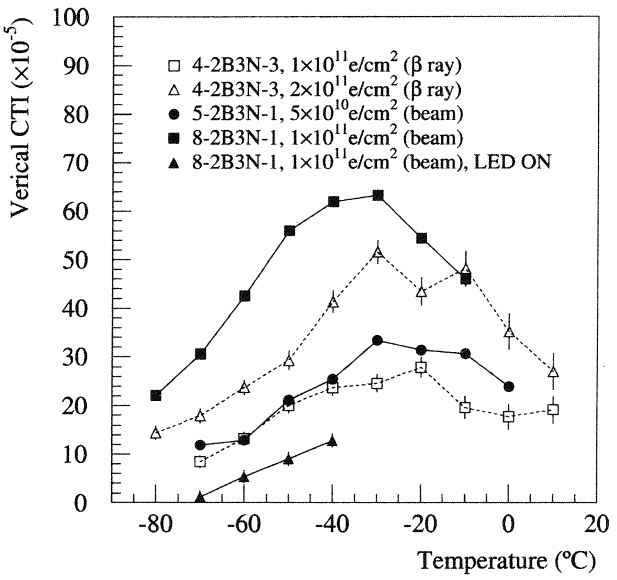

Fig.3. Charge transfer inefficiency (CTI) as a function of temperature. CTI with fat-zero charge injection of ~ 1200 electrons/pixel is also plotted [8].

injection was clearly observed.

In our measurement, the CTI in the horizontal (serial) register was smaller than the sensitivity of the measurement (less than 5×10^{-5} at -60 °C). This is presumably due to the CTI suppression by the large spurious dark current in the horizontal register.

§ 5. Conclusions

We have executed electron irradiation experiment of CCD pixel sensors at LNS in order to study the radiation damage effects expected at the future high energy e^+e^- linear collider experiment. The characteristics of electron-beam irradiated CCDs have been measured and compared with that of ^{90}Sr β-ray-irradiated CCDs. We have observed energy dependence of the radiation effects of CCDs clearly. We found that the 140 MeV electrons create hot pixels which cannot be found in β-ray-irradiated CCDs. No significant flat-band voltage shift was observed up to 2×10^{11} /cm^2 irradiation. The CTI caused by the high energy electron beam was found to be 2−3 times larger than that caused by the β-ray of ^{90}Sr. Suppression of the CTI by fat-zero charge injection has been demonstrated. The results we have obtained in this work give an important guideline to the design and further R&D of the CCD vertex detector at the linear collider experiment.

Acknowledgement

Authors would like to thank the staff of LNS for the excellent operation of the accelerator and the beamline. This work is partially supported by Japan-Europe (UK) Research Cooperative Program of JSPS.

References

[1] K. Abe *et al.*: GLC Project, KEK Report 2003-7.

[2] T. Abe *et al.*: Linear Collider Physics, SLAC-R-**570** (2001).

[3] TESLA Technical Design Report, DESY 2001-011.

[4] K.D. Stefanov *et al.*: IEEE Trans. Nucl. Sci. NS-**47** (2000) 1280.

[5] K.D. Stefanov *et al.*: Nucl. Instr. and Meth. A **453** (2000) 136.

[6] T. Mouthuy: Atlas Internal note Indet-No-**28** (1993).

[7] G.P. Summers *et al.*: IEEE Trans. Nucl. Sci. NS-**40** (1993) 1372.

[8] Y. Sugimoto *et al.*: submitted to Nucl. Instr. and Meth. A.

[9] F. Hinode *et al.*, "Proc. 12th Symp. on Accelerator Science and Technology", RIKEN, Wako, Japan (1999) 177.

[10] M. Chiba *et al.*: submitted to Nucl. Instr. and Meth.

[11] REM Oxford Ltd., Oxford, England.

[12] S. Wood *et al.*: IEEE Trans. Nucl. Sci. NS-**28** (1981) 4107.

Beam Test of a BSO Calorimeter

F. Miyahara[1], H. Hariu[2], T. Ishikawa[1], M. Itaya[2], T. Iwata[2], T. Kinoshita[1], M. Moriya[2], T. Nakabayashi[1], Y. Tajima[2], T. Hayakawa[1], M. Yamamoto[2], H. Yamazaki[1], H.Y. Yoshida[2], Y. Yoshida[2], and H. Shimizu[1]

[1]*Laboratory of Nuclear Science, Tohoku University, Sendai 982-0826*
[2]*Department of Physics, Yamagata University, Yamagata 990-8560*

The response of an electromagnetic calorimeter of large bismuth silicate (BSO) crystals has been measured for the first time for electrons, positrons, and charged pions at the incident momentum ranging from 0.5 to 3.0 GeV/c. The calorimeter consists of 9 BSO crystals arranged in a 3 × 3 matrix. The size of each crystal is 22mm × 22mm × 180mm (15.6 radiation lengths). The energy resolution of $(\sigma_E/E)^2 = (0.024 \pm 0.003/\sqrt{E\ [\mathrm{GeV}]})^2 + (0.018 \pm 0.002)^2$ has been obtained for incident electrons. The position information for the electrons injected onto the center crystal is given with energy deposit signals from 9 BSO crystals. The obtained position resolution is better than 5 mm in this energy range. The misidentification probability of pions to electrons is found to be $\sim 10^{-3}$ in the energy range from 1.0 to 3.0 GeV.

§ 1. Introduction

In the energy region of several hundred MeV, NaI(Tl) and CsI crystals are often used for electromagnetic (EM) calorimeters since the light outputs of these crystals are rather large so as to give a good energy resolution. However, the total volume of the NaI(Tl)/CsI calorimeter would be relatively large because their unit radiation lengths are long compared to that of other crystals. In addition to that, there is another inconvenience that the hygroscopicity of these crystals has to be taken care during experiments. Bismuth silicate $Bi_4Si_3O_{12}$ (BSO) scintillating crystals have good characteristics [1] such as a short unit radiation length and non-hygroscopicity. BSO may well replace these crystals regardless of smaller light output since the number of scintillating photons is large enough if the energy of the incident γ is in the several hundred MeV region or higher. Table 1 lists physical properties of BSO and other crystals. BSO crystals have not been used notwithstanding their good qualities for EM calorimeters because it was difficult to grow a large single crystal. Recently Ishii *et al.* succeeded in

Table 1. Properties of some scintillators. (f : fast component, s : slow component)

	Density (g/cm^3)	Radiation length (cm)	Decay constant (ns)	Peak emission (nm)	Relative output	Hygroscopicity
BSO	6.8	1.15	99	480	0.04	no
BGO	7.13	1.12	300	410	0.15	no
NaI(Tl)	3.67	2.59	250	410	1.00	very
Pure CsI	4.53	1.85	10^f, 620^s	305^f, ~480^s	0.10^f, 0.20^s	some

growing up large BSO crystals with the vertical Bridgman method [2, 3], although there seemed to be some difficulties preventing them from producing a large number of big size crystals. Employing the same method but with an additional technique we have gotten the way for mass production of large single BSO crystals in cooperation with a crystal company supervised by Ishii. We performed the first beam test of a prototype BSO calorimeter to measure the energy resolution and the position resolution for 0.5−3.0 GeV/c electrons and also the electron/pion separation factor.

§ 2. Experimental Setup

The measurement was made at the $\pi 2$ beamline of the proton synchrotron facility at KEK. Electron, positron and charged pion beams are produced by 12 GeV protons striking a production target located in the synchrotron ring. The produced charged particles are momentum-analyzed with the beamline magnets. The beam momenta used in the test experiment are 0.5, 1.0, 1.5, 2.0, and 3.0 GeV/c. The experimental setup is illustrated in Fig.1.

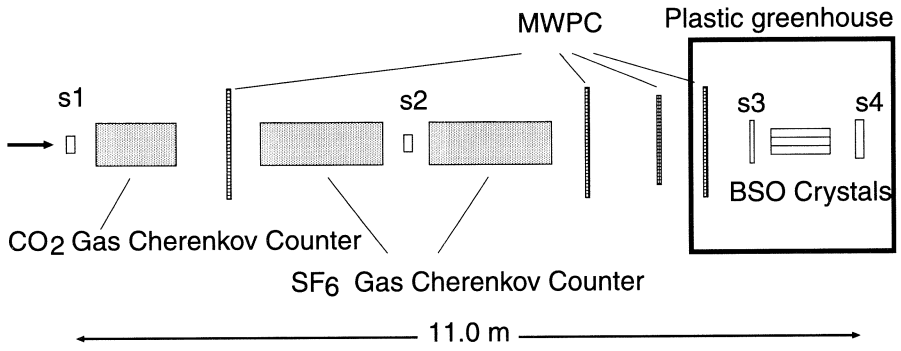

Fig.1. Plan view of experimental setup.

Three plastic scintillation counters, S1, S2 and S3, are used as trigger counters. Particle identification is made by means of time of flight (TOF). And the momentum resolution for the $\pi 2$ beam line is evaluated also with TOF spectra given by time difference between the signals from S1 and S4 plastic counters, the thickness of which is 10 mm and 30 mm, respectively. Three sets of gas Cherenkov counters(GCC) distinguish electrons/positrons from the other charged particles. The GCC1 is filled with 1.8 atm CO_2 gas, while 1 atm SF_6 gas is employed for GCC2 and GCC3. The three GCCs are used in the trigger for electrons. The trajectory of a charged particle is obtained by using four sets of multiwire proportional chambers (MWPC). Each MWPC has 2 wire planes, x and y. The wire spacing for all these planes is 2 mm. The BSO calorimeter, shown in Fig.2, consists of 9 BSO crystals giving a 3 × 3 matrix. Each crystal size is 22 mm × 22 mm × 180 mm, which corresponds to 15.6 radiation lengths along the incident beam direction. The calorimeter located at the end of the beam line is placed in a plastic greenhouse so that thermal stabilization is achieved. The temperature in the greenhouse has been monitored during the measurement and is kept to be 17 ± 1 °C.

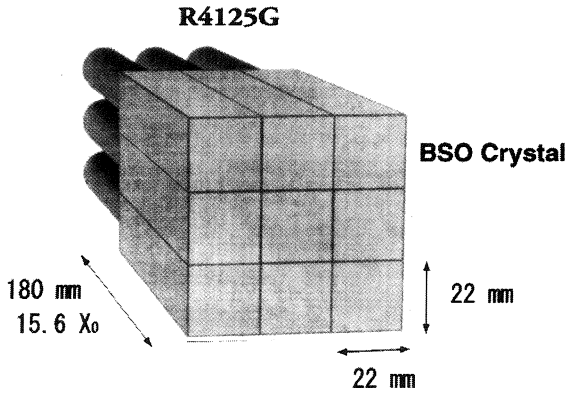

Fig.2. Schematic view of the BSO calorimeter.

§3. Results

3.1 Energy resolution

Figure 3 shows the energy spectra for the 0.5, 1.0, 1.5, 2.0, and 3.0 GeV/c electrons incident on the 4×4 mm^2 area of the central crystal after energy calibration is made. The deposited energy is given by

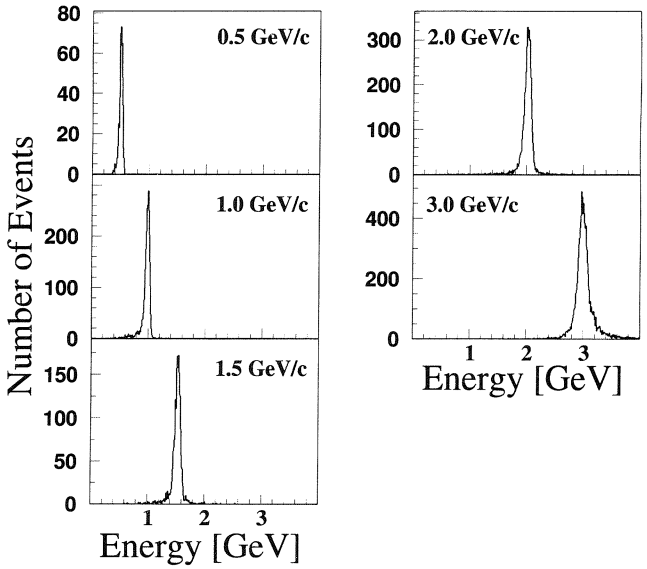

Fig.3. Response of the BSO calorimeter for 0.5, 1.0, 1.5, 2.0, and 3.0 GeV/c electrons.

summing up all the signals of the 9 crystals and normalized with 3 GeV/c electrons. These spectra are fitted with a Gaussian function.

Figure 4(a) shows the obtained energy resolutions σ_E/E (closed circles) and the result of Monte Carlo simulations based on the GEANT3 code (open diamonds) as a function of the incident electron energy. The energy resolution σ_E/E is deduced by subtracting the effect of the beam-momentum spread from the observed value σ_{ob}/E_{ob} which may be written as

$$\frac{\sigma_{ob}}{E_{ob}} = \sqrt{\left(\frac{\sigma_E}{E}\right)^2 + \left(\frac{\sigma_b}{E_b}\right)^2} \qquad (1)$$

Here E_b represents the beam energy and σ_b denotes the energy spread of the beam which is estimated

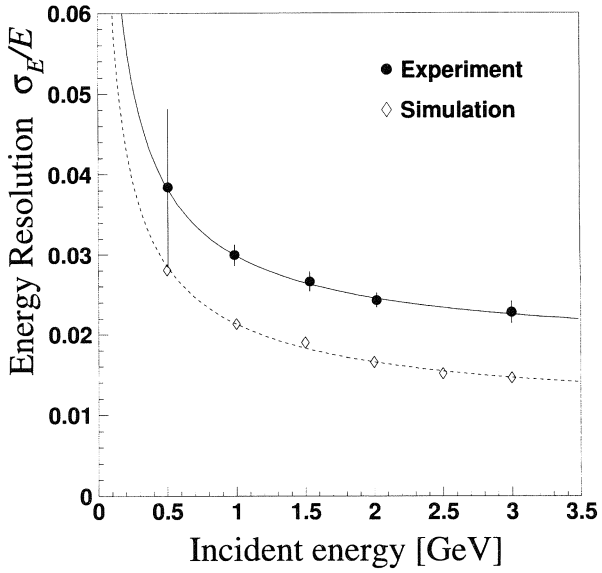

Fig.4. Energy resolution σ_E/E of a 3 × 3 BSO crystal calorimeter. The solid line indicates function(2) with parameters obtained by fitting the data. The dashed line represents a simulation result for the same detector arrangement.

from the momentum resolution of the $\pi 2$ beam line. The momentum spread for 1 GeV/c protons is measured with TOF and 0.7% is obtained for σ_b/E_b. The energy resolution is parameterized as

$$\frac{\sigma_E}{E} = \sqrt{\left(\frac{a}{\sqrt{E}}\right)^2 + b^2} \qquad (2)$$

where a means the statistical fluctuation for the incident energy E given in GeV and b is a constant. By fitting the data of σ_E/E with Eq. (2), the coefficients are found to be a = 0.024 ± 0.003, b = 0.018 ± 0.002 (experiment) and a = 0.019, b = 0.010 (simulation).

Figure 5 shows a simulation result for the correlation between a crystal length and the parameters a and b. The statistical term a is constant through this energy range and the constant term b depends on the crystal length. The result indicates that the fluctuation of EM showers is almost constant in this energy region and that shower leakage from the calorimeter mostly accounts for the constant term. However, the length of our crystal (180 mm) seems long enough according to the simulation result. Discrepancy in the constant term could be related other effects such as non-uniformities in the crystal response [4].

3.2 Position resolution

Position information for the incident γ/electron is important to provide an accurate reconstructed invariant mass of a meson decaying into photons or electrons (e.g. $\eta \to 2\gamma$, $\eta \to e^+e^-\gamma$, *etc.*). The position of the center of gravity X_{cg} is given with measured energy deposits as

$$X_{cg} = \frac{\sum_{i=1}^{9} E_i x_i}{\sum_{i=1}^{9} E_i} \qquad (3)$$

where E_i is the energy deposit and x_i the x coordinate of the center of the ith crystal. Comparing a X_{cg} to the MWPC reconstructed position, we obtain an energy dependent function giving the position of the incident γ/electron out of the X_{cg}. The position resolution of the BSO calorimeter is estimated with the

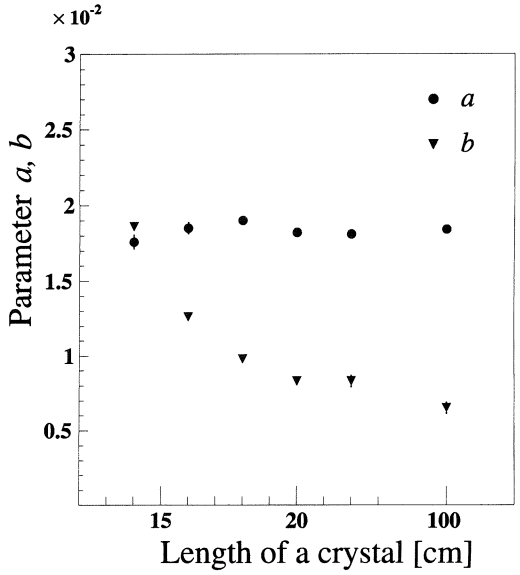

Fig.5. Correlation between a crystal length and the parameters a, b.

standard deviation of the position given by the function with the X_{cg} from the MWPC reconstructed position. The results are shown in Fig.6. The position resolution at the center of the calorimeter is better than 5 mm for incident electrons of the energy greater than 0.5 GeV.

3.3 Electron/pion separation

The e/π separation capability is one of the characteristics to be measured for EM calorimeters. Pions produced in experiments sometimes give a large energy deposit due to the nuclear reaction taking place in the calorimeter. In order to measure the e/π separation factor, first of all, pions have to be well selected on the $\pi 2$ beam line. Three GCCs are employed for this purpose. The detection efficiency of the

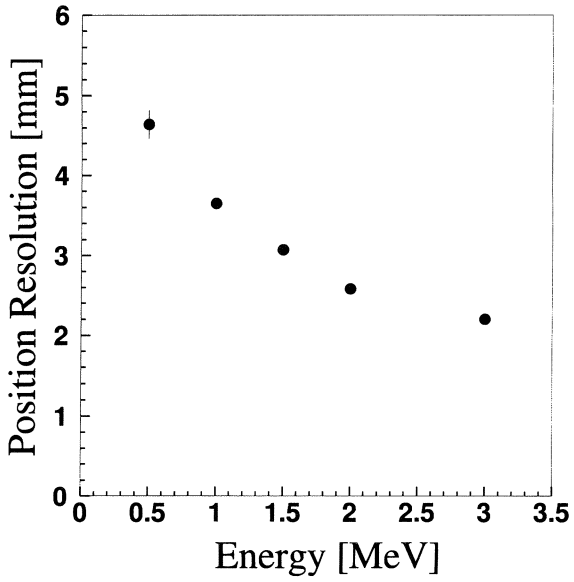

Fig.6 Position resolution at the center of the calorimeter.

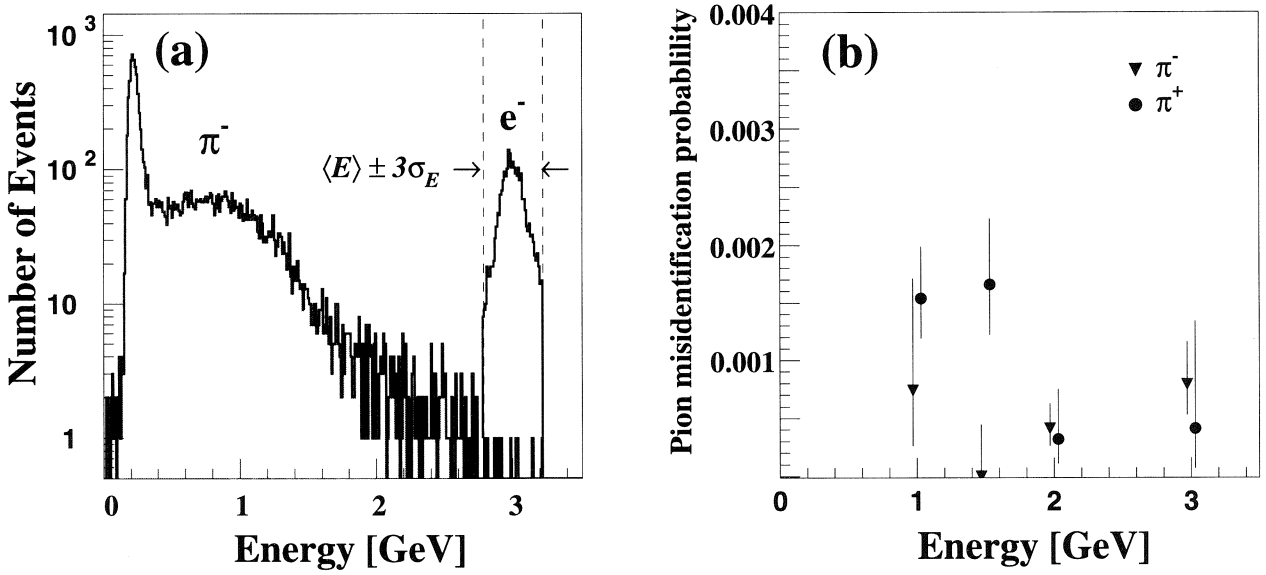

Fig.7. (a) Energy spectra for 3 GeV/c π^- together with 3 GeV/c electrons. (b) Misidentification probability of pions to electrons.

ith GCC for electrons is given by

$$\varepsilon_i = \frac{Y_{123}}{Y_{jk}} \tag{4}$$

where Y_{123} represents the number of three-fold coincidence events firing 3 GCCs simultaneously and Y_{jk} means that of two-fold coincidence events. The obtained efficiencies are $\varepsilon = 0.959$, $\varepsilon_2 = 0.996$, and $\varepsilon_3 = 0.987$, respectively. Thus the contamination ratio of electrons into the pion beam is found to be $(1-\varepsilon_1)(1-\varepsilon_2)(1-\varepsilon_3) = 2.13 \times 10^{-6}$. Figure 7(a) shows the response of the BSO calorimeter for 3.0 GeV/c π^- and electrons. The peak around 200 MeV corresponds to the minimum ionization loss of passing through pions and a broad bump up to 3.0 GeV is due to the nuclear reaction in the BSO crystals. The pion spectrum has an overlap with the electron peak slightly. Using the measured energy resolution we define the misidentification probability of pions to electrons (so called e/π separation factor) at each momentum as

$$\eta = \frac{\sum_{E=<E>-3\sigma_E}^{E=<E>+3\sigma_E} Y_\pi(E)}{\sum_{E=0}^{\infty} Y_\pi(E)} \tag{5}$$

where Y_π(E) is the number of pions for the incident momentum E, $\langle E \rangle$, the peak energy of electrons at each momentum, and σ_E, the measured energy resolution. Figure 7(b) shows the misidentification probability of pions to electrons in the energy range from 1.0 to 3.0 GeV. There is no clear difference observed between π^+ and π^- in the present experiment. The misidentification probability is found to be about 1/1000.

§ 4. Conclusions

We have tested a calorimeter consisting of 3 × 3 BSO crystals using electron, positron and charged pion beams of 0.5, 1.0, 1.5, 2.0 and 3.0 GeV/c. The obtained energy resolution is $(\sigma_E/E)^2 = (0.024 \pm 0.003/\sqrt{E\ [\mathrm{GeV}]})^2 + (0.018 \pm 0.002)^2$ in this energy range. The position resolution is found to be better than 5

mm at the center of the calorimeter for 0.5−3.0 GeV/*c* electrons. The electron/pion separation factor (the misidentification probability of pions to electrons) is estimated to be approximately 10^{-3} in the energy range of 1.0−3.0 GeV.

References

[1] M. Kobayashi *et al.*: Nucl. Instr. and Meth. A **400** (1997) 392.

[2] M. Ishii *et al.*: Journal of Crystal Growth **205** (1999) 191.

[3] M. Ishii *et al.*: Optical Materials **19** (2002) 201.

[4] G. Gratta *et al.*: Annu. Rev. Nucl. Part. Sci. **14** (1994) 453.

Experiments with a Forward Gamma Detector at SPring-8/LEPS

K. Kino[1], H. Fujimura[2], S. Hasegawa[1], K. Hicks[3], T. Hotta[1], T. Ishikawa[4], T. Iwata[5], T. Kawamura[5], H. Kohri[1], T. Matsuda[6], T. Matsumura[1], M. Miyabe[7], N. Muramatsu[8], T. Nakano[1], M. Niiyama[8], K. Okamura[4], Y. Saito[4], Y. Shiino[9], M. Sumihama[1], Y. Sugaya[10], K. Suzuki[4], Y. Tajima[5], Y. Toi[6], T. Tsuru[11], M. Uchida[1], H. Yonemura[4], T. Yorita[12], H.Y. Yoshida[5], and H. Shimizu[4]

[1]*Research Center for Nuclear Physics (RCNP), Ibaraki, Osaka 567-0047*
[2]*School of Physics, Seoul National University, Seoul 151-747, Korea*
[3]*Department of Physics, Ohio University, Athens, Ohio 45701, USA*
[4]*Laboratory of Nuclear Science, Tohoku University, Sendai, Miyagi 982-0826*
[5]*Department of Physics, Yamagata University, Kojirakawa, Yamagata 990-8560*
[6]*Department of Applied Physics, Miyazaki University, Miyazaki 889-2192*
[7]*Department of Physics, Kyoto University, Kyoto 606-8502*
[8]*Advanced Science Research Center, Japan Atomic Energy Research Institute (JAERI), Tokai, Ibaragi 319-1195*
[9]*Department of Physics, Chiba University, Chiba 263-8522*
[10]*Department of Physics, Osaka University, Toyonaka, Osaka 560-0043*
[11]*High Energy Accelerator Research Organization (KEK), Tsukuba, Ibaraki 305-0801*
[12]*Japan Synchrotron Radiation Research Institute (JASRI), Sayou, Hyogo 679-5143*

An experiment for photoproduction of $2\pi^0$ and other neutral mesons has been performed at the SPring-8/LEPS beam line. A forward gamma detector (FG) newly constructed has been used in combination with the backward gamma detector (BG). The energy calibration of the forward gamma detector has been made by an iteration method applied for 2γ forming π^0. The obtained π^0 mass resolution is 4.9% for now. The invariant mass distributions for 2 and 3 gamma event data are also shown for preliminary results.

We performed measurements of neutral mesons through multi-gamma detection at the SPring-8/LEPS beam line using two gamma detectors, a forward gamma detector (FG) and a backward gamma detector (BG). Of the physical motivation is a measurement of $2\pi^0$ generated by the Primakov effect. This reaction is related to the polarizability of π^0. The polarizability is defined as a proportionality constant of a particle's dipole moment in an electromagnetic field. Only one measurement [1] has ever been reported for π^0, although this is one of the fundamental values for particle's properties. The invariant mass distribution from the $2\pi^0$ threshold to 2 GeV was obtained in that measurement and the polarizability was extracted using the S-matrix approach. The value given in an analysis recently made is $\alpha - \beta = -1.1 \pm 1.7$ fm^3 [2] and it has a large uncertainty. There are interests in studying the loop structures in the chiral perturbation theory[3]. The Primakov production of $2\pi^0$ could also give a

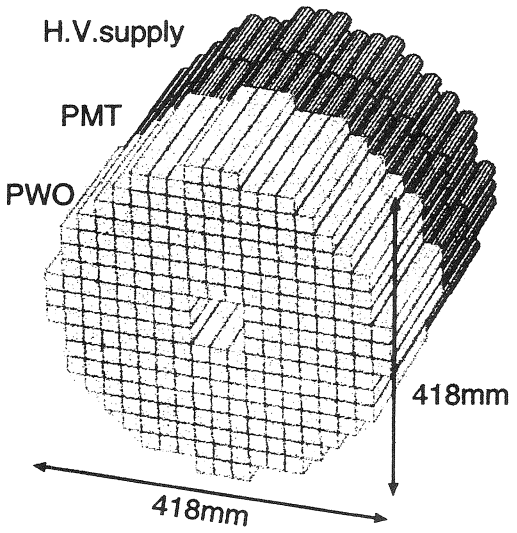

Fig.1. Forward gamma detector (FG).

unique approach for the σ meson study as the process of $\gamma + \gamma^* \rightarrow \sigma \rightarrow 2\pi^0$, where γ^* denotes a virtural photon corresponding to the electric field of a target nucleus.

One would expect the detection of η, η', ω, and K^0 in multi-gamma measurements. Measurements of these mesons are expected to be helpful in searching for "missing resonances" since ever observed states through πN scattering and π decay channels have not satisfied the predictions given by constituent quark models. The measurement of the beam asymmetry is expected for further information. In this report, we describe the structure of the forward gamma detector which has been constructed for these measurements and the basic analysis for the data taken with FG. Then some preliminary spectra obtained by combining FG and BG [4] will be shown.

The FG consists of 252 sets of a $PbWO_4$ crystal, a photomultiplier tube, and a high-voltage supplier. The size of each crystal is 22 × 22 × 180 mm^3. The length for the direction that the electromagnetic shower proceeds corresponds to 19.5 radiation lengths. Figure 1 shows the inside of the detector box. There is a hole which corresponds to nine crystals at the center of the detector in order that the incident gamma beam can go through the detector after passing the target. We used $PbWO_4$ crystals because of their superior properties. One radiation length of the crystal is 0.92 cm and this is smaller than that of other common crystals. The Moliere radius is small (22 mm) and this is suitable for a precise position measurement. The fast decay time (~10 nsec) is good for high count rate experiments like a forward angle measurement. One disadvantage is its relatively small light output, but it was not a problem for our experiment in which gamma-rays with higher energy dominate due to the measurement at a forward angle. A 3/4-in. HAMAMATSU R4125G photomultiplier tube was attached to the end of each crystal with a spring. We adopted a Cockcroft-Walton type (HAMAMATSU E974-19CWDP) high voltage supplier which can provide up to −1800 V. This equipment requires only two low voltage DC inputs and can make the high voltage system simple.

The experiment was performed with the setup shown in Fig.2. The gamma beam with an energy of 1.5-2.4 GeV and an intensity of 5-6 $\times 10^5$ photons/s was bombarded on targets. We used a tungsten

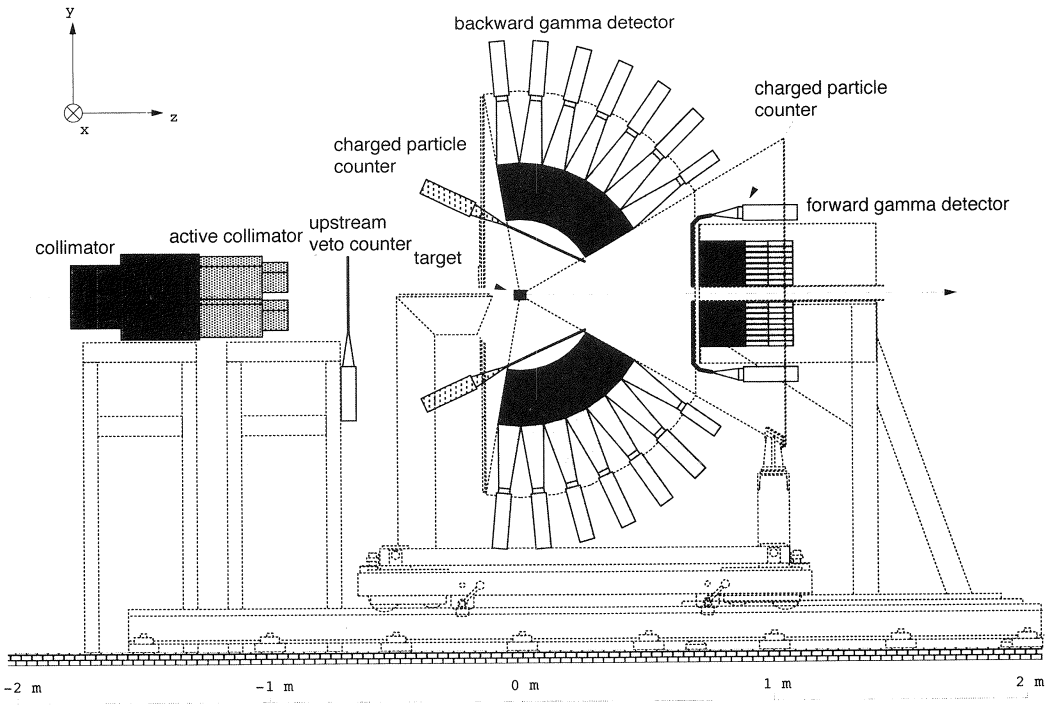

Fig.2. Detector setup. The distances from the target to the forward and backward detectors are 710 and 300 mm, respectively.

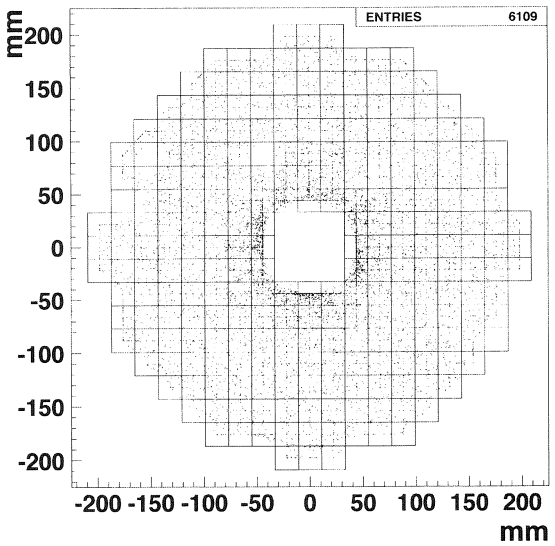

Fig.3. Position distribution of detected particles by the forward gamma detector. The squares in the figure represent the positions of 252 $PbWO_4$ crystals.

target for the Primakov reaction and polyethylene and carbon targets for nucleon resonances. The thickness of all these targets corresponds to ~0.1 radiation lengths. The FG and BG cover the polar angle of 5-15 deg and 30-100 deg with the full azimuthal angles, respectively.

The trigger for the data taking was generated by the following logic,

$$(FG \oplus BG) \otimes Tagger \otimes \overline{(UpstreamVeto \oplus ActiveCollimator)}, \quad (1)$$

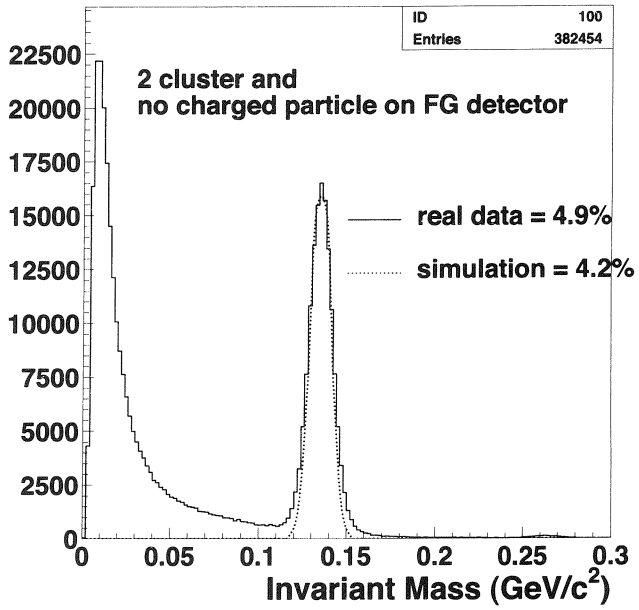

Fig.4. Invariant mass distribution of 2 gamma events detected with the forward gamma detector. The dotted line is the result of a GEANT4 simulation.

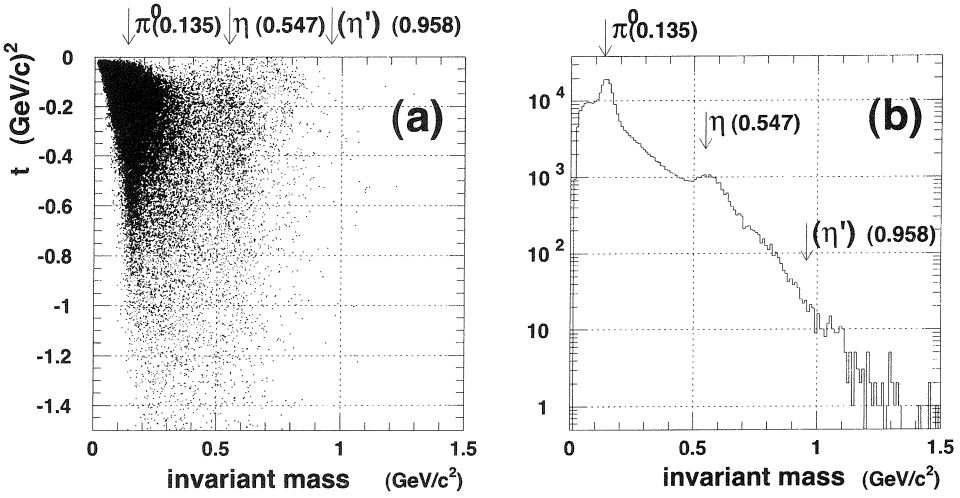

Fig.5. Invariant mass distribution of 2 gamma events, one gamma detected with FG and the other with BG. These are polyethylene target data.

where "*FG*" and "*BG*" represent the triggers of FG and BG, respectively. The trigger of FG was created when an energy of 30 MeV or higher was deposited at least in one $PbWO_4$ crystal except for twelve crystals which are closest to the beam line. Similarly, the trigger of BG was created when a 10 MeV or higher energy is detected in Lead/SCIFI modules. "*Tagger*" means the trigger signal by the tagging counter. "*UpstreamVeto*" is the signal of the plastic scintillation counter to veto electrons and positrons contained in the incident gamma beam. "*ActiveCollimator*" is the signal from four lead glass counters to veto background electromagnetic showers coming along the incident gamma beam. The charged particle counters were set in front of FG and BG but they were not included in the trigger. The trigger rate was 600-700 s^{-1} and the live time of the data acquisition was 70-80%. The temperature of FG was monitored

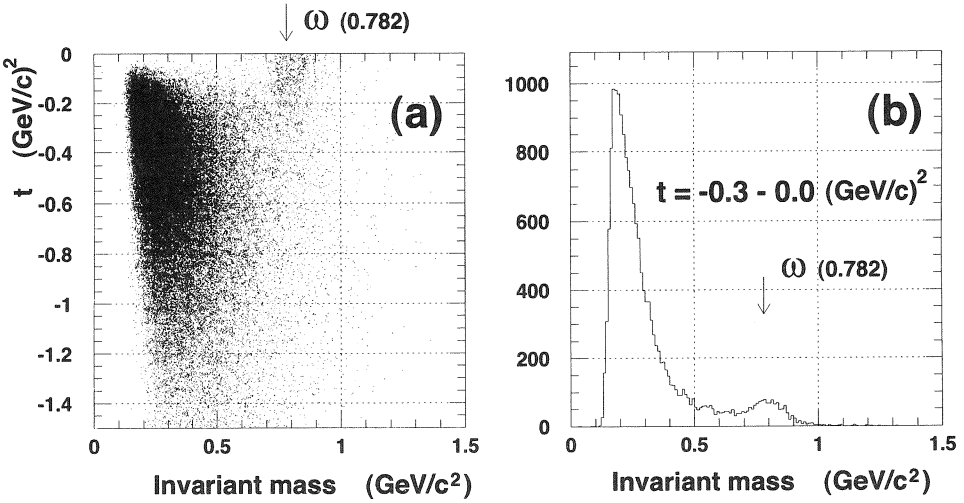

Fig.6. Invariant mass distribution of 3 gamma events. The momentum transfer $t = -0.3\text{-}0.0$ (GeV/c)^2 is selected in (b). These are polyethylene target data.

during the experiment since $PbWO_4$ crystals have the temperature dependence on their light outputs.

The energy calibration for each crystal of FG was done by using an iteration method using 2 gammas from π^0. The energy deposition of each electromagnetic shower in FG was basically obtained by nine crystals of the 3 × 3 matrix. The position reconstruction was performed by the center of gravity method. An example of the position distribution for detected gammas is shown in Fig.3. Many events concentrate around the beam line and most of them are either one of e^+e^- pairs and γ coming from the target. Figure 4 shows the invariant mass distribution of 2 gamma events in which both of gammas were detected by FG. A peak corresponding to π^0 is seen at 0.135 GeV/c^2. The obtained mass resolution (σ_m/m) for π^0 is currently 4.9%, while a GEANT4 simulation gives the mass resolution of 4.2% (dotted line).

Figure 5 shows data for which each of FG and BG detected one gamma-ray. The two peaks corresponding to $\pi^0 \rightarrow 2\gamma$ and $\eta \rightarrow 2\gamma$ decays are seen. The width is expected to be reduced by applying a kinematic fitting on events in which the recoil proton is detected. The η' meson is not observed at 0.958 GeV/c^2 for the time being. We are also searching η' through the $\eta' \rightarrow \pi^0\pi^0\eta$ decay channel. Figure 6 shows ω events decaying into the $\pi^0+\gamma$ channel. We applied a kinematic fitting under the condition that two of three gammas are from a π^0. The ω meson is strongly created at a small momentum transfer region as explained by the vector meson dominance model. The vertical axis in Fig.6(a) is the momentum transfer. One can see that ω events are concentrating on the small $|t|$ region. Analyses of above and other channels are in progress.

References

[1] H. Marsiske *et al.* : Phys. Rev. D **41** (1990) 3324.

[2] A.E. Kaloshin and V.V. Serebryankov: hep-ph 9306224.

[3] S. Bellucci *et al.* : Nucl. Phys. **B423** (1994) 86.

[4] T. Matsumura *et al.* : "*Nuclear Physics in Different Degrees of Freedom*", edited by H. Bhang, S.W. Hong, and H. Shimizu: Proc. 41, (Institute of Basic Science, 2002).

Search for *s*-channel Baryon Resonances in the $\gamma p \rightarrow a_0(980)p$ Reaction

T. Matsumura[1,2], J.K. Ahn[3], S. Daté[4], M. Fujiwara[1,2], K. Hicks[5], T. Hotta[1], T. Ishikawa[6], J. Kasagi[7], H. Kawai[8], T. Kinoshita[7], H. Kohri[1], T. Mibe[1,2], K. Miwa[6], M. Miyabe[6], N. Muramatsu[2], T. Nakabayashi[7], H. Nakamura[9], T. Nakano[1], M. Niiyama[6], Y. Ohashi[4], T. Ooba[8], D. Oshuev[10], C. Rangacharyulu[11], P.M. Shagin[12], Y. Shiino[8], Y. Sugaya[9], M. Sumihama[13,2], Y. Tajima[14], H. Yamazaki[7], T. Yorita[4], H.Y. Yoshida[14], R.G.T. Zegers[1], and H. Shimizu[7]

[1]*Research Center for Nuclear Physics, Osaka University, Osaka 567-0047*
[2]*Advanced Science Research Center, Japan Atomic Energy Research Institute, Ibaragi 319-1195*
[3]*Department of Physics, Pusan National University, Pusan 609-735, Korea*
[4]*Japan Synchrotron Radiation Research Institute, Hyogo 679-5143*
[5]*Department of Physics, Ohio University, Ohio 45701, USA*
[6]*Department of Physics, Kyoto University, Kyoto 606-8502*
[7]*Laboratory of Nuclear Science, Tohoku University, Taihaku, Sendai 982-0826*
[8]*Graduate School of Science and Technology, Chiba University, Chiba*
[9]*Laboratory of Nuclear Studies, Osaka University, Toyonaka, Osaka 560-0043*
[10]*Institute of Physics, Academia Sinica, Nankang, Taipei 11529, Taiwan*
[11]*Department of Physics and Engineering Physics, University of Saskatchewan, Saskatoon SK S7N 5E2, Canada*
[12]*Department of Physics and Astronomy, University of Minnesota, Minneapolis, MN 55455 USA*
[13]*Department of Physics, Osaka University, Toyonaka, Osaka 560-0043*
[14]*Department of Physics, Yamagata University, Kojirakawa, Yamagata 990-8560*

§ 1. Introduction

Studying the baryon excitation is one of the key issue for understanding the hadron structure. Recent discovery of the pentaquark state (Θ^+) from LEPS collaboration [1] led to a new insight into this field. Under such circumstances, understanding the non-strange cryptoexotic states, which are categorized as the member of exotic pentaquark states but have non-exotic quantum number, became important [2, 3]. The N*(1710) and/or N*(1440), where the spin-parity of both states are $J^P = 1/2^+$, are assigned to the candidates of these states by some theorists [4, 2]. However, it surely needs further investigation.

The $\gamma p \rightarrow a_0(980)p$ reaction might be a good tool when one tries to search for a new cryptoexotic baryon in the *s*-channel. The reason is that a $J^P = 1/2^+$ baryon can decay into an $a_0(980)$ and a proton with *s*-wave since the $a_0(980)$ is a scalar state ($J^P = 0^+$); therefore, the decay probability would be expected to be high because there is no angular-momentum barrier comparing to the case of the decay to a pseudo-scalar meson and a proton. Furthermore, the $a_0(980)$ resonance has relatively narrow width ($\Gamma \sim$ 50-100 MeV/c^2) among the all low-mass scalar mesons, and it is a well-established resonance.

Experimental search for baryon resonances in the decay mode (scalar meson + nucleon) has never been performed. In this report, we discuss the experimental search for new baryon resonances in the $\gamma p \rightarrow a_0(980)p$ reaction.

§ 2. Experiment

The experiment was held in November, 2001 at the LEPS/SPring-8 facility, where beam photons in the tagged energy region between 1.6 GeV and 2.4 GeV were produced by backward Compton scattering of laser photons off electrons in the SPring-8 storage ring [5].

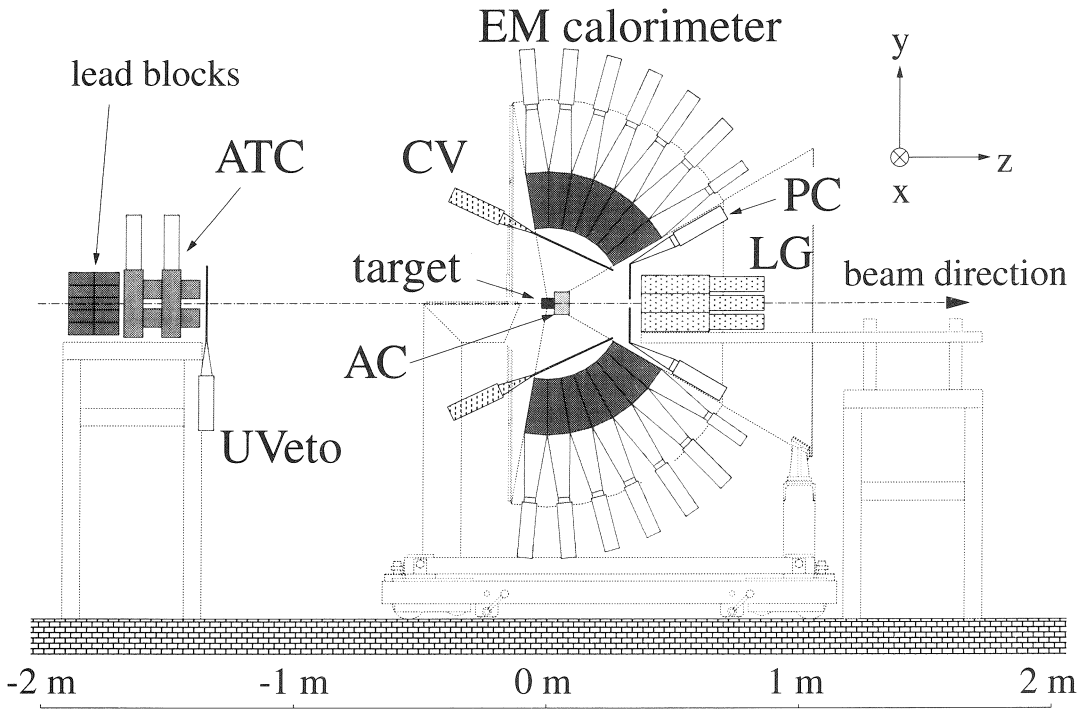

Fig.1. Side view of the experimental setup. A tagged photon beam generated at 70 m upstream from the target was injected on to a target. (CV and PC) plastic scintillators for charged-particle identification. (LG) lead glass counters for photon veto. (AC) aerogel counters with n = 1.05 for $\pi^{\pm}$/p identification. (ATC) active collimator consisting of 8 blocks of lead glass for beam-halo rejection. (UVeto) a plastic scintillator to reject any charged particles in the incoming beam.

Figure 1 shows the experimental setup. The main experimental device was a 2π-calorimeter consisting of 252 modules of lead scintillating fiber blocks [6]. The calorimeter was used in order to detect 4-photons coming from π^0 and η decays. Note that the decay mode of the $a_0(980)$ is dominantly $\pi^0\eta$. The energy resolution σ_E of the calorimeter was estimated to be $(\sigma_E/E)^2 = 0.052/\sqrt{E})^2 + 0.042^2$, where E is the photon energy in GeV; The angular resolutions are almost same for both polar and azimuthal angles and were $\sigma = 2.1°$ (1.2°) for a 100 MeV (1 GeV) photon. We employed carbon (40 mm thickness) and CH_2 (50 mm thickness) targets. The proton-target data were obtained by subtracting the carbon contribution from CH_2 spectra.

The event trigger was generated when any one of the calorimeter modules gave a signal in coincidence with a signal from the tagging scintillators. A 5-mm thick plastic scintillator (UVeto) and an

active collimator (ATC) consisting of 8 lead-glass blocks were placed upstream of the target to reject triggers due to charged particles and low-energy photons contaminating the incoming beam. An aerogel Cherenkov counter (AC) with a refractive index of 1.05 and forward plastic scintillators (PC) were installed for $\pi^{\pm}$ and recoil-proton identification. A detector assembly of 8 lead-glass blocks forming a 3 × 3 matrix (LG) was placed downstream of the calorimeter. The AC, PC and LG counters were used only for checking properties of background processes. Totally 6.2×10^7 and 4.2×10^7 triggered events were accumulated for the carbon and CH_2 targets, respectively.

§ 3. Result

From a systematic analysis, totally 469 events for the carbon target and 380 events for the CH_2 target were obtained as $\gamma p \rightarrow \pi^0 \eta p$ event samples. After a beam-flux normalization, we estimated the number of events originated from the proton target to be 113 ± 36 events.

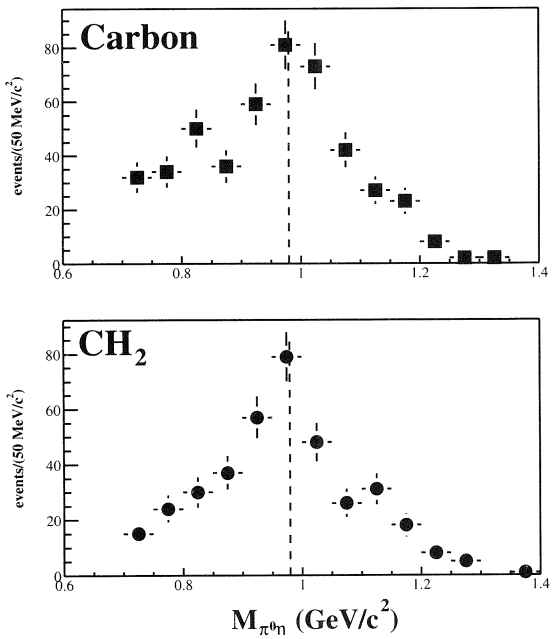

Fig.2. Invariant $\pi^0\eta$ mass ($M_{\pi^0\eta}$) spectra for the carbon and CH_2 samples. The dashed lines indicate the position of $M_{\pi^0\eta}$ = 980 MeV/c^2.

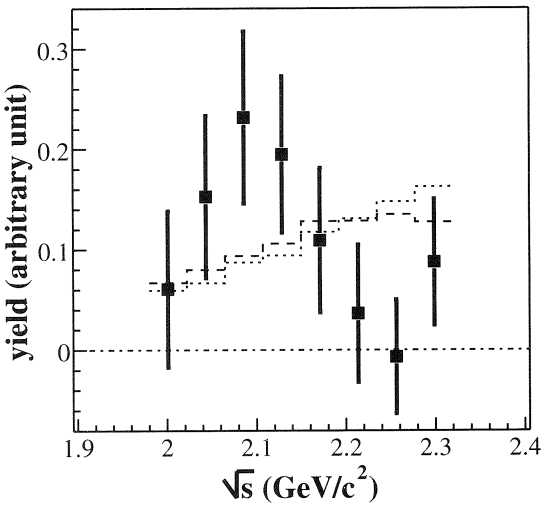

Fig.3. $\sqrt{s}$ distribution for the proton target. The histograms show the distributions obtained by an MC simulation.
(dashed line) $\gamma p \rightarrow \pi^0 \eta p$ phase space.
(dotted line) $\gamma p \rightarrow a_0(980)p$ phase space.

Figure 2 shows the invariant $\pi^0\eta$-mass ($M_{\pi^0\eta}$) spectra for each target. A peak around $M_{\pi^0\eta}$ = 980 MeV/c^2 was observed in both the carbon and CH_2 data. The peak corresponds to the scalar-isovector $a_0(980)$ resonance which couples strongly to the $\pi^0\eta$ system [7].

The distribution of the $\sqrt{s}$ (energy of the γp CM-system) for the proton-target data is shown in Fig.3. The distribution shows a resonance-like structure at around 2.1 GeV/c^2. The mass and the width of the resonance were estimated by assuming a Breit-Wigner resonance; They were $M = 2080^{+20}_{-20}$ MeV/c^2 and $\Gamma = 100^{+60}_{-20}$ MeV/c^2, respectively. This result might be interpreted that this state is a new baryon resonance that couples strongly to an $a_0(980)$ and a proton.

§ 4. Discussion

The statistics are not good enough to confirm whether the baryon resonance really exists or not. Nevertheless, it is worth discussing the spin-parity of the state. The $a_0(980)$ momentum in the CM system is about $k \sim 0.40$ GeV/c; thus, the characteristic parameter kR is 2.0 by assuming $R \sim 1.0$ fm. This means that the dominant contribution to the decay would be s-wave or p-wave. Therefore, the spin-parity of the state would be $J^P = 1/2^+$ for s-wave, and $J^P = 1/2^-$ or $3/2^-$ for p-wave. The iso-spin of the resonance is either $I = 1/2$ or $I = 3/2$ since the $a_0(980)$ is an iso-vector state. In order to improve the data statistics, we are now performing a data analysis with new data which have been taken in the autumn of 2003.

Acknowledgement

The authors would like to thank Dr. A. Hosaka (RCNP), Dr. M. Koma (MPIM), and Dr. A. Titov (JINR) for helpful discussion. This work was supported in part by the Grant-in-Aid for Scientific Research No.15340069 from the Ministry of Education and Science of Japan.

References

[1] T. Nakano *et al.*: Phys. Rev. Lett. **91** (2003) 012002.

[2] R. Jaffe and F. Wilczek: Phys. Rev. Lett. **91** (2003) 232003.

[3] R.A. Arndt *et al.*: Phys. Rev. D **69** (2004) 035208.

[4] D. Diakonov, V. Petrov, and M.V. Polyakov: Z. Phys. A **359** (1997) 305.

[5] T. Nakano *et al.*: Nucl. Phys. **A684** (2001) 71c.

[6] T. Matsumura *et al.*: Nucl. Phys. **A721** (2003) 723c.

[7] K. Hagiwara *et al.*: Phys. Rev. D **66** (2002) 010001.

ϕ Photo-production from Nuclei at E_γ= 1.5 - 2.4 GeV

T. Ishikawa[1], D.S. Ahn[2], J.K. Ahn[3], H. Akimune[4], W.C. Chang[5], S. Daté[6], H. Fujimura[7], M. Fujiwara[2,8], K. Hicks[9], T. Hotta[2], K. Imai[7], H. Kawai[10], K. Kino[2], H. Kohri[2], T. Matsumura[11], T. Mibe[2], K. Miwa[7], M. Miyabe[7], M. Morita[2], T. Murakami[7], N. Muramatsu[2], H. Nakamura[12], M. Nakamura[13], T. Nakano[2], M. Niiyama[7], M. Nomachi[12], Y. Ohashi[6], T. Ooba[10], D.S. Oshuev[5], C. Rangacharyulu[14], A. Sakaguchi[12], Y. Shiino[10], Y. Sakemi[2], H. Shimizu[1], Y. Sugaya[12], M. Sumihama[15], Y. Toi[16], H. Toyokawa[6], C.W. Wang[5], T. Yorita[6], M. Yosoi[7], and R.G.T. Zegers[17]

[1]*Laboratory of Nuclear Science, Tohoku University, Sendai 982-0826*
[2]*Research Center for Nuclear Physics, Osaka University, Ibaraki 567-0047*
[3]*Department of Physics, Pusan National University, Busan 609-735, Korea*
[4]*Department of Physics, Konan University, Kobe 658-8501*
[5]*Institute of Physics, Academia Sinica, Taipei 11529, Taiwan*
[6]*Japan Synchrotron Radiation Research Institute, Mikazuki 679-5198*
[7]*Department of Physics, Kyoto University, Kyoto 606-8502*
[8]*Advanced Science Research Center, Japan Atomic Energy Research Institute, Tokai 319-1195*
[9]*Department of Physics and Astronomy, Ohio University, Athens, Ohio 45701, USA*
[10]*Graduate School of Science and Technology, Chiba University, Chiba 263-8522*
[11]*National Defense Academy in Japan, Yokosuka 239-8686*
[12]*Department of Physics, Osaka University, Toyonaka 560-0043*
[13]*Department of Physics, Liberal Arts and Sciences, Wakayama Medical University, Wakayama 641-8509*
[14]*Department of Physics and Engineering Physics, University of Saskatchewan, Saskatoon, Saskatchewan S7N5E2, Canada*
[15]*Department of Physics, Tohoku University, Sendai 980-8578*
[16]*Physical Engineering Group, Miyazaki University, Miyazaki 889-2192*
[17]*National Superconducting Cyclotron Laboratory, Michigan State University, Michigan 48824, USA*

The modification of vector mesons in nuclear matter is a subject of great interest in hadron physics. Although a broadening of the width and/or a decrease of the mass were predicted for the ϕ meson in nuclear medium [1,2,3,4], no clear evidence has been obtained. The ϕ - N coupling should be suppressed because of the OZI rule since nucleon basically contains no $s\bar{s}$ pairs and ϕ meson is essentially 100% $s\bar{s}$. If the total ϕ -N cross section in nuclear medium, $\sigma_{\phi N}$, is the same as that in free space, the incoherent ϕ production cross section from nuclei, σ_A^{inc}, is almost proportional to the target mass number A. When $\sigma_{\phi N}$ is enlarged in nuclear medium due to the change of the ϕ properties, some fraction of photo-produced ϕ mesons would interact with a nucleon inside the nucleus and disappear, and the σ_A^{inc} is expected to have $\alpha < 1$ in the parameterization $\sigma_A^{inc} \propto A^\alpha$.

Only one measurement of ϕ photo-production from nuclei is reported at E_γ= 6.4−9.0 GeV [7]. The

value of $\sigma_{\phi N}$ was not accurately determined. On the other hand, $\sigma_{\phi N}$ in free space is well determined to be 7.7−8.7 mb from ϕ photo-production cross section on the proton, $d\sigma/dt|_{t=0}$, at E_γ= 4.6−6.7 GeV, where the γ - ϕ coupling is assumed to be energy independent constant in the vector meson dominance model (VDM) [8]. The value of $\sigma_{\phi N}$ in free space is much smaller than other meson-nuclear total cross sections, $\sigma_{\omega N}$, $\sigma_{\rho N}$, and $\sigma_{\eta N}$ (~30mb)[15].

Coherent production is suppressed near the threshold of ϕ photo-production due to the heavy mass of the ϕ meson. In the Glauber-type multiple scattering theory for incoherent production [9], the production cross section from nuclei, $d\sigma_A/dt$, is described as a product of the effective nucleon number, $A_{\rm eff}$, and the ϕ photo-production cross section on the nucleon, $d\sigma_0/dt$, where $A_{\rm eff}$ is a function of nucleon density distribution and $\sigma_{\phi N}$. Thus, $\sigma_{\phi N}$ obtained via the ϕ meson photo-production from nuclei at the incident energy near the threshold is expected to be determined less ambiguously as compared with that via the coherent photo-production at high energies.

The experiment was carried out using the Laser-Electron Photon facility at SPring-8 [10]. Photons were produced by backward Compton scattering from 8 GeV electrons in the storage ring. An ultra-violet Ar laser with wave lengths of 351 and 364 nm was used to generate a photon beam with the maximum photon beam energy of 2.4 GeV. The recoil electrons were momentum analyzed by a bending magnet in the storage ring, and were detected by a tagging counter placed at the exit of the bending magnet. Photons with energies above 1.5 GeV were tagged.

The nuclear targets used in the experiment were Li, C, Al, and Cu with thicknesses of 100 mm, 36 mm, 24 mm, and 3 mm, respectively. All the targets used were natural. The Li target block was placed in a target box filled with Ar gas. The windows of the target box were sealed with 50 μm aramid sheets. To minimize the difference of the acceptances among different target thicknesses and to avoid a systematic error caused in the acceptance correction, each of the other three targets was set by dividing into three pieces with the same center of gravity and standard deviation of the position along the photon beam direction as those of the Li target. To avoid the systematic errors due to the change of the beam conditions, targets were exchanged every two hours.

Charged particles produced by photo-reactions were momentum analyzed with the LEPS spectrometer system consisting of a dipole magnet, a silicon strip detector (SSD) array, and three multi-wire drift chambers. The SSD array and the first drift chamber were located upstream of the magnet and the other drift chambers were positioned downstream of the magnet. The angular coverage of the spectrometer was about ±0.4 rad and ±0.2 rad in the horizontal and the vertical directions, respectively. The momentum resolution for 1 GeV/c particles was 6 MeV/c (σ). The time of flight information was obtained for each charged particle. The start signal was produced by a 5 mm thick plastic scintillator (SC) located downstream of the target, and the stop signal was produced by an array of 40 plastic scintillators positioned 3.2 m downstream from the magnet center. The time of flight resolution was typically 150 ps (σ). Many electron and positron pairs were produced in the target material. Electrons, positrons, and high momentum pions were vetoed in the trigger by a silica aerogel Čerenkov counter located behind the SC.

The particle mass for each track was reconstructed by using the time of flight and the momentum

information. Kaons were identified within 4 σ of the momentum dependent mass resolution, which was about 30 MeV/c^2 for 1 GeV/c kaons. The contamination of pions due to the particle mis-identification is 3% for 1 GeV/c kaons. The ϕ mesons produced in the targets were selected by the vertex position (*vtz*) of the K^+K^- tracks along the photon beam direction. Figure 1(a) shows the *vtz* distribution of the K^+K^- tracks together with the selected region for the Cu target. The *vtz* position resolution at the SC was typically 2 mm for the K^+K^- tracks, and K^+K^- events produced at the SC were clearly separated. Figure 1(b) shows the K^+K^- invariant mass distribution for the Cu target. A clear ϕ peak can be observed for the other targets as well. The measured mass and width of the ϕ meson are consistent with free ϕ mesons [12] within our detector system.

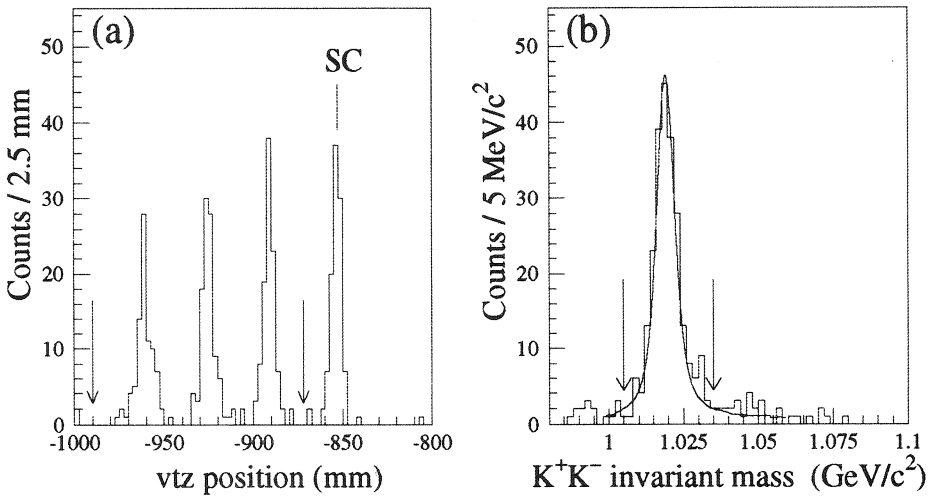

Fig.1. (a) Vertex position (*vtz*) distribution for K^+K^- events along the photon beam direction for Cu. Cut points to select the K^+K^- events generated at the target are indicated by the arrows. (b) K^+K^- invariant mass distribution for the Cu target. The solid curve shows the fitting results with free m_0 and Γ_0 parameters given in the text. Cut points to select the ϕ events are indicated by the arrows.

The ϕ meson events were selected by gating the ϕ meson peak in the K^+K^- invariant mass distribution from 1005 to 1035 MeV/c^2. The number of background events in the ϕ peak region, was estimated from the measured number of events in the region of 1050 to 1100 MeV/c^2 assuming that the background shape is the same as non-resonant K^+K^- invariant mass distributions. The fraction of the background events are small (5−7%). The background events due to the mis-identification of the particle were negligible.

Normalization for the photo-production cross section was made by taking into account the number of hits in the tagging counter, the attenuation of the photon flux in the target material, the number of target nuclei, the live time of data taking system, and the acceptance correction.

Measured momentum transfer square $|t|$ ranges up to 0.6 GeV^2/c^2. Figure 2(a) shows $\tilde{t} = |t| - |t|_{min}$ distribution of ϕ mesons for the C target, where $|t|_{min} = |t_{\theta=0^\circ}|$ was given for the proton at rest. When $\tilde{t}$ distribution was fitted with the exponential function $d\sigma/d\tilde{t} = C \exp(-b\tilde{t})$ in the region of $\tilde{t}$ = 0.0-0.5 GeV^2/c^2, the slope parameter b was obtained to be 3.6 ± 0.9, 4.5 ± 1.0, 3.1 ± 0.9, and 4.5 ± 1.0 (GeV^2/c^2)$^{-1}$

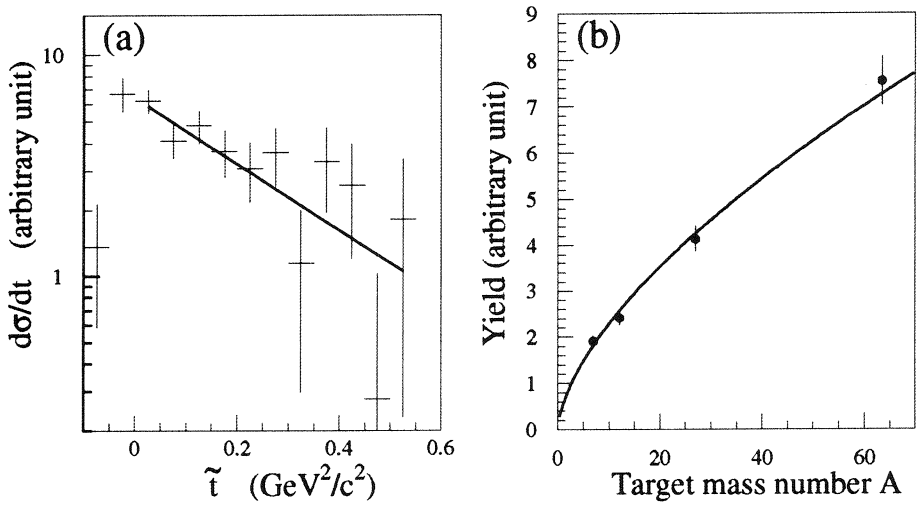

Fig.2. (a) $\tilde{t} = |t| - |t|_{\min}$ distribution for the C target together with an exponential fit of the form $d\sigma/dt = C \exp(-b\tilde{t})$. (b) Target mass number dependence of the ϕ meson photo-production from nuclei. The data points are compared with a solid curve using the parameterization $A^{0.63}$.

for Li, C, Al, and Cu, respectively. These slope parameters were consistent with the case of ϕ photo-production on the proton, $b \sim 3.38$ $(\mathrm{GeV}^2/c^2)^{-1}$ [13], within the error bars. When the mass number dependence of the yields were fitted with the standard parameterization as $\sigma_A = \sigma_0 A^{\alpha}$, $\alpha = 0.63 \pm 0.05$ was obtained assuming all the ϕ mesons are produced incoherently. Figure 2(b) shows the target mass number dependence of the ϕ meson photo-production from nuclei.

An optical model of the Glauber-type multiple scattering theory for incoherent production was applied to determine the total ϕ-N cross section [9]. In this model, the production cross section from a nucleus, $d\sigma_A/dt$, is described as

$$\frac{d\sigma_A}{dt} = A_{\mathrm{eff}} \frac{d\sigma_0}{dt}, \tag{1}$$

where A_{eff} stands for the effective nucleon number and $d\sigma_0/dt$ represents the production cross section on the nucleon. The effective nucleon number A_{eff} for ϕ photo-production is expressed as a function of the target mass number A, the total photon-nucleon cross section, $\sigma_{\gamma N}$, and ϕ-nucleon total cross section, $\sigma_{\phi N}$;

$$A_{\mathrm{eff}}(A, \sigma_{\gamma N}, \sigma_{\phi N}) = \frac{1}{\sigma_{\phi N} - \sigma_{\gamma N}} \int \left(e^{-\sigma_{\gamma N} T(\vec{b})} - e^{-\sigma_{\phi N} T(\vec{b})} \right) d^2 b, \tag{2}$$

$$T(\vec{b}) = A \int_{-\infty}^{+\infty} \rho(\vec{b}, z)\, dz,$$

where $\vec{b}$ stands for the impact vector of the incident photon, and ρ is the nucleon density of the target nucleus. The effect of quasi-elastic collision between the ϕ meson and the nucleon is not included in Eq. (1) since the direction and energy change of the ϕ meson is small thanks to the small direct ϕNN coupling [11]. Assuming the same $d\sigma_0/dt$ for the proton and the neutron, $\sigma_{\phi N}$ is derived from the target mass number dependence of the yields. The absolute values of the production cross sections, $d\sigma_A/dt$, are not necessary for determining $\sigma_{\phi N}$. The total γ-N cross section $\sigma_{\gamma N}$ was fixed to be 140 μb in the energy

range from 1.5 to 2.4 GeV [12]. The nucleon densities for the different target nuclei were given by normalizing the charge density distributions [14], where proton and neutron density distributions were assumed to have the same r-dependence. The branching ratio of $\phi \to K^+K^-$ was assumed to be the same for each target nucleus since almost all the ϕ mesons decayed outside the nucleus. The ϕ-N total cross section $\sigma_{\phi N}$ becomes $70.8^{+31.7}_{-19.0}$ mb assuming all the ϕ mesons are produced incoherently. This value is quite larger than other meson-nucleon total cross sections $\sigma_{\omega N}$, $\sigma_{\rho N}$, and $\sigma_{\eta N}$ [15].

It is reported in Ref. [11] that the ratio of the coherent to the incoherent process increases rapidly with increasing the incident photon energy, and that the contribution of the coherent process cannot be negligible especially for light nuclear targets. If the coherent process contributes for light targets more, it makes α small. Thus, it is necessary to exclude the coherent events in determining $\sigma_{\phi N}$ by utilizing the target mass number dependence of the ϕ meson yields. Final results will be presented elsewhere.

References

[1] T. Hatsuda and S.H. Lee: Phys. Rev. C **46** (1992) 34; H. Kuwabara and T. Hatsuda: Prog. Theor. Phys. **94** (1995) 1163; T. Hatsuda, H. Shiomi, and H. Kuwabara: Prog. Theor. Phys. **95** (1996) 1009.

[2] E. Oset, M.J. Vicente Vacas, H. Toki, and A. Ramos: Phys. Lett. B **508** (2001) 237; E. Oset and A. Ramos: Nucl. Phys. **A679** (2001) 616.

[3] D. Cabrera and M.J. Vicente Vacas: Phys. Rev. C **67** (2003) 045203.

[4] P. Mühlich, T. Falter, C. Greiner, J. Lehr, M. Post, and U. Mosel: Phys. Rev. C **67** (2003) 024605.

[5] H. En'yo *et al.*: Nucl. Phys. **A670** (2000) 182c; H. En'yo *et al.*: Prog. Theor. Phys. Suppl. **149** (2003) 49; K. Ozawa *et al.*: Phys. Rev. Lett. **86** (2001) 5019.

[6] E-802 Collaboration, Y. Akiba *et al.*: Phys. Rev. Lett. **76** (1996) 2021.

[7] G. McClellan *et al.*: Phys. Rev. Lett. **25** (1971) 1593.

[8] H.-J. Behrend *et al.*: Phys. Lett. B **56** (1975) 408.

[9] K.S. Kölbig and B. Margolis: Nucl. Phys. **B6** (1968) 85; B. Margolis: Phys. Lett. B **26** (1968) 524.

[10] T. Nakano *et al.*: Nucl. Phys. **A684** (2001) 71c; T. Nakano: Nucl. Phys. **A721** (2003) 112c; T. Nakano *et al.*: Phys. Rev. Lett. **91** (2003) 012002; R.G.T. Zegers *et al.*: Phys. Rev. Lett. **91** (2003) 092001.

[11] D. Cabrera, L. Roca, E. Oset, H. Toki, and M.J. Vicente Vacas: Nucl. Phys. **A733** (2004) 130.

[12] K. Hagiwara *et al.*: Phys. Rev. D **66** (2002) 010001.

[13] T. Mibe: Doctor thesis, Osaka University (2004).

[14] H. de Vries *et al.*, Atom. Data Nucl. Data Tabl. **36** (1987) 495.

[15] T.H. Bauer, R.D. Spital, D.R. Yannie, and F.M. Pipkin: Rev. Mod. Phys. **50** (1978) 261, and references therein; M. Effenberger and A. Sibirtsev: Nucl. Phys. **A632** (1998) 99.

Ⅱ. Radiochemistry

(LNS Experiment : #2847, #2501)

光量子放射化分析法による大気浮遊粒子中の炭素の定量

大浦泰嗣，永幡　健，海老原充

東京都立大学大学院理学研究科　(192-0397　東京都八王子市南大沢 1-1)

Photon Activation Analysis of Carbon in Atmospheric Suspended Particulate Matters

Y. Oura, T. Nagahata, and M. Ebihara

Graduate School of Science, Tokyo Metropolitan University, 1-1 Minami-Ohsawa, Hachiouji, Tokyo 192-0372

Carbon contents in atmospheric suspended particulate matters (PM_{10}) collected at Hachioji, Tokyo in 2002 and 2003 were determined nondestructively by instrimental photon activation analysis. Although paticulate concentartions were almost constant (20 - 35 $\mu g/m^3$), carbon contents were fluctuated from 3.7 to 11 $\mu g/m^3$. It is suggested that particulates collected at Hachioji are composed of several sources with various contents.

§1．はじめに

最近，特に首都圏ではディーゼル車からの排気微粒子が健康に重大な被害を与えるということで問題になっている。大気中には様々な粒径の粒子が漂っているが，空気動力学径10 μm 以下の粒子（PM_{10}），中でも特に2.5 μm 以下の粒子（$PM_{2.5}$）の日別濃度変動が日別死亡率と相関することが報告され関心を集めている。我々は PM_{10} 大気浮遊粒子（SPM）をポリカーボネートフィルターで捕集し，その元素組成を中性子放射化分析法（NAA）にて調べている。しかしながら，SPM の主要元素の一つで，自動車からの排出粒子がその主な起源の一つであると考えられる炭素は，NAA では定量できない。そこで，光量子放射化分析法による SPM 中の炭素濃度定量を試みたので報告する。

§2．実　　験

SPM の採集は，東京都八王子市（都心から西へ約40 km）にある東京都立大学理学部棟屋上にて隔週（毎月第二週と第四週）行なった。ニールフィルターホルダーに10 μm 以上の径の粒子をカットするインパクターと石英製フィルタ（QMA, Whatman）をセットし，流量16.7 ℓ/min にて大気を約5日間吸引し，SPM を濾過した。

採集された粒子重量を秤量後，直径10mm の円盤状に２枚切り出し，粒子採集面を向き合わせて Al 箔で包み，照射用試料とした。また，標準試料である国立環境研究所が発行している自動車排出粒子 NIES No.8 と米国標準局が発行している瀝青炭 NIST 1632c もそれぞれ数 mg を直径10mm の石英フィルターではさみ，Al 箔で包んで試料とした。炭素定量用の比較標準試料として Al 箔で包んだ直径10mm の炭素板（約

20mg）を用いた。これらをスタック状にしてフラックス補正用金箔とともに石英管に封入し，最大エネルギー25MeVの制動放射線で20分間照射した。照射エネルギーは炭素定量に用いる $^{12}C(\gamma, n)^{11}C$ 反応の妨害反応である $^{14}N(\gamma, p2n)^{11}C$ と $^{16}O(\gamma, \alpha n)^{11}C$（Q値はそれぞれ−31.2 MeVと−25.7 MeV）が起きないように設定した。

照射後，ただちに試料をAl箔からポリ袋に移し，厚さ1 mmの銅板ではさんでγ線を5分間測定した。炭素定量に用いる ^{11}C は純 β^+ 壊変核種でありγ線を放出しないため，12時間から24時間測定を繰り返し，壊変曲線から ^{11}C からの511 keV消滅γ線の純度を確認した。

§3．結果と考察

第1図にSPMのγ線スペクトルの一例を，第2図に511keV消滅γ線の壊変曲線の一例を示す。511 keV消滅γ線以外にいくつかの誘導核種からのγ線が検出された。観測された消滅γ線の壊変曲線は ^{11}C，^{18}F，ならびに ^{24}Na の3核種の寄与の和として説明でき，これら以外の核種からの寄与は無視し得る。得られた壊変曲線を ^{11}C，^{18}F，ならびに ^{24}Na の3成分に分解した結果を点線にて第2図中に示した。^{24}Na（ならびにバックグランドの511 keVγ線）の寄与は照射終了4時間までは1％以下でありほとんど無視できるが，^{18}F からの寄与は試料によるが照射終了後で約10％であり，^{11}C 正味の計数率を得るには補正が必要であった。また，石英フィルターブランクの寄与が約25％あったので補正した。

標準試料NIST　1632cの炭素定量を繰り返し行なった。本試料のNISTによる炭素濃度参照値は77.45±0.25％で，本研究による定量値と参照値との比を第3図に示した。小さい定量値から大きい定量値の順で並べたが，ほとんどの定量値は参考値の±10％以内の範囲で得られた。10回の平均値は0.99（標準偏差は0.11）で，参考値と非常によく一致した。ばらつきが少し大きいが，原因の一つは少量試料（数 mg）の照射形態にあると考えている。現在，石英フィルターの中心部に試料をのせて，別の石英フィルターではさんで照射用試料としているが，比較標準試料の炭素板（10mmφ）やフラックス補正用金箔（10mmφ）と面積が異なるためにフラックスが正しく補正されなかった可能性がある。今後，照射形態を改善する必要がある。標準試料NIES　No.8の炭素濃度は推奨値・参考値ともに公表されていないが，繰り返し分析の平均値として69±9％を得た。

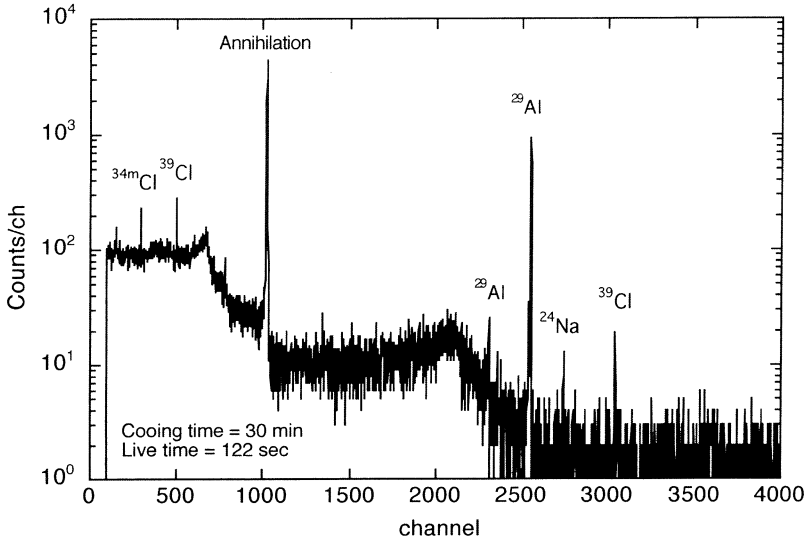

第1図　大気浮遊粒子のγ線スペクトルの一例。

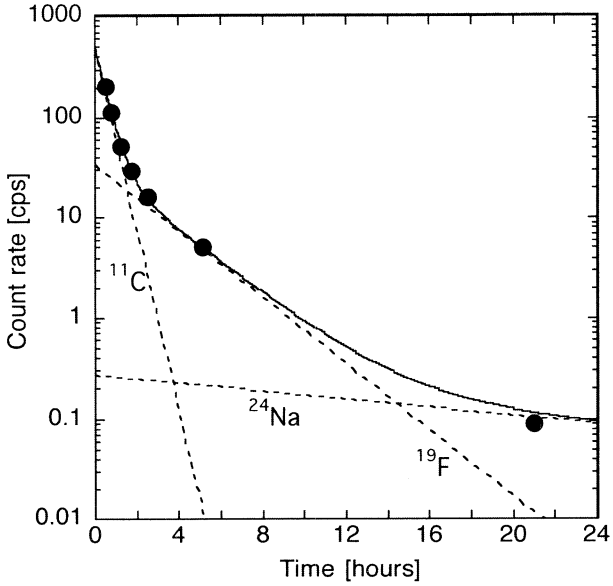

第２図　511 keV消滅γ線の壊変曲線の一例。^{11}C, ^{18}F, ^{24}Na の３成分とすると観測値をよく再現できる（実線）。点線は観測値を各成分に分解したときの壊変曲線。

SPM の採集は, 2002年８月から定期的に行っている。2002年８月から2003年12月までに捕集した SPM (PM_{10}) の粒子濃度（$\mu g/m^3$）を第４図に示した。粒子濃度は通常20～35 $\mu g/m^3$ の範囲でほぼ一定で，2002年2/24-3/1，3/25-3/29，2003年6/26-6/28のように一時的に高い粒子濃度が観測された。

本研究で得た炭素濃度の経時変化を第５図に示す。大気中の炭素重量濃度を●で，捕集された粒子中の炭素重量濃度を○で示した。大気中濃度の経時変化と粒子中濃度の経時変化の様子は一部を除いて非常によく一致した。一時的に粒子濃度が高かった時期（2002年11/19-23，2003年2/24-3/1，6/26-28）は粒子中

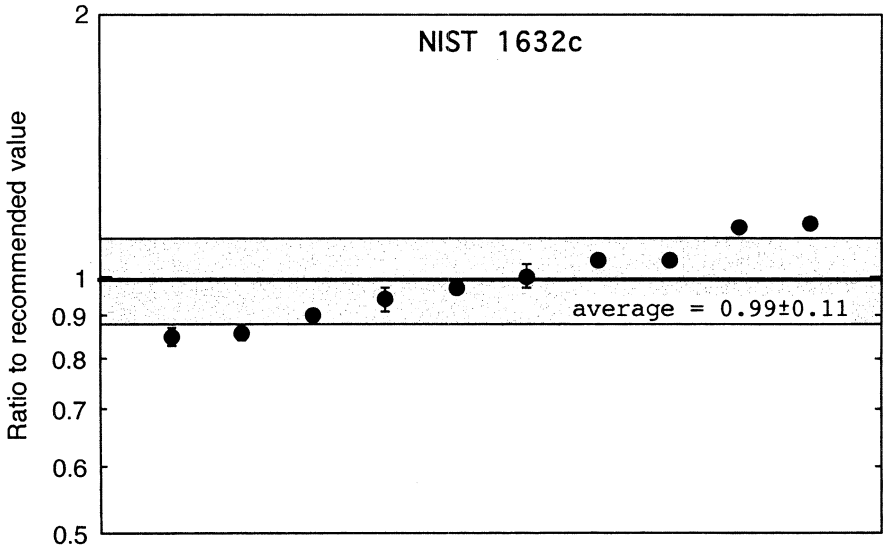

第３図　標準試料 NIST　1632c の炭素濃度定量結果。推奨値77.45％との比で示した。実線は定量値の平均値，網部分はその標準偏差（1σ）を示す。

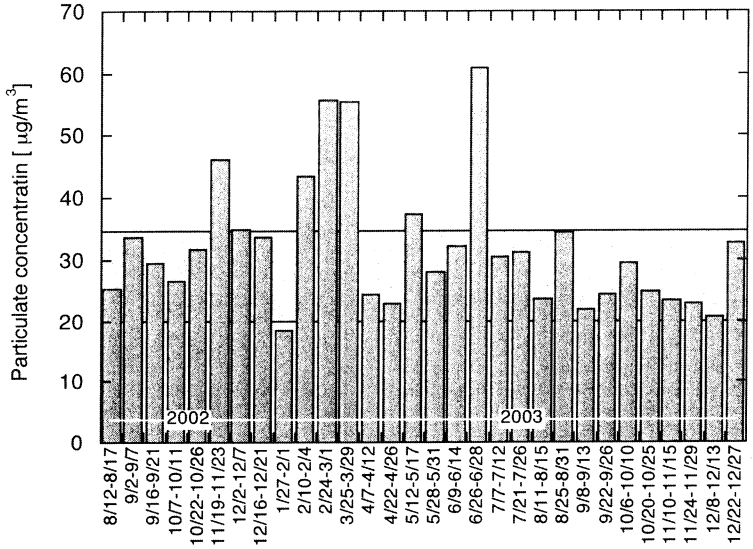

第４図　2002年から2003年に採集した PM_{10} 粒子濃度。粒子濃度は年間を通じて網で示した20～30 $\mu g/m^3$ の範囲で一定であった。

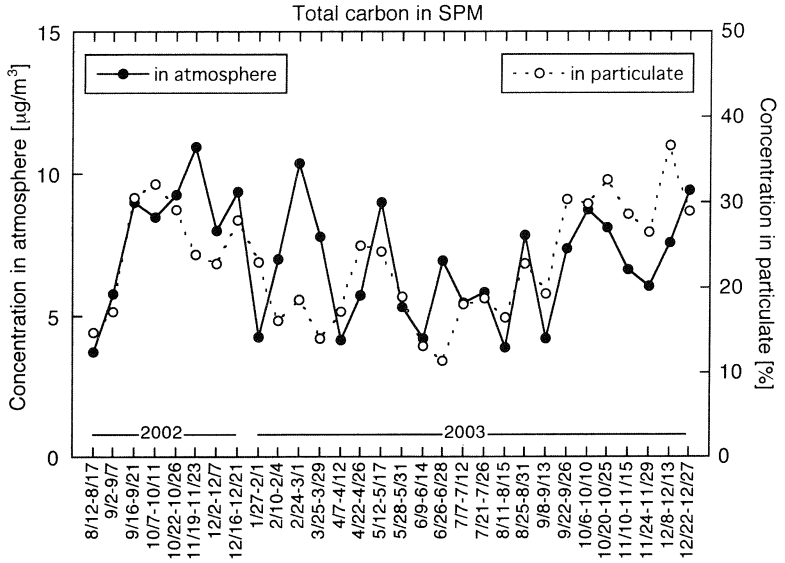

第５図　2002年から2003年に採集した PM_{10} 粒子中の炭素濃度。大気中の炭素重量濃度を●（左軸）で，捕集粒子中の炭素重量濃度を○（右軸）で示した。

濃度が相対的に低くなり，粒子中濃度の経時変化は大気中濃度の経時変化とは一致しなかった。炭素含有量が小さい粒子のみが相対的に増加したためと考えられる。粒子濃度は20～35 $\mu g/m^3$ の範囲でほぼ一定であるのに対し，大気中炭素濃度は3.7から11 $\mu g/m^3$（11から37％）まで約３倍変化した。SPM には多様な起源の粒子が混在しているが，その構成比は元素組成に反映される。炭素重量濃度の大きな変化は，同一地点においても起源の異なる粒子の構成比は一定ではないことを示唆している。

謝　辞

本研究を行うにあたり良質な電子ビームを供給していただいた東北大学原子核理学研究施設マシングループの方々と試料照射ならびに放射線測定でお世話になった大槻勤助教授と結城秀行博士に深く感謝する。

Ⅲ. Accelerator, Synchrotron Radiation, and Instrumentation

(LNS Experiment : #2452, #2468, #2496)

フォトニック結晶からのスミス・パーセル放射と未解明放射の観測

神戸　亮[1], 近藤泰洋[1], 大原直人[1], 清水俊明[1], 宮嵜博司[1], 柴田行男[2],
伊師君弘[2], 蔦谷　勉[2], 日出富士雄[3], 瀬川勇三郎[4,5], 山本貴一[4],
堀内典明[4], 渡辺良祐[4], 大高一雄[6], 山口修一[7]

[1]東北大学大学院工学研究科（980-8579　仙台市青葉区荒巻字青葉 08）
[2]東北大学多元物質科学研究所（980-8577　仙台市青葉区片平 2-1-1）
[3]東北大学原子核理学研究施設（982-0826　仙台市太白区三神峯 1-2-1）
[4]理化学研究所フォトダイナミクスセンター（980-0845　仙台市青葉区荒巻字青葉 519-1399）
[5]東北大学大学院理学研究科（980-8578　仙台市青葉区荒巻字青葉）
[6]千葉大学先進科学教育センター（263-8522　千葉市稲毛区弥生町 1-33）
[7]千葉大学工学部（263-8522　千葉市稲毛区弥生町 1-33）

Observation of Smith-Purcell Radiation and Unknown Radiation from a Photonic Crystal

M. Kambe[1], Y. Kondo[1], N. Ohara[1], T. Shimizu[1], H. Miyazaki[1], Y. Shibata[2],
K. Ishi[2], T. Tsutaya[2], F. Hinode[3], Y. Segawa[4,5], K. Yamamoto[4],
N. Horiuchi[4], R. Watanabe[4], K. Ohtaka[6], and S. Yamaguchi[7]

[1]*Department of Applied Physics, Advanced School of Engineering, Tohoku University, Aramaki, Aoba-ku, Sendai 980-8579*
[2]*Institute of Multidisciplinary Research for Advanced Materials, Tohoku University, 2-1-1 Katahira, Aoba-ku, Sendai 980-8577*
[3]*Laboratory of Nuclear Science, Tohoku University, 1-2-1 Mikamine, Taihaku-ku, Sendai 982-0826*
[4]*Photodynamics Research Center, The Institute of Physical and Chemical Research (RIKEN), 519-1399 Aoba, Aramaki, Aoba-ku, Sendai 980-0845*
[5]*Department of Physics, Graduate School of Science, Tohoku University, Aoba, Aramaki, Aoba-ku, Sendai 980-8578*
[6]*Center for Frontier Science, Chiba University, 1-33 Yayoi-cho, Inage-ku, Chiba 982-0826*
[7]*Graduate School of Science and Technology, Chiba University, 1-33 Yayoi-cho, Inage-ku, Chiba 982-0826*

The normal and unknown Smith-Purcell radiation (SPR) from samples that were different in periods, edge structure, and number of layer has been studied. Comparing with theoretical calculation of photonic bands, it has been found that unknown radiation as well as SPR lies on the photonic bands. The intensity of unknown radiation is enhanced by increase of the number of sample layer. Therefore, this unknown radiation may be emissions from excited photonic band modes in the photonic crystal.

フォトニック結晶から放射されるスミス・パーセル放射（SPR）と従来の理論では説明できない放射の起源を明らかにすべく，周期構造，端面構造，層数の異なるサンプルについて放射を観測した。理論計算との比較から正規のスミス・パーセル放射，未解明放射ともにフォトニックバンド上にあることがわかった。層数を増やすと未解明放射が増強することから，内部で特定のフォトニックバンドモードが励起されて放射されていると考えられる。

§1．はじめに

スミス･パーセル放射（以下 SPR と記す）は1953年，金属回折格子を用いて観測され，Smith と Purcell により報告された [1]。我々のグループは金属回折格子をフォトニック結晶に置き替え，フォトニックバンド構造の観測や効率の良い光変換への応用を視野にフォトニック結晶からのスミス・パーセル放射の基礎研究を進めてきた。前号 [2]，前々号 [3]において，本グループはフォトニック結晶からの SPR の観測に成功し，SPR ではない放射も観測されることについて述べた。特に前回は，この SPR ではない放射の起源がサンプルの撓みでないことを示した。また２層の実験から，理論的予測 [4] の通り，層が増えるとシャープで高強度な放射が得られるであろうことも示した。ただしこれまでは三角格子の１方向からしか測定してこなかった。そこで今回は周期構造，サンプルの端面，層数の異なるサンプルからのスミス・パーセル放射について報告する。

§2．フォトニック結晶からの SPR と未解明放射ライン

フォトニック結晶からの SPR は，次の条件を全て満たしたものである。

１．(k，ω）空間でライトコーンの内側にある。

２．フォトニックバンド上である。

３．電子から放射される減衰波の分散線をフォトニック結晶の逆格子ベクトルの線形和だけシフトした分散線上にある。

１は観測可能な進行波に要請される条件である。２は，フォトニック結晶内にはフォトニックバンド上の光しか存在できないことによる制約である。これにより，フォトニックバンドを反映した SPR が得られることになる。

３は，ウムクラップ散乱によって減衰波がライトコーン内にシフトすることで観測可能な進行波になることである。これらを模式的に表したのが第１図である（詳細は [3，4]）。

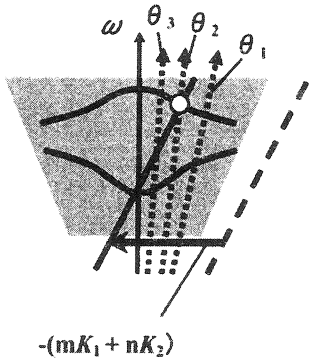

第１図　(k，ω）空間における散乱過程の模式図。減衰波の分散直線（破線）がウムクラップ散乱をうけ，ライトコーン（影をつけた部分）の内部へシフトし，H_{mm}（実線）となる。実曲線はフォトニックバンドを模式的に表したもの。点線矢印は放射角度θを固定したときのスペクトルに相当する。

電子の速度 v が光速 c に近い場合（$v/c\sim 1$），H_{mm} 分散線はほとんどライトコーンの境界線と平行になる。つまり，この条件で SPR を観測するとライトコーンの境界線と平行な H_{mm} 分散線が等間隔でててくると考えられる。この正規のラインを以降シフトの小さい順に H_1，H_2，H_3，･･･と呼ぶことにする。しかし，これまでの実験では，ライトコーンの境界線より緩やかな傾きの分散線も観測された。我々はその起源を探ってきて，サンプルの撓みによるものではないことは分かった。そこで，今回はこの SPR ではない放射の起源を考えるうえで，周期構造，端面構造，層数の効果に注目し放射ラインの振る舞いを追った。

§3．実　　験

測定系の基本構成は以下に示す改善点の他は前回，前々回の報告と同様である [2,3]。

・チャンバーの内部にエコソーブを貼り，迷光が発生しないようにした。これにより S/N 比が向上した。

・微弱信号検出を Box car 積分器で，A/D 変換を Data Acquisition(DAQ) ボードで行なうようにし，測定時間を 約1/2に 短縮し た。(以前は Lock-in Amp. とデジボルで行なっていた。)

フォトニック結晶は直径3.2mm のテフロン球（$\varepsilon=2.05$）を配列し，粘着テープで支持して作成した。多層サンプルの場合は1層サンプルを重ねて多層とした。測定したサンプルを第1表に示し，構造と電子の通る方位を第2図に示す。

第1表　測定サンプル一覧

サンプル形状	層数	ビーム入射方位
三角格子	1	Γ - M
三角格子	2	Γ - M
三角格子	4	Γ - M
三角格子	1	Γ - K
三角格子斜めカット	1	Γ - K
四角格子	1	Γ - X
四角格子	4	Γ - X

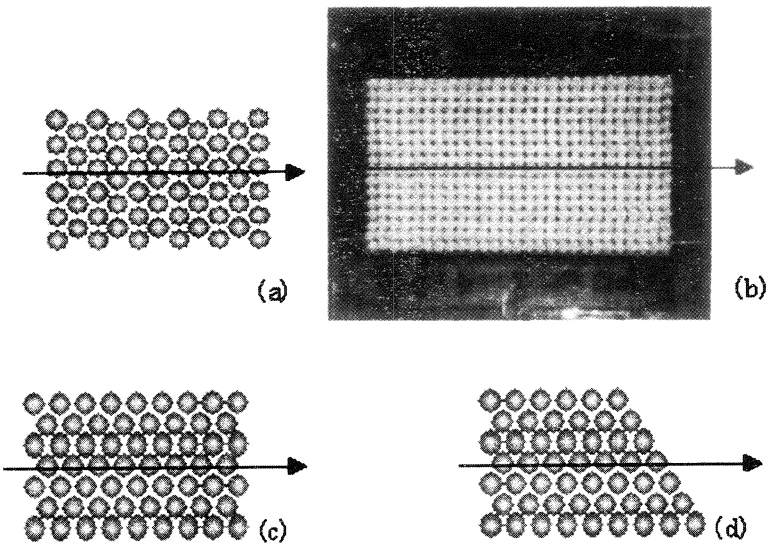

第2図　(a)三角格子Γ - M 入射配置，(b)四角格子Γ - X 入射配置，(c)三角格子Γ -K 入射配置，(d)三角格子斜めカットΓ - K 入射配置（矢印は電子線の入射方向)。

§4．実験結果と考察

4-1. 三角格子　Γ - M 入射配置　1，2，4層

第3図(a)，(c)，(d)に層数を変えて，SPR スペクトルを観測した結果を示す。これらより増強されるのは未

解明放射ライン上の特定の放射であることがわかる。第３図(b)に示した１層の場合のバンド計算との比較より，全ての放射ピークがバンドとH_1ラインの交点であることが分かる。また，79％放射ラインのピークもバンドに乗ることが分かる。このことから，未解明放射もフォトニックバンドからの励起放射であると考えられる。

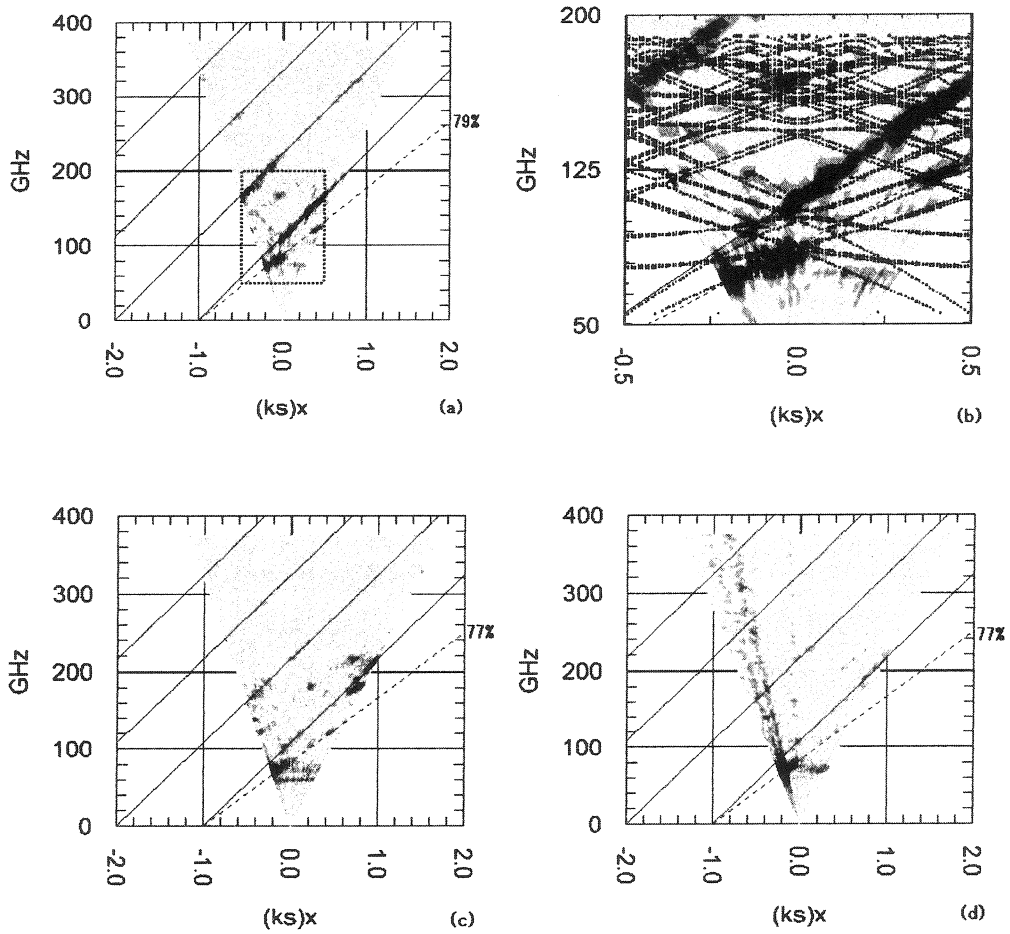

第３図　テフロン球Γ-M入射配置の角度依存スペクトル。(a)１層の測定結果，(b)１層の点線四角内部とバンド計算との比較，(c)２層，(d)４層の測定結果（横軸は逆格子ベクトルで規格化している）。

４-2. 三角格子　Γ-K入射配置

第４図(a)に示すように，Γ-K入射配置においては，これまで同様の未解明放射ラインとともに，理論上ありえない正負逆の傾きのライン（以下$-H_1$ラインと呼ぶこととする）に乗る放射が観測された。理論計算との比較が第４図(b)である。いずれの放射もバンドに乗っている。我々は先の$-H_1$ラインに注目し，その起源を端面の反射と仮定し，端面を斜めに配列したサンプルでその効果を無くそうと試みた。その結果，第４図(c)のようにラインが消えたように見えた。しかし，ビーム条件の違い，サンプルサイズ短縮による放射強度の減少があるため端面による効果とは断定できない。また，次に示す四角格子の１層にも同様のラインが見られるようである。このことから，Γ-KとΓ-X入射配置に共通するテフロン球のビーム軸方向の連続性が原因ではないかとも考えられる。

４-3. 四角格子　Γ-X入射配置　１，４層

Γ-K入射配置でも言及したが，四角格子のΓ-X入射配置でも$-H_2$ラインに乗る放射が観測された（第５図(a)）。また，４層にすると，他のサンプルと同様に未解明放射ラインの特定の放射のみが増強された（第

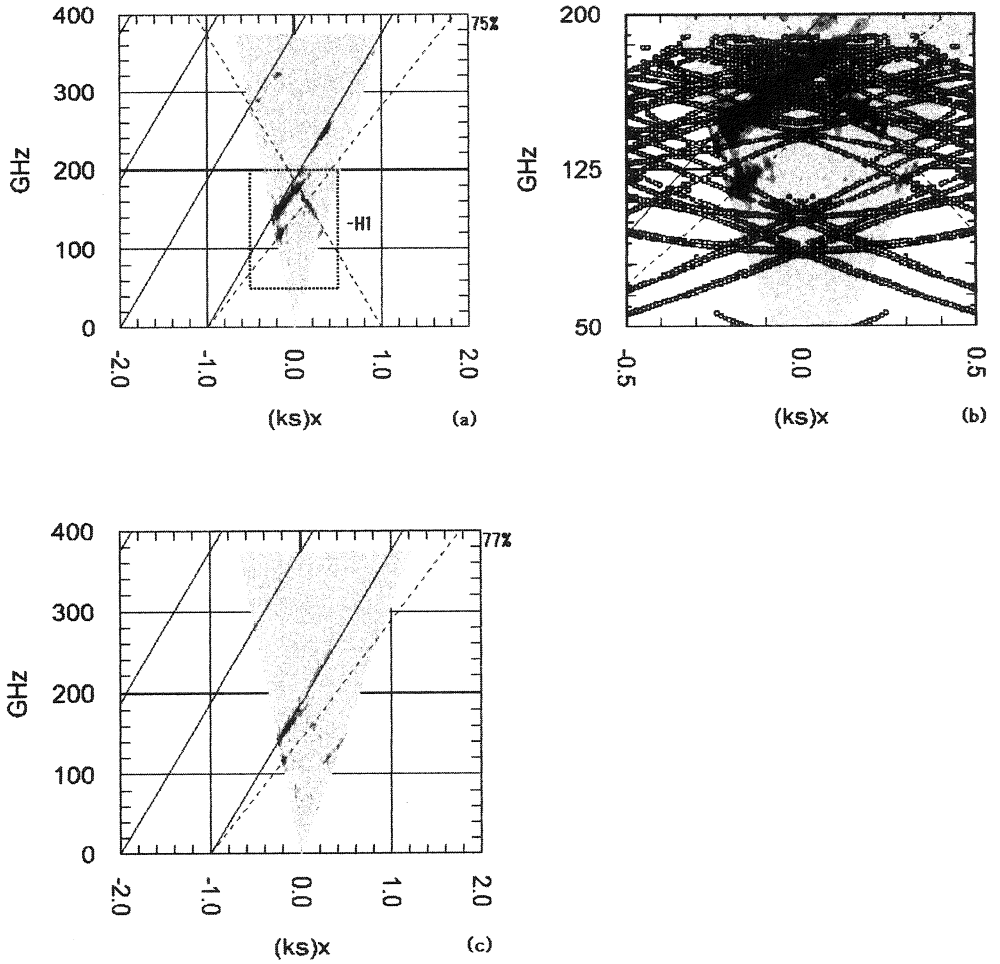

第４図　テフロン球Γ-K入射配置の角度依存スペクトル。(a) 1 層の測定結果，(b) 1 層の点線四角内部とバンド計算との比較，(c) 1 層端面斜めカットの測定結果（横軸は逆格子ベクトルで規格化している）。

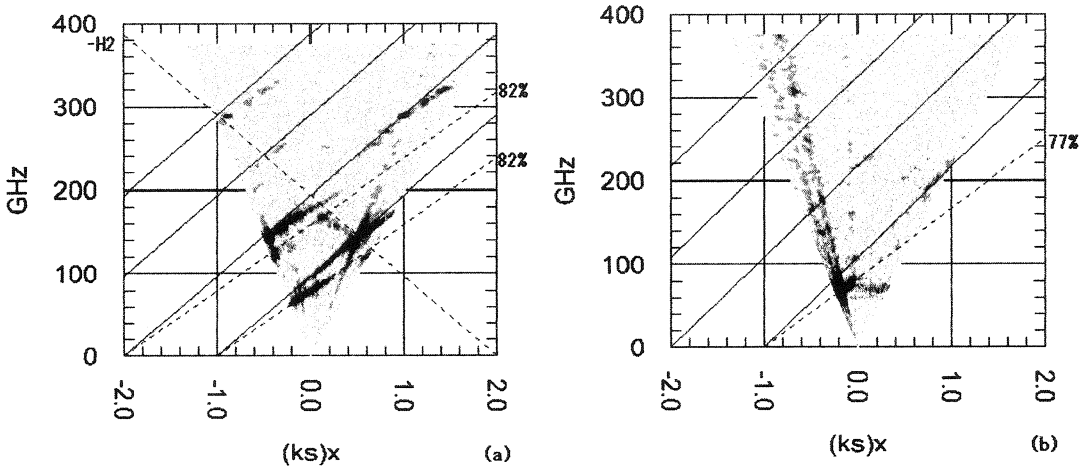

第５図　テフロン球Γ-X入射配置の角度依存スペクトル。(a) 1 層，(b) 4 層の測定結果（横軸は逆格子ベクトルで規格化している）。

５図(b))。こうして，未解明放射は層数（バルクの割合）が増えると増強されることが示された。よって，内部で特定のフォトニックバンドモードが励起され放射していると考えられる。

§5. まとめ

前回の報告でも触れたように，層を増やすと確かに強度は増すことが分かった。しかし増強されるのは正規のスミス・パーセル放射ではなく，未解明放射ラインの一部であった。すなわち，未解明放射ラインは内部で励起されるフォトニックバンドモードの放射であり，ゆえにバルクの割合が増えると増強すると考えられる。

参　考　文　献

[1] S.J. Smith and E.M. Purcell : Phys. Rev. **92** (1953) 1069.

[2] N. Ohara *et al.*: Research Report of LNS **36** (2003) 115.

[3] K. Yamamoto *et al.*: Research Report of LNS **35** (2002) 90.

[4] K. Ohtaka and S. Yamaguti : Optics and Quantum Electronics **34** (2002) 235.

リナック冷却系の現状及び最近の故障例とその対策

高橋重伸，河合正之，浜　広幸

東北大学大学院理学研究科　附属原子核理学研究施設　（982-0826　仙台市太白区三神峯 1-2-2）

Present Status of the LINAC Cooling System : Recent Malfunction Examples and Measures

S. Takahashi, M. Kawai, and H. Hama

Laboratory of Nuclear Science, Tohoku University, 1-2-1 Mikamine, Taihaku-ku, Sendai 982-0826

The cooling system in LNS has continued to operate for 38 years to support a lot of experiments. However, recently, the water leaking by the corrosion occurred at weldeng parts and aluminum gaskets for pipe joint. Therefore, the degradation of the performance of the system is remarkable. In this report we illustrate about the malfunction examples and the measures of this system for recent 3 years.

§1．概　　要

電子リナックは原子核の研究，STBリングの入射用，200MeV パルス実験，RI 製造など多目的実験を行っている。その性能は，加速エネルギー，取り出し平均ビーム電流について，1 系は15～65MeV, 150 μA, 2，3 系では100～220MeV，10 μA，パルス繰り返し300pps，最大 Duty Factor は0.1％である。

冷却系は，リナックの安定運転のために，ビーム ON－OFF 時の熱負荷変動あるいは気象条件の温度変化があっても，それぞれの循環系の冷却水をある一定温度に冷却保持する必要がある。冷却設備は38年間にわたる High Duty Beam 実験などによる放射線損傷，冷却水の汚れ，腐食や振動，ヒートサイクルに伴う経年変化により損傷を受けているが，多くの機器配管を更新あるいは修理整備をして現在でも共同利用実験に供している。特に，この 3 年以内の故障原因を検討すると，設備の末期故障でもある水漏れが多発している。本報告では，各水系の特徴，メンテナンス状況，最近の故障例及びその対策（●で示す。）について述べる。第 1 図に冷却系の系統図を示す。

§2．純水温度調節系

加速管水系，導波管水系のことで，水温40±0.1℃，循環水導電率は 1 ～ 2 μS/cm である。高周波電力伝送損失の発熱除去，温度変化による位相変動防止のために微細温度調節が必要である。

2.1　加速管（ＡＣＣ）水系

21本の加速管にそれぞれ60 L/min を循環する。圧力は 1 MPa である。ポンプは10年前にメカニカルシール部からの水漏れにより同型式のポンプに更新した。同時期に吐き出し電動バルブに変更し，ポンプ起動・停止と同期して開閉するようにしてある。A 3 加速管にはテスト用としてフロート式流量計が20年前から 2 台付いているが，放射線損傷により硬質ガラス部が黒くなり，また，NBR ゴムパッキンを使用しているた

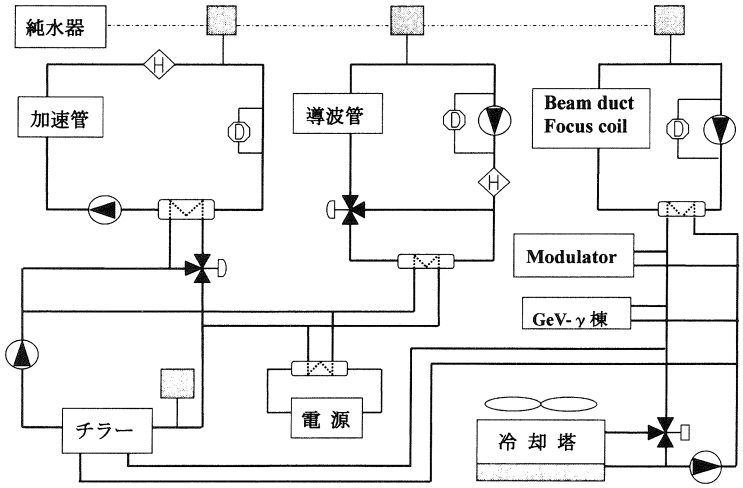

第１図　リナック冷却系ブロック図【H：昇温用ヒータ，D：デミネラライザ（フィルタ)】。
GeV-γ棟冷却系は冷却塔水系から200L/min 程度分流している。

めに交換が必要である。将来は可動部のない構造の渦流量計を取り付けたいと考えている。

●Honey-Well 社のパドル式フロースイッチ（FS4J-1）を21台使用しているが，SUS 製パドル部が高流速水の振動により折れる故障が年３～４個程度あった。当時の修理法はパドルを２枚重ねに改造して使っていたが，数年前からパドルの厚みが大きくなったので，現在は購入品を１枚のまま使用している。

●2004年７月，加速管接続用の SUS と銅管溶接構造の水ジャケットが、その溶接部から水漏れした。旧型のもので，SUS 管と銅管を銀ロー付けしてあるが，溶接しろが少なく，配管振動により亀裂が入り易い。対策は，両材質に親和性のある真鍮管を両管の間に入れ，補強溶接したジャケットに交換した。この配管の故障は10年前までは多発していたが在庫予備品があったので，短時間の修理で完了した。この水漏れの際，フロースイッチ作動によりフェイルセーフ機能が働き，ポンプ停止及びバルブ閉止は自動作動された。

●2004年９月，水位レベルセンサの動作不良により，ポンプ起動ができなくなった。このセンサは，純水タンクのビニール製連通管に取り付けられていて，静電容量の変化を検知するものである。検知感度調整ネジがあるが，室温や湿度の変化により感度が変化し誤動作することがある。レベル検知方式はフロート式，圧力式，超音波式などがあり，信頼性の高いセンサに交換していくようにしたいと考えている。

2.2　導波管（Wave Guide）水系

圧力0. 35 MPa，総流量300 L/min，導電率１μS/cm の水系である。矩形導波管（以後，WG と言う。）に溶接されている水ジャケット部のみを循環するので流路構造がシンプルであり，循環純水の純度低下が少なく一番きれいな水が流れている。しかし，この１～２年は水漏れが頻発していて，これまでとは違った溶接箇所の漏水が発生している。ハンダ溶接材の純水溶出が原因であり，WG の銅管細管路の接続の全てがこの溶接方法であり，その接続箇所は数百以上にも上り，漏水する恐れのある箇所は非常に多い。そのための簡易修理対策として，約20年前より，N２型シンフレックス管を使用している。この管材を用いる理由は，溶接が不要，Swagelok 継ぎ手より安価，銅管よりも熱の発散が少ない，屈曲可能であるために配管経路を自由に敷設できる，配管や継ぎ手の着脱が簡易などの利点がある。

継ぎ手部分の口径が銅管（15φ）より小さくなるが，流量は８L/min 以下であり問題はない。WG にはフレアオス継ぎ手が溶接されていて，その両管材の変換が面倒であったので，フレア継ぎ手とシンフレックス管の変換にフレア銅管を使わない方法を2004年９月から試験的に行っている。第２図の写真のように，直接

フレア袋ナットにRCネジでタッピングして，1/2シンフレックス管に変換している。銅管フレアが要らない，溶接作業が不要，モジュレータ裏側などの狭隘場所の配管接続におけるメンテナンス空間確保などに有用であると考えている。このシンフレックス管は，本体室A部加速管の中間部においてモード変換器冷却用ジャケットに5年間の使用実績があり，修理部分は数10箇所に上る。しかし，放射線量が高い場所，例えばB部ライナック入り口や出口のシンフレックス管は放射線損傷により硬化し，折れ易くなるために，5年以内の交換が必要と思われる。これらの箇所においては，緊急修理時以外は，従来接続方式の銅管接続にしている。WGポンプは2001年，メカニカルシール部の水漏れにより同形式のポンプに更新した。クライストロン室のオリフィス型フロースイッチは当初のものを現在も使用しているが，更新時期に来ている。最近の故障例としては，以下のものが挙げられる。

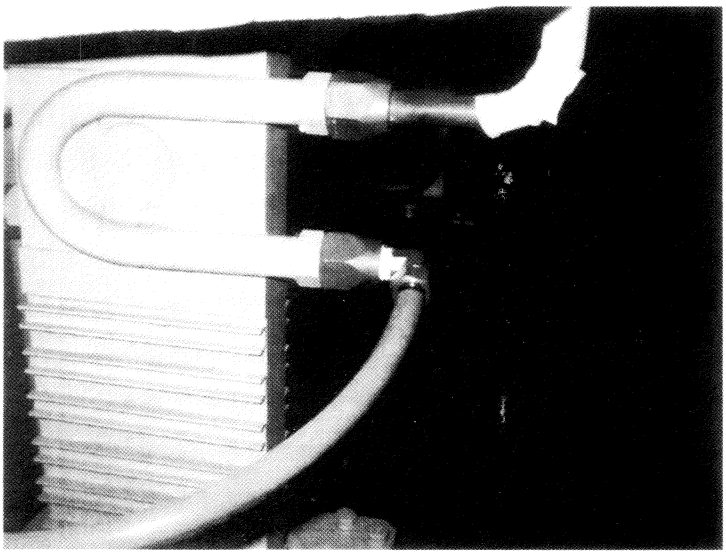

第2図　N2型シンフレックス管と改造フレアナットの接続。

●2003年4月，フロースイッチを殺したまま，修理のために流路を閉じて昇温運転を開始した。このためにフィルタ部アクリル流量計が水温上昇により溶融破損した。インターロック機能を殺した事が原因で発生した事故であり，フェイルセーフ対策の充実が必要である。

●WG本体と水ジャケットの溶接部，水ジャケット内のピンホール，あるいはジャケット部とフレア継ぎ手のハンダ溶接部からの水漏れ，フレア継ぎ手接続部における銅フレア部の亀裂による水漏れがあったが，今までは溶接箇所からの漏水は少なかった。

●2004年夏には，配管室設置の流量計の鉛パッキン部（1台につき2箇所ある）からの水漏れ，あるいは染み出し傾向が見られたので，A部流量計を8箇所交換，B部流量計12箇所は撤去し，ソケット接続としてある。新規流量計は安価であり，縦－横自在取り付け可能で，パッキンはNBRであるが，配管室はリナック本体側とコンクリート壁で仕切られているので，10年程度は問題なく使用できるものと考えている。この新A部流量計により2箇所，流量低下場所が見つかったが，原因や影響について調査中である。

§3．純水粗温度調節系

3.1　BF（Beam-duct・Focus-coil）水系

（20～30）±1.5℃，圧力0.7Mpa，循環水導電率1～2 μS/cmである。水質の劣化を防ぐ為にデミネライザが装備されていて，総循環水量の3％程度を分流・浄化している。BF水系は，リナック本体室や各実験室内を網目のように配管されていて，真空ダクト，分析スリット，各系偏向電磁石，集束コイル（A1加速管のみ）及び第1，第2実験室の熱負荷を冷却する。配管経路が一番長く，放射線損傷による影響も多い。また様々な実験装置が接続されており，水系内も汚れ易い。そのために冷却水の導電率の管理は重要である。第1実験室でのRI製造に使用される照射用ボートの冷却のように，直接ビームが照射され，水系内を汚染する場合には，BF水系から分離し別水系にしている。（この他の分離水系は，STBリング水系，STB電源水系，TAG－X水系等がある。）16年前にアルミ真空ダクト（AD6など）にアルミ製の水ジャケットをネジ

で取り付けてあるが，現在まで問題は起こっていない。放射線損傷による劣化の激しいものにはゴム，プラスチック，テフロンなどの高分子化合物，銅配管，ガラスがあり，フローメータやフロースイッチ等は，放射線の高い場所を避けてピット内や配管室など直接放射線を受けない場所に設置している。

●初段加速管A1の集束コイル用配管は，編組材入りのU字型高圧ゴムホースを使用しているが，放射線損傷により2～3年程度でゴムが硬化し亀裂が入り，水漏れが起こる。セラミックス付き銅管に更新予定だが，接続方法を検討中である。加速管集束コイルはA1のみで使用されている。

●スリットは1ヘッド（片側）あたり30 L/min を直列に通水しているが，残留放射線が非常に強いため，修理しにくい箇所である。2003年，SD1の銅製ヘッドから真空側に水が染み出し，圧力の関係で凍結凝固した。ヘッド内の水抜き後，ドライヤーで乾燥させてヘリウム真空リークテストを行って漏水を確認した。

原因はヘッド部の溶接不良と純水による銅の侵食などの経年変化にあると想像される。これによりSD1は撤去された。また，スリット本体と接続するフレキシブル配管には，それぞれ3㎜厚の円形鉛板パッキンがスリット1基全体では8箇所，その他，本体内に口径の大きい鉛パッキンが2箇所，合計10箇所使用されており，純水により鉛が侵食され，1箇所あたり2年ほどで水漏れが起こり，長年多大なメンテナンス時間を割いてきた。2004年2月に，SD2－X及びYのフレキシブル配管を，鉛パッキンを使わない曲げ半径の小さいSUS製フレキシブル配管に改造更新した。配管取り付け位置もヘッドの駆動負荷にならないようなU字取り付けとした。スリット周辺の配管接続に使用しているテフロン・シールテープは粉状に材質が変化するために使用を最小限にとどめ，継ぎ手材はSUS製Swagelok接続とした。鉛パッキンを一切使わない新3系分析スリットSA3は，設置から7年間経過後も順調に稼動している。

●LDM（Large scale Deflection Magnetの略）の水漏れ修理ミスがあった。漏水調査をしないで接着剤を塗布したが漏れは止まらず，結局，接着剤を剥がして，2m長ファイバースコープによる漏れ個所捜索を行った。その結果，その先の手の届かない狭隘部分から漏れ出している事が解った。対策として，市販の自動車用ラジエーター漏れ止め材を循環させたところ，漏れ個所は閉塞した。現在までの2年間，水漏れはない。簡易補修剤としては有用であるが，植物繊維材で作られているので，放射線に対しては弱いであろう。

●リナック本体中央部，B2加速管入り口側の銅製コリメータから水漏れがあった。直接銅管を銀ロー接続しているが，その溶接部分の亀裂が原因である。真空を破ることができない，代替部品がない等の理由により接着剤塗布修理でしのいで来たが，漏水が止まらず，手を焼いてきた。2004年2月に行った修理方法は，以前の接着剤を全て剥がし，コリメータ内の水を抜き，ドライヤーで乾燥させ，亀裂箇所に2液性の配管修理用接着剤を塗布し，掃除機で配管内に接着剤を染込ませ，1昼夜乾燥固化させた後，通水した。まだ水漏れは起きていない。

●BF系のフロースイッチ，フローメータは殆ど，使用不能となっている。フラッパ式フローメータは前述のWG水系と同じ型式のもので，鉛パッキン材や真鍮製フラッパが循環純水に溶出している。

●ヘッダー及び連絡管にはSUS管が使用されており，そのフランジにはアルミ製波型パッキンが使われている。このパッキンが純水へ溶け出し，リークが多くなってきている。この漏水場所探査について，実験室内ではヘッダー管が床面のピット内に敷設されているため，放射線シールド用コンクリートブロックで塞がれている場所があり，漏水場所の特定が困難となっている。

3.2 純水補給系

市水から活性炭ろ過，イオン交換をして純水を製造し，各タンクに供給する装置である。製造能力は1トン/hの流量で10トン/cycleである。2年前にカートリッジ型純水器を導入した。常時使用する為にDual化してある。劇物薬品を使用しないことや，市水を入り口側に接続するだけで低導電率純水（0.1 μS/cm 以上）

が製造できる点や，排液が出ない点なども以前に比べて安全になった。

●原水タンクボールタップの波打ち現象により給水配管が振動し，タンクと配管とのプラスチック製接続部が割れて水漏れが起こった。現在，この接続部の材質を砲金製の金属にしてある。波打ちが起こらないよう給水管出口をタンク内の下部あるいは内壁面に沿わせて給水するような方式を検討中である。

§4．市水粗温調系

放射線に曝されない水系であり，市水を循環させている。冷水系と冷却塔水系（以後，タワー水系と呼ぶ。）に大別される。フィルター系を備えていないので，定期的なドレイン洗浄が必要である。

4.1 冷水系

10±1 ℃の温調水系で，圧力0.5 MPa，総流量 300L/min。加速管および，導波管温度制御用の冷水を発生させる。チラーは14年前に25～100％無段階能力可変式のスクリュー型に変更した。冷水系の主配管は鉄管で施工されているために，管内のサビ・コブの発生が著しく，早期更新が必要である。導電率管理をしていないので，目視判断により，２ヶ月に一度程度，水を置換している。

●これまで15年間，ノンメンテナンス，ノントラブルであったが，2004年８月に冷却器（蒸発器）内から冷媒及び潤滑油が漏れる故障が起こった。早期に発見することができ，また，幸いにも同型の冷却器の在庫品があり，１週間程度で回復することができた。現在フロン22使用のチラーは製造中止となっている。

4.2 電源室水系

後付けの水系で，冷水系から流量20L/min を分流して電源室蓄熱槽の冷却に寄与していて，一番保有水量の小さな水系である。配管は銅管で銀ロー接続されているが，配管経路が制御室内の各種の配線と同じピット内なので，水漏れ発生時にはその影響が大きい事が懸念される。配管接続方法，経路等を見直す必要がある。

●この槽内の熱交換器である銅管に2003年，数箇所の穴が開き，１次水側に漏れてオーバーフローしていた。原因としては，数年前に槽内に酸性洗浄剤を投与したことにより肉厚が薄くなった事が考えられる。

4.3 タワー水系（冷却塔水系）

循環水温は（20～30）±2 ℃（通常，22±2 ℃）で，圧力0.2MPa，循環水導電率800～1000 μS/cm。リナック及び GeV- γ 棟の負荷で発生した熱を最終的に屋外に放熱して各水系温度を適正値にしている。400冷却トンの開放型角型冷却塔に４年前更新した。2003年夏には薬注装置を更新し，薬液タンクを100 L と大型にした。ポンプと連動して動作し，薬液の滴下時間を調整できるので藻の発生の抑制などに役立っている。薬品はマルチ剤を使用している。

タワー水系の問題としては，開放型冷却塔であるためにどうしても粉塵の混入は避けられない。旧型の VAPODINE 装置（クライストロンのコレクタを冷却する装置で，蒸発冷却方式採用している。）は１，２，４号機で使われている。 1993年まで毎年この熱交換器内に付着した泥やカルシウム成分除去のための洗浄をしていたが，鋳鉄製熱交換器容器の内面が腐食して穴が開き，洗浄を止めている。また，この容器内面から剥離した鉄サビ片や外気粉塵が水系内を循環し，モジュレータ内のパルストランスや充電チョーク配管の流量計を詰まらせ，伝熱阻害を起こしている。2000年にモジュレータ周りの１インチ配管を，腐食やサビ・コブの発生しにくい塩化ビニールライニング鋼管に更新した。将来の目標としては，屋内熱負荷への粉塵混入を防ぐ為に，タワー水系をプレート型熱交換器で分離すれば，モジュレータやチラーへの清浄水の循環が可能となる。

●タワー水温度安定化のため３方向弁が備えてあるが，この温度制御サーモスタットの摺動抵抗部の磨耗による故障が２～3年に一度起こる。これは，タワー水温の制御温度設定幅が±1℃と狭く作動回数が多かった事が原因であり，現在は温度幅±2 ℃に設定している。３方向弁のセンサは，将来，可動部のない構造としたいと考えている。

●また，2004年５月に，14年間目で初めて，この３方弁のパッキンから漏水した。重工側制御盤の近くの天井付近に取り付けられているが，水滴が落ちたのは制御盤の脇の位置だったので大きな被害はなかった。３方弁パッキン周辺には，漏水防止用の水受け皿を付けた方が良いかも知れない。

●VAPODINE 装置（クライストロン冷却装置）は３号及び５号機の熱交換器を多管式からプレート式に更新した。３号機の冷却装置の２年間に起こった故障は２回，５号機は１回ある。３号機１回目は，2002年12月，アクリル製タンクの重合接着部から水漏れが発生した事がある。原因としては，WG 水系の40℃の循環水を，タンク内が空の状態から補給した事が何回かあった。これにより接着部が剥がれて漏水したものと想像する。現在は，10㎜厚の透明塩ビ製タンクに変更し，三角柱の補強材を付けて，以前より接着面積を大きく取り，その強度を増している。その後の水漏れはない。２回目は，2004年９月に装置タンクの水がオーバーフローした故障がある。これは水位センサの誤動作により給水電磁弁が給水継続状態となり発生したものである。調査の結果，センサ内部の半導体圧力計に接続してあるポリエチレン製の中空外気導入パイプが途中で折れていた為に，正確に大気圧と比較することができなくなり，実際の水圧より低い圧力と誤認してしまった事が解った。この大気導入パイプは４芯線の中心に配置されている電線であるが，配線中に曲げ半径を小さくした事が直接の原因である。

５号機の故障は，2004年２月に１次冷却水（純水）温度が上昇したことがあった。これはプレート熱交換器２次側タワー冷却水のストレーナメッシュの目詰まりによるものである事が解り，メッシュサイズを多少大きなものに変更した。

§5．制御系及び電源動力系

更新が一番遅れている場所である。制御盤は製作会社名から（三菱）重工側と電機側とに分かれていて，前者は加速管水系，後者は導波管及び BF 水系を制御している。各制御盤内には一部 PLC を導入したり，更新機器の制御は部分的に新しくなっているが，殆ど当時のリレー回路のままである。早急な更新が必要である。

30点温度記録計のデータや各リレーの接点を PC に取り込んで故障表示装置に表示しているが，OS が古くなり，時代に合わなくなってきたので，Ethernet対応の記録計を設置する予定である。まずは，各タンク水位レベルをリアルタイム計測し，異常な漏水による水位低下を検知し，水漏れ対策に一役買おうと思っている。

§6．最 後 に

BF 水系のアルミや鉛パッキン腐食やハンダ溶接部の問題あるいはタワー水系の分離などは現状予算措置で，一度に全数補修することは難しい。機器更新などは，共同利用運転の緊急性や将来的展望を見据えたリナックの再構築プランにより決定されると考えている。現在の課題として，大きな漏水が起こる確率は非常に高くなっているので，夜間時における突発的な水漏れに対する対策，冷却系故障時でもリナック運転者に頼らないで自動的にビーム OFF するなどの最低限の安全機能を作る必要がある。冷却系は，加速器の中でも，基本的なものの一つであり，常に万全にしておかなければならない。メンテナンスのコンセプトとして

は，ノンメンテナンスを目指し，また修理の容易性や修理時間の短縮，汎用品を使用する事などがある。まだまだ古い設備機器や配管が多いので，故障再発防止のための日常点検や原因究明はしっかりと確認するようにしている。

(LNS Experiment : #2455, #2472)

第２実験室床の荷重試験及び電子リナックのＡ部直線性の測量

高橋重伸，田中拓海，河合正之，浜 広幸

東北大学大学院理学研究科附属原子核理学研究施設
(982-0826 宮城県仙台市太白区三神峯1-2-1)

Weight Test of the Floor of the No.2 Experimental Room and Alignment of the A-part Acceleration Structures in the Linac

S. Takahashi, T. Tanaka, M. Kawai, and H. Hama

Laboratory of Nuclear Science, Tohoku University, Mikamine 1-2-1, Taihaku-ku, Sendai, 0982-0826

To extend the research work of the nuclear physics, a new spectrometer is demanded at the No.2 experimental room in the Laboratory of Nuclear Science (LNS) of the Tohoku University. The gross weight of the spectrometer is about 100 ton. However, the tolerable level to the weight which the floor has is 10 ton/m^2. The load to the floor becomes a problem of the accelerator alignment. Therefore, we gave temporary weighting of concrete blocks and verified the influence on the alignment of the STB ring. The measurements of the alignment of the magnets were done by comparing the levels of magnets before and after the loading from July to August, 2004.

In addition, the measurement of the straightness of the A-part of the accelerator structure of the linac was done. This measurement is preparation for the reorganization which is planned in the spring in 2005. The results are also reported here.

§1．概要

2004年７月にK0実験が終了した。この実験には５年前に旧東大核研から移管した総重量約35トンのTAG-X及びPILOT電磁石を第２実験室内の北側に設置し，使用していた。

STBリング（以下，リングと呼ぶ）による原子核実験の新研究課題を拓くために，同じ場所に総重量約100トンの新スペクトロメータの設置が要望されている。しかしながら，建設時の文献などによると，実験室床面の耐荷重は約10トン/㎡程度であると記載されている。この為に，2004年７月から８月の１ヶ月に亘って第２実験室内の北側に，総重量が110トンのコンクリートブロックを設置し，リング電磁石のレベルをその設置の前後で測量したので，その結果などについて述べる。また，2005年の春に予定されている電子リナックＡ部出口の改造にあたり，Ａ部加速管の直線性を測量する必要性が生じてきた。その測量の方法及び結果などについても述べる。第１図に核理研のレイアウトを示す。

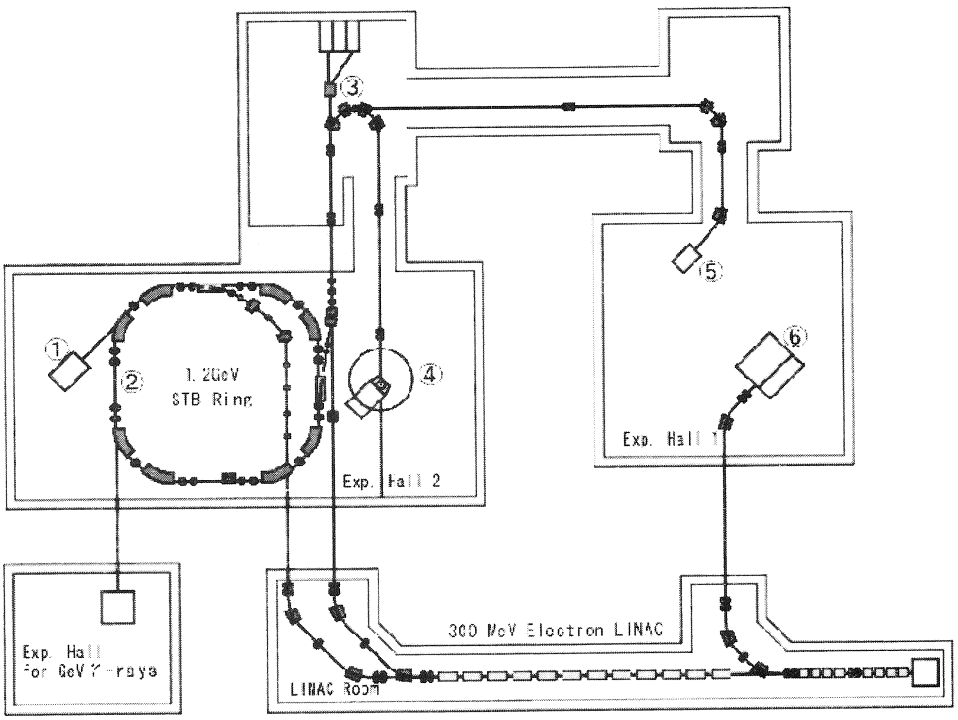

第１図　核理研のレイアウトを示す。重量110トンの新 NKS 電磁石設置予定箇所は第２実験室内の図の①の場所である。2004年７月にこの場所に110トン相当のコンクリートブロックを積み，約１ヶ月間放置し，その前後でレベル測量を行った。
　また，リナック A 部とは，電子銃出口の A１から A８までの加速管列の事で，通常60 MeV までの初段加速部を担っている。

§2．第２実験室の床面荷重試験について

第２図は第２実験室内の STB リング周辺を拡大したものである。コンクリートブロックを図中の斜線部分に設置し，リング電磁石のレベルをその設置の前後で測量したので，その結果などについて述べる。

QF５，QD５，BM５を包む点線の円は実験室建屋基礎から独立している部分を示す。壁上の黒い点は，測量用シールを貼った場所を示してある。

リングレベル測量の機材，方法については核理研報告Vol.34（2001年）に掲載された方法[1]とほぼ同じだが，鉄製の測量用ポール（３箇所で使用）に代わり，QUICKSET 社の TRIPOD（以後，QUICKSET と呼ぶ）を使用した[1]。第３図で，2002年のデータは GeV・γ棟実験室が第２実験室の北西側に隣接して建設された時期（2002年７月完成）であり，埋め戻しによる沈み込みの影響がリング北西アーク部のBM５からQF６にかけて，またその反作用である浮き上がりが実験室の南東側の BM２からQD･QF４のレベル差として現れている。2004年では北東側（QF３から QF４）が沈み，また南側直線部（QD８から QD１）が浮き上がって，重量物設置の影響がわずかに現れている様にも見えるが，測量誤差が0.1mm 程度あるところもあり，断定する事はできない。

第４図はリング北西部電磁石と周辺壁上測量シールのレベル変化を2004年の７月と８月で測量したものである。ここで，QNW は北壁，QWW は西壁のシールで，８月が少し沈んで見えるが，比較するデータの点数が少ない事や測量誤差が大きい事などから，床面変位を判定する事は難しい。

§3．荷重試験についての課題

1)　従来の鉄製測量用ポールは約100Kgと重量があるため，電磁石や真空ダクトにぶつけないよう，移動時

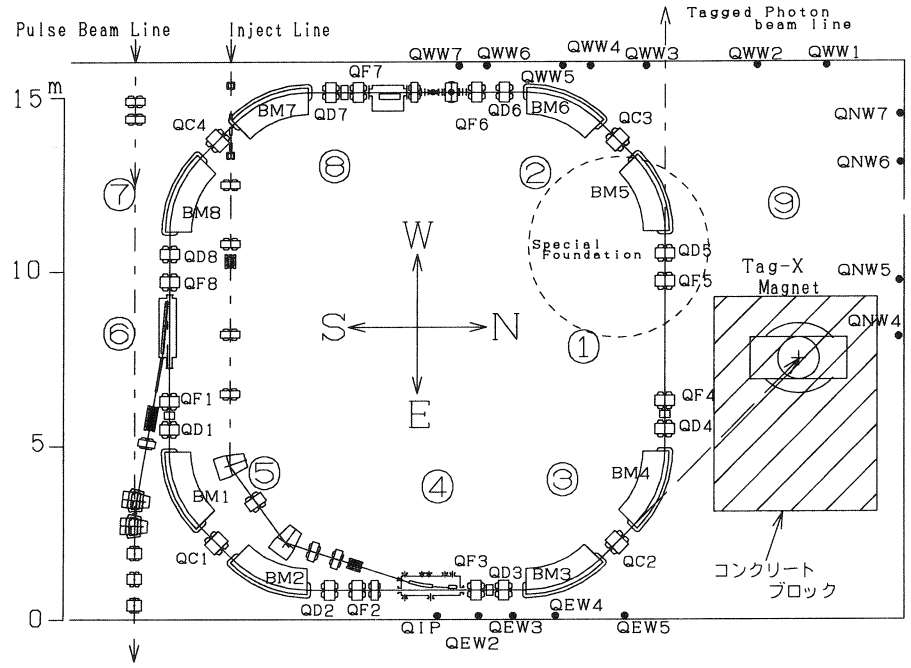

第２図　STB リング全周を測量するにはリング内６箇所，リング外２箇所に測量機をセットする。鉄製の測量用ポールは IM１付近の⑤と QD７付近の⑧にセットした。壁面レベル測量のために今回は⑨の位置にも測量機をセットした。QEW，QNW，QWW は壁面の高さ2.2m上に貼り付けた各測量用シール点の概略位置である。

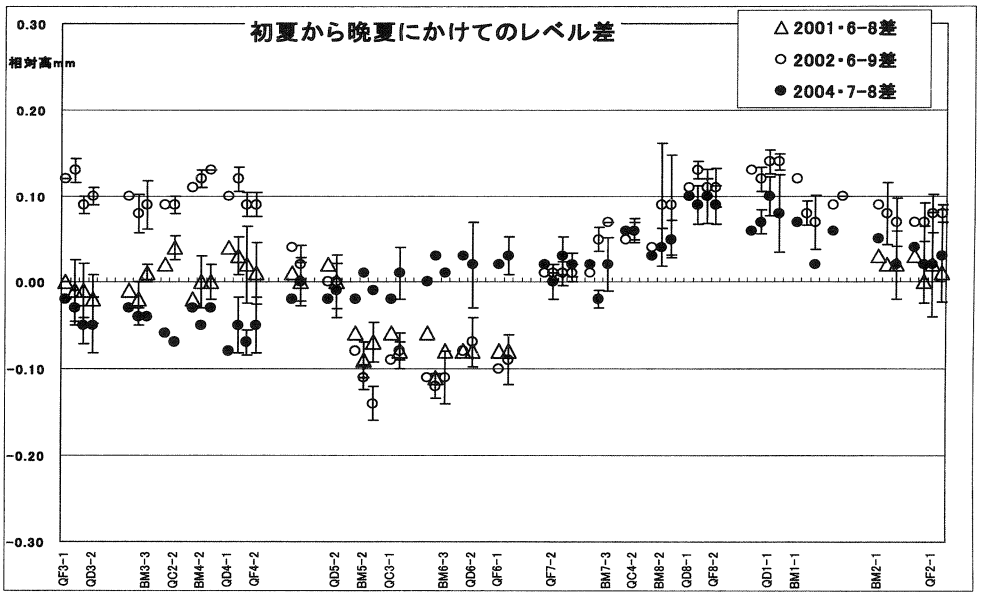

第３図　2001，2002，2004年の初夏から晩夏に亘るリングのレベル差を表示したものである。 2001年は QF７から QC１にかけてデータがない。2002年の１月から５月はGeV-γ棟の建設期間でレベル値の変動が大きく，床面レベルの動き方が例年とは逆方向になっている。2004年は微細ではあるが BM４周辺が沈下し QF８周辺が持ち上がっている。その差は約±0.1mmである。

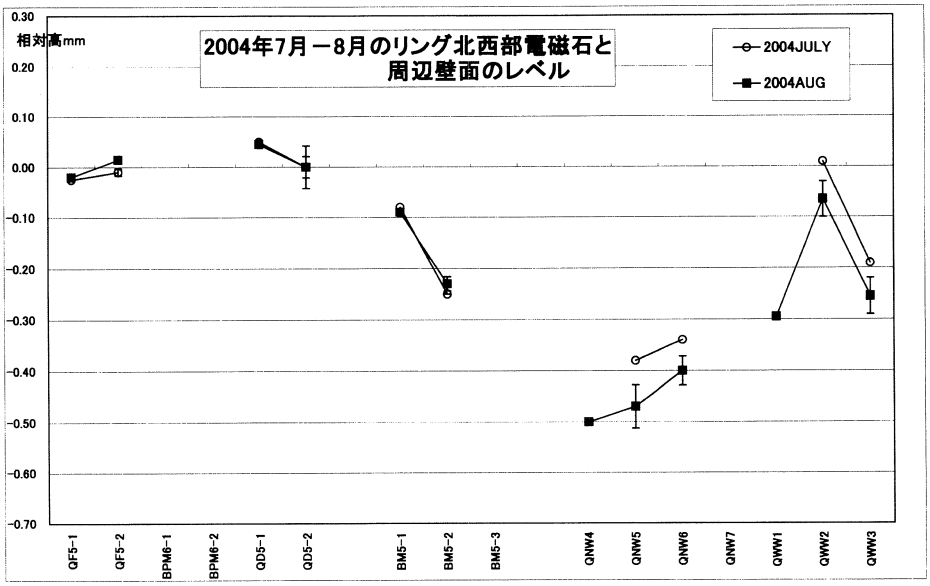

第４図　2004年の７月と８月にリング北西部と周囲壁面とのレベルを測量したデータである。壁上シールの誤差が多いのはシールの取り付けが悪い為に生じたものである。（基準点はQD５-２としてあり，QNWは北側壁面，QWWは西側壁面上の測量用シールのポイントである）

には注意を要するが，「QUICKSET」は前者に比べてブレが少なく移動や高さ調整が簡単である。欠点は，あまり軽量な為，測量者が誤って触ると再整準，再測量をしなければならないことである。これを防止する目的で，中心支柱下部に適当な鉛ブロックを下げて安定させた。今回は２種類の測量用三脚を使用する必要があった。

2)　2004年７，８月測量方法が今までと異なる点は，測量作業に７名の初心者が加わった事である。人手は増えたが，測量に関する個人差が大きい事や，狭い場所での測量にはデータの誤差が大きくなりやすい為に，一人で行う測量日数と同程度であった。また，レベルデータの繋ぎ合わせが難しくなり，再測量することもあった。作業日数の短縮化や誤差の減少を目指して，ウォーターレベルによるレベル測量も行っていきたいと考えている。

§4．リナックA部直線性の測量

ビーム強度の向上，本体室及びトランスポート系でのビームロスの低減，エミッタンスの測定，加速管列収斂系の改良のためのデータ収集，真空系の増強など，リナックの性能向上のために，来春，A部加速管（A1からA8までの加速管列を言う）下流側に電子ビーム診断装置を設置する予定である。この改造に当たり，A部加速管の直線性を確認する必要性が出てきた。Y軸については2002年に一度測量しているが，X軸方向の変位の測量については，初めての事で，現在手持ちの測量機器で，その測量の可能性を見つける事も目的であった。

X軸の測量機セットは，「QUICKSET」の上にNEWPORT社のXYステージとセオドライトを載せたものである。この測量機を，初め，電子銃高圧電源筐体の後部に設置した。ターゲットとして，第５図のアルミ製治具に600mm程度のA１製アングルを取り付けた治具（第６図の左側参照）を使用した。その先端部付近には測量用シールを貼り付けてあり，本体室通路側（電子銃側から見て加速管の西側）の加速管支持金具に押し当てた。治具押し当て面である加速管支持金具の面はアラインメント基準レールと接している面である。第７図に示したように，A１入り口側とA８出口側に交替で前記の馬型ターゲットを置きながらセオ

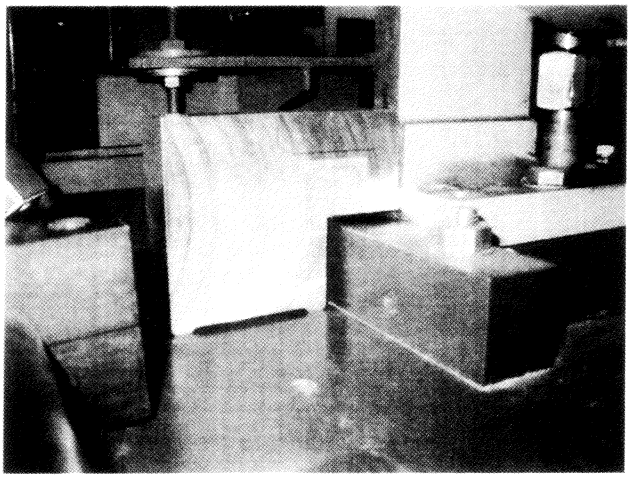

第５図　Ｘ軸変位測量のため使用された馬形をしたAl製治具。加速管アラインメント基準支柱に，この治具を押し付けて測量する。大きさは100mm×100mm×30mmである。

ドライト望遠鏡の視準軸を，その半固定の回転微調ネジとXYステージを動かしてターゲットに合わせて行くと軸出しができる。その後は各加速管の入り口及び出口側基準レールに接している支持金具に，順次馬型ターゲット治具を押し当て，Ｘステージを移動させて，このＡ１－Ａ８直線軸からの偏差を読み取る。
この測定を，Ａ部下流側からも同様にして行う。

Ｙ軸方向の測量機材は，前述のQUICKSETに，GPM３（平行平板マイクロメータ）を付けたライカ社のＮ２レベルを載せて，Ａ４，Ａ７，Ａ部下流側の３箇所に設置した。レベル用のターゲットは第６図の右側図のように，540mm長の鉄製角棒を使用し，500mmの位置に測量用シールを貼り，加速管定盤上支持支柱の近くの３点（西側２点，東側１点）に，この角棒を立てて測量した。

§５．Ａ部直線性の測量結果

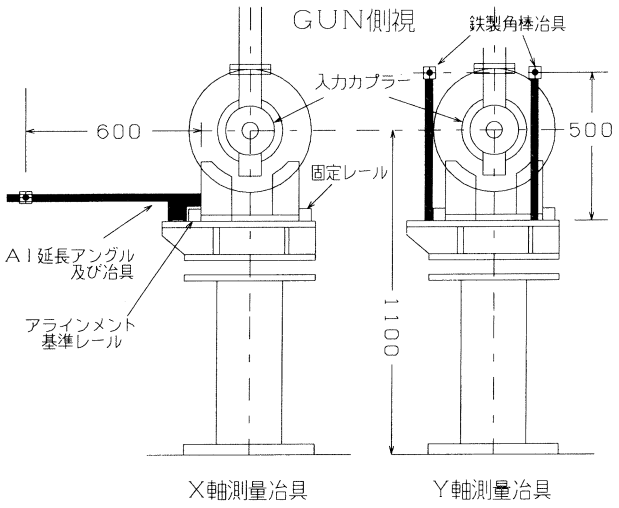

第６図　Ｘ軸，Ｙ軸の測量用治具の配置概念図。Ｘ軸用馬型治具には600mmの延長アングルを取り付けて，その先端にターゲットシールを貼り付けてある。Ｙ軸用治具は鉄製の500mm長の角棒で，先端の適当な位置に同様のシールを貼り付けて測量する。各治具は１台のみである。図は電子銃側から見ている。

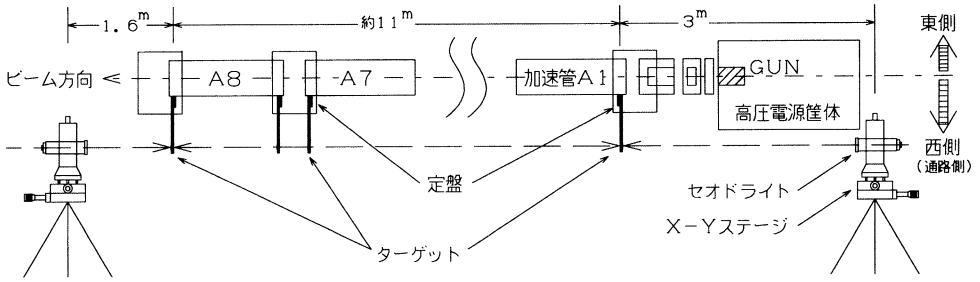

第７図　X 軸の測量方法。測量機１機を A 部の前後で置き換えて測量した。直線軸の軸出しは，A１入り口側と A８出口側にターゲットを置き，これらを交互に視準して合わせる。ターゲットを順次，基準アラインメント支持金具に接している加速管支柱に押し当て，X ステージのマイクロメータで A１－A８直線軸からの変位差を読み取る。

第８図，第９図にそれぞれ X 軸，Y 軸の直線性を示す。両図のゼロ点は，全ての測量点の重心を直線で当てはめた線である。S-band (2856MHz)，２π／３モードの加速管では通常，加速管のアラインメント許容値は±0.5mm以内とされており，この同心円内では電子ビームは一様に加速されると考えられている。第９図の Y 軸方向に関しては，A４から A７まで高くなっているが，ほぼ±0.5mm以内に入っており，また，２年前の測量値と比べて，ほとんど変化していない事が解った。この測量によって，A 部加速管のアラインメントを変更することなく，現在のままビーム診断装置の設置が可能である事がわかった。

§6．リナック直線性測量の課題

a)　当初は，加速管支持支柱の近くで X，Y 両軸同時に測量しようと思っていたが，後付の Q 電磁石架台，加速管取り付けの Q 電磁石の支持金具やモード変換器冷却配管などが遮り，また電子銃高圧電源の筐体があるため，測量機を加速管に近づけて設置する事が出来なかった。そのために，X，Y 軸の測量で別々の方法を取らざるを得なかった。今後は両軸同時測量をしたいと考えている。

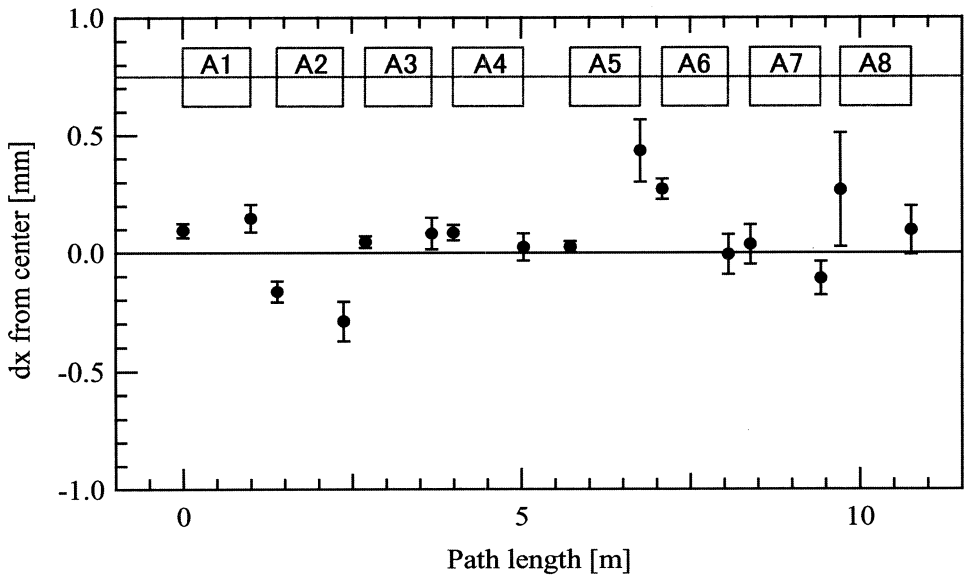

第８図　X 軸の直線性を示す。ゼロ点は X 軸の重心を直線でフィットしたものである。

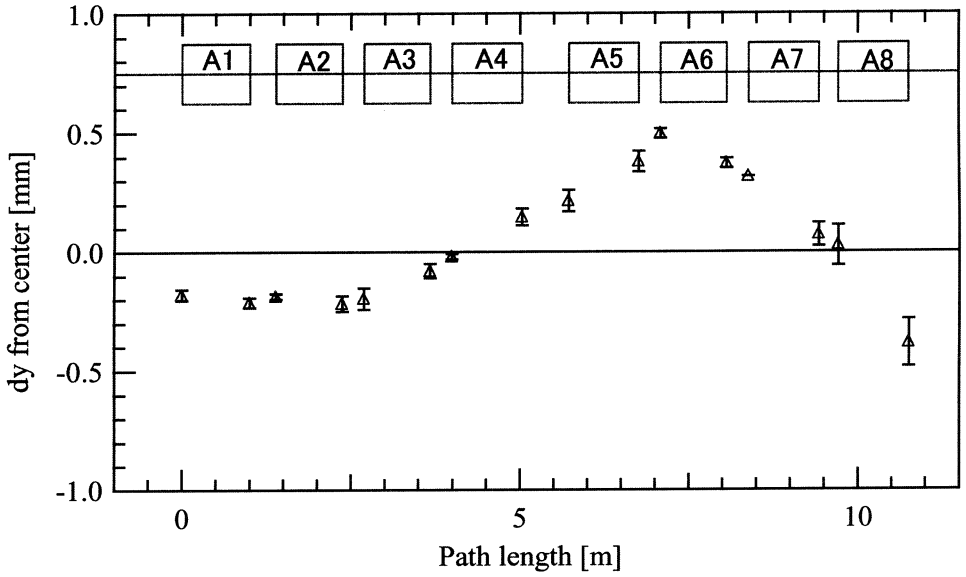

第９図　A 部加速管の Y 軸データ。加速管定盤上に540mm長の鉄製角棒たてて，適当な高さの位置に測量用シールを貼り付けて，かつ，レベル測量機を A 部の３箇所に移動して測量した。
　各点は，定盤東側と西側（通路側）の平均を取っている。2002年のデータとほぼ同じ結果であった。

b)　加速管定盤表面には長期使用により出来た凹凸があるため，フラットな位置を探して馬型治具や測量用棒をセットするのであるが，加速管を移動せずに測量するには，治具の製作など検討が必要である。

c)　測量日数の制限や測量者の被爆量の関係から A 部下流側のレベルデータ数が少なかった。

d)　A 部加速管列の Q 電磁石用の治具がないため，測量ができなかった。今後はこれらの電磁石も含めた再測量が，簡単に出来るようにする必要がある。

e)　建設当時の文献によれば「加速管アラインメント精度は架台が±0.1mm以内，加速管を含めた総合設置精度は±0.5mm以内に収めてあるため，架台アラインメントが狂わない限り加速管の分解組み立てが可能である。」と記されている [2]。しかし，その後38年経過し，加速管の入れ替えや地盤変動などにより，アラインメント基準枠が狂ってしまった疑いがある。これを検証する事も測量目的の一つであったが，大きな変位は見られなかった。リナック B 部の直線性測量についても考えているが，電磁石やその架台，スリットや導波管の配管等が遮っている事，あるいはまた，A 部より距離が２倍程度長い事等，現有機器での測量には検討が必要である。

謝　辞

本報告はリングの測量を手伝って頂いた，深澤宏司氏，縄　健一氏，本望雅志氏，鈴木耕拓氏，鈴木慎哉氏，岡村憲有氏，斉藤雄高氏ならびに加速管直線性測量用の治具を製作して頂いた松田一衛氏のご配慮，ご協力によるもので，深く感謝いたします。

参　考　文　献

[1]　核理研報告　Vol. 34. 2001

[2]　三菱電機技報　Vol. 42. 1968

IV. Status Report of LNS Accelerator Complex in 2003

Status Report of LNS Accelerator Complex in 2003

H. Hama, F. Hinode, A. Kurihara, M. Mutoh, M. Nanao, Y. Shibasaki, K. Shinto, and S. Takahashi

Laboratory of Nuclear Science, Tohoku University, 1-2-1 Mikamine, Taihaku-ku, Sendai 982-0826

Operation status of an electron accelerator complex in FY2003 at the Laboratory of Nuclear Science, Tohoku University is reported. Total user-time had reached 2800 hours (operation-time of accelerators was totally 3500 hours), which is probably the longest time of beam supply recorded in these years.

§ 1. Operation Statistics

After the stable operating point of the STB ring (1.2 GeV synchrotron) was established, the total operation time of the LNS accelerator complex has steadily increased. The total machine time reached up to ~2500 hours in FY'01 and FY'02. In FY'03, initially there was no long shut-off term was scheduled except a summer vacation. In addition, there was no serious machine trouble. As a result the electricity charge hit bottom of the budget, so that machine times of the high-energy operation in January and February in '04 were not scheduled. which is shown in Fig. 1.

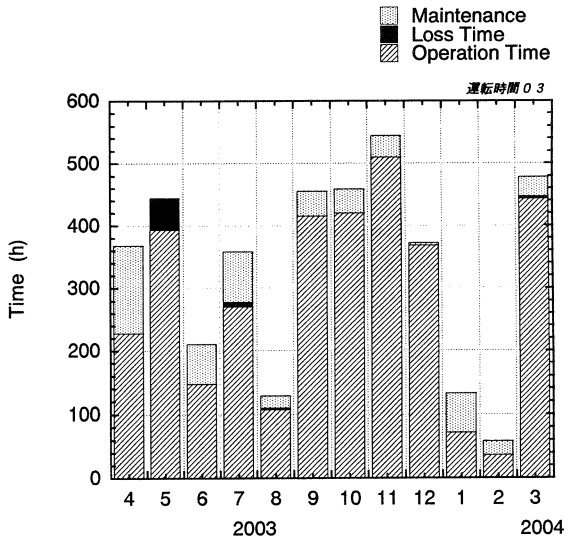

Fig.1. Time portion of the LNS accelerator complex for each month in FY2003.

Because of continuous effort for care of the 37-year-old linac and survey of efficient operating method, the accelerators have been working very well. It has to be pointed out that the total unscheduled shut-off time was drastically reduced to be 1.6 % of the total available machine time, which is only one tenth of that of FY'02. The most significant fact is that the nominal injection energy of the booster operation was reduced to be 150 MeV from the former one of 200 MeV. In other words, among five klystron modulators, one of those was usually not in duty. Consequently troubles on modulators happened frequently were always recovered by the back-up modulator, so that the net loss time has been able to be much reduced.

In Fig. 2, the portion of the linac operation mode in FY'03 is shown. It is clearly seen that the loss time due to the troubles was drastically decreased. Of course the reduction of the injection energy into

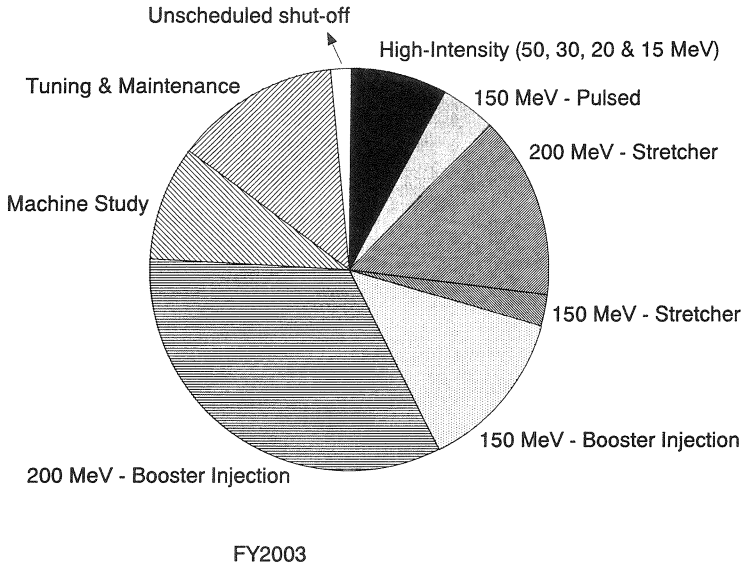

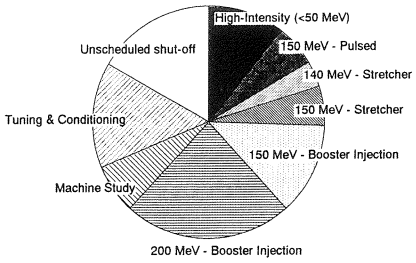

Fig.2. Shared time portion of each operating mode of the LNS linac integrated over the FY2003. The right hand one (small figure) is that of the FY2002

the STB ring brought not only advantages but caused difficulties in the machine operation.

Since the stabilities of the dipoles and the quadrupoles of the STB ring are relatively poor in the lower magnetic field region, the ripple of the betatron tunes is serious problem for efficient beam injection, and then very careful machine tuning has been always required.

§ 2. Major troubles

Serious troubles happened to the linac system are still frequent. Particularly the infrastructures (or the utilities) are no longer neatly working. Accordingly cooling water leaks and break-down of high voltage cables cause risks of long-term shut-off.

In the FY'03, in addition to such an everyday affair, a significant trouble occurred to a klystron modulator. Some resisters in the charging part were burned several times. We have not identified what was caused by, so that the investigation is still under way.

§ 3. Development

One of the specific features of the LNS linac performance is that the system can be operated at a very high repetition rate of 300 Hz. Although a severe BBU effect limits macropulse peak current of 80 mA at the high energy part, a higher beam current of ~ 200 mA with lower beam energies less than 50 MeV has been supplied for users. The consequent average beam current is approximately 150 μA, which is probably the highest current obtained from the present RF linacs in Japan. This very high intense beam is usually provided to user's applications based on the radioisotope production. However the required beam energy is certainly depending on the experiment purpose, so that the linac operating parameters has to be often changed. Detail of the low energy operation in FY'03 is shown in Table 1.

One may notice that the beam energy covers a very wide region. Because of stable operation of the injector part of the linac, we do not change any parameters for the 1st klystron modulator (K#1). Consequently the beam energy after passing the accelerating part of K#1 is ~ 25 MeV at the beam

Table 1 Shared time portion for various beam energies in the high-intensity and low-energy operation mode of the LNS linac in FY'03.

Beam Energy (MeV)	Operation Time (h)	Portion (%)
50	68.4	22
30	203.0	66
20	24.3	8
15	13.5	4

current of ~ 150 mA. Because the beam transport optics in the linac was not carefully considered, such a low energy beam cannot be transported properly to the exit of the low energy part of linac. For the lower energy operation below the practical maximum energy of 50 MeV, we need some beam deceleration in followed accelerating structures driven by K#2, which leads a complicate machine operation. In addition, larger beam emittance (~200 π mm mrad) and wider energy spread cause considerable beam loss in the transport line. Entire system of the LNS linac has to be improved for further progress of the use of the low-energy and high-intensity beam.

V. List of Publication

List of Publication（論文リスト）（2003.1～2003.12）

Papers Published in Refereed Journals

Radiation Damage of Silicon Microstrip Detectors by High Doses of 200 MeV Electrons.

T. Takahashi, M. Ukai, A. Yoshida, Y. Fujii, K. Dobashi, O. Hashimoto, K. Maeda, A. Miyamoto, T. Miyoshi, S.N. Nakamura, Y. Okayasu, T. Tamae, H. Tamura, K. Tsukada, and T. Watanabe

Nucl. Instr. and Meth. **A 511** (2003) 328-334.

Beam-Polarization Asymmetries for the $p(\gamma, K^+)\Lambda$ and $p(\gamma, K^+)\Sigma^0$ Reactions for E_γ = 1.5-2.4 GeV.

R. G. T. Zegers, M. Sumihama, D. S. Ahn, J. K. Ahn, H. Akimune, Y. Asano, W. C. Chang, S. Date, H. Ejiri, H. Fujimura, M. Fujiwara, K. Hicks, T. Hotta, K. Imai, T. Ishikawa, T. Iwata, H. Kawai, Z. Y. Kim, K. Kino, H. Kohri, N. Kumagai, S. Makino, T. Matsumura, N. Matsuoka, T. Mibe, K. Miwa, M. Miyabe, Y. Miyachi, M. Morita, N. Muramatsu, T. Nakano, M. Niiyama, M. Nomachi, Y. Ohashi, T. Ooba, H. Ohkuma, D. S. Oshuev, C. Rangacharyulu, A. Sakaguchi, T. Sasaki, P. M. Shagin, Y. Shiino, H. Shimizu, Y. Sugaya, H. Toyokawa, A. Wakai, C. W. Wang, S. C. Wang, K. Yonehara, T. Yorita, M. Yoshimura, and M. Yosoi

Phys. Rev. Lett. **91** (2003) 092001 (1-4).

Evidence for a Narrow S = +1 Baryon Resonance in Photoproduction from the Neutron.

T. Nakano, D. S. Ahn, J. K. Ahn, H. Akimune, Y. Asano, W. C. Chang, S. Date, H. Ejiri, H. Fujimura, M. Fujiwara, K. Hicks, T. Hotta, K. Imai, T. Ishikawa, T. Iwata, H. Kawai, Z. Y. Kim, K. Kino, H. Kohri, N. Kumagai, S. Makino, T. Matsumura, N. Matsuoka, T. Mibe, K. Miwa, M. Miyabe, Y. Miyachi, M. Morita, N. Muramatsu, M. Niiyama, M. Nomachi, Y. Ohashi, T. Ooba, H. Ohkuma, D. S. Oshuev, C. Rangacharyulu, A. Sakaguchi, T. Sasaki, P. M. Shagin, Y. Shiino, H. Shimizu, Y. Sugaya, M. Sumihama, H. Toyokawa, A. Wakai, C. W. Wang, S. C. Wang, K. Yonehara, T. Yorita, M. Yoshimura, M. Yosoi, and R. G. T. Zegers

Phys. Rev. Lett. **91** (2003) 012002 (1-4).

Separation of the Longitudinal and Transverse Cross Sections in the $^1H(e,eK^+)\Lambda$ and $^1H(e,eK^+)\Sigma^0$ Reactions.

R. M. Mohring, D. Abbott, A. Ahmidouch, Ts. A. Amatuni, P. Ambrozewicz, T. Angelescu, C. S. Armstrong, J. Arrington, K. Assamagan, S. Avery, K. Bailey, K. Beard, S. Beedoe, E. J. Beise, H. Breuer, R. Carlini, J. Cha, C. C. Chang, N. Chant, E. Cisbani, G. Collins, W. Cummings, S. Danagoulian, R. De Leo, F. Duncan, J. Dunne, D. Dutta, T. Eden, R. Ent, L. Eyraud, L. Ewell, M. Finn, T. Fortune, V. Frolov, S. Frullani, C. Furget, F. Garibaldi, D. Gaskell, D. F. Geesaman, P. Gueye, K. K. Gustafsson, J.-O. Hansen, M. Harvey, W. Hinton, E. Hungerford, M. Iodice, C. Jackson, C. Keppel, W. Kim, K. Kino, D. Koltenuk, S. Kox, L. Kramer, T. Leone, A. Lung, D. Mack, R. Madey, M. Maeda, S. Majewski, P. Markowitz, T. Mart, C. J. Martoff, D. Meekins, A. Mihul, J. Mitchell, H. Mkrtchyan, S. Mtingwa, I.

Niculescu, R. Perrino, D. Potterveld, J. W. Price, B. A. Raue, J.-S. Real, J. Reinhold, P. Roos, T. Saito, G. Savage, R. Sawafta, R. Sege S. Stepanyan, P. Stoler, V. Tadevosian, L. Tang, L. Teodorescu, T. Terasawa, H. Tsubota, G. M. Urciuoli, J. Volmer, W. Vulcan, T. P. Welch, R. Williams, S. Wood, C. Yan, and B. Zeidman

Phys. Rev. C **67** (2003) 055205 (1-16).

Threshold Electrodisintegration of ^{3}He.

R. S. Hicks, A. Hotta, S. Churchwell, X. Jiang, G. A. Peterson, J. Shaw, B. Asavapibhop, M. C. Berisso, P. E. Bosted, K. Burchesky, R. A. Miskimen, S. E. Rock, I. Nakagawa, T. Tamae, T. Suda, J. Golak, R. Skibinski, H. Witala, F. Casagrande, W. Turchinetz, A. Cichocki, K. Wang, W. Glokle, H. Kamada, T. Kobayashi, and A. Nogga,

Phys. Rev. C **67** (2003) 064004 (1-8).

Measurement of the Transverse-longitudinal Cross Sections in the $p(e,e'p)\pi^0$ Reaction in the Δ region.

C. Kunz, N.I. Kaloskamis, M.O. Distler, Z.-L. Zhou, R. Alarcon, D. Barkhuff, A.M. Bernstein, W. Bertozzi, J. Calarco, F. Casagrande, J. Chen, J. Comfort, G. Dodson, A. Dooley, K. Dow, M. Farkhondeh, S. Georgakopoulos, S. Gilad, R. Hicks, A. Hotta, X. Jiang, A. Karabarbounis, S. Kowalski, D.J. Margaziotis, C. Mertz, R. Miskimen, I. Nakagawa, C. N. Papanicolas, M.M. Pavan, G. Peterson, A. Ramirez, D. Rowntree, A.J. Sarty, J. Shaw, E. Six, N. Sparveris, S.-B. Soong, S. Stiliaris, T. Tamae, D. Tieger, C. Tschalaer, G. Tsentalovich, W. Turchinetz, C.E. Vellidis, G.A. Warren, S. Williamson, A. Young, J. Zhao, and T. Zwart

Phys. Lett. B **564** (2003) 21-26.

Alpha-decay from the 3.5 eV Isomer of ^{229}Th.

T. Mitsugashira, M. Hara, T. Ohtsuki, H. Huki, K. Takamiya, Y. Kasamatsu, A. Shinohara, H. Kikunaga, and T. Nakanishi,

J. Radioanal. Nucl. Chem. **255** (2003) 63-66.

Preparation of Carrier-free ^{7}Be Isotope by Means of an Ion-exchange Method Following Charged Particle and Photonuclear Reactions.

T. Ohtsuki, S.I. Fujikawa, and H. Yuki

App. Radiat. Isotope, **59** (2003) 221-223.

Two-phonon Giant Resonances in ^{136}Xe, ^{208}Pb, and ^{238}U.

K. Boretzky, A. Grunschloss, S. Ilievski, P. Adrich, T. Aumann, C.A. Bertulani, J. Cub, W. Dostal, B. Eberlein, T.W. Elze, H. Emling, M. Fallot, J. Holeczek, R. Holzmann, C. Kozhuharov, J.V. Kratz, R. Kulessa, Y. Leifels, A. Leistenschneider, E. Lubkiewicz, S. Mordechai, T. Ohtsuki, P. Reiter, H. Simon, K. Stelzer, J. Stroth, K. Summerer, A. Surowiec, E. Wajda, and W. Walus

Phys. Rev. C **68** (2003) 024317-(1-17).

Development of the Radiation Control System for Personal Permission, Status and Record.

A. Miyamoto, H. Yamazaki, H. Yuki, M. Nanao, Y. Sugawara, and T. Ohtsuki

Radioisotopes **52** (2003) 693-698.

Papers Published in International Conference Proceedings

S_{11}(1535) Resonance in Nuclei Studied with the C(γ, η) Reaction.

H. Yamazaki, T. Kinoshita, K. Kino, T. Nakabayashi, T. Katsuyama, A. Katoh, T. Terasawa, H. Shimizu, J. Kasagi, T. Takahashi, H. Kanda, K. Maeda, Y. Tajima, H.Y. Yoshida, T. Noma, Y. Aruga, A. Iijima, Y. Ito, T. Fujinoya,T. Yorita, K. Hirota, and O. Konno

Proceedings of the 9th International Conference on "the Structure of Baryons," Edited by C. Carlson and B. Mecking (World Scientific, 2003) 541-544.

S_{11}(1535) Resonance in Nuclei Studied via (γ, η) Reactions.

J. Kasagi

Prog. Theor. Phys. Supp. **149** (2003) 215-220.

Photoproduction of Neutral Kaons on C in the Threshold Region.

T. Takahashi, Y. Fujii, O. Hashimoto, K. Itoh, H. Kanda, M. Katoh, T. Kinoshita, O. Konno, K. Maeda, H. Miyase, K. Mizunuma, S.N. Nakamura, T. Osaka, A. Sasaki, T. Tamae, H. Tamura, T. Terasawa, H. Tsubota, K. Tsukada, M. Ukai, M. Wakamatsu, T. Watanabe, and H. Yamazaki

Nucl. Phys. **A 721** (2003) 991c-994c.

Photoproduction of Mesons on Nuclei at LNS.

H. Yamazaki, T. Kinoshita, A. Katoh, T. Katsuyama, K. Kino, T. Nakabayashi, H. Shimizu, T. Terasawa, J. Kasagi, H. Kanda, K. Maeda, T. Takahashi, Y. Aruga, T. Fujinoya, A. Iijima, Y. Ito, T. Noma, Y. Tajima, H.Y. Yoshida, K. Hirota, T. Yorita, and O. Konno

Proceeding of International Symposium on "Electrophoto-production of Strangeness on Nucleons and Nuclei (Sendai03)", Sendai, Japan, June 16-18, 2003, Edited by K. Maeda, H. Tamura, S.N. Nakamura, O. Hashimoto, (World Scientific) 191-197.

Photoproduction of Neutral Kaons in the Threshold Region at LNS-Tohoku.

T. Takahashi, K. Dobashi, Y. Fujii, O. Hashimoto, K. Itoh, H. Kanda, M. Katoh, K. Maeda, A. Matsumura, H. Miyase, T. Miyoshi, K. Mizunuma, Y. Miura, S.N. Nakamura, H. Nomura, Y. Okayasu, T. Osaka, M. Oyamada, H. Tamura, H. Tsubota, K. Tsukada, M. Ukai, H. Yamaguchi, M. Wakamatsu, T. Watanabe, T. Ishikawa, T. Kinoshita, F. Miyahara, H. Shimizu, T. Tamae, T. Terasawa, H. Yamazaki, O. Konno, S. Endo, A. Sasaki, and T. Satoh

Proceeding of International Symposium on "Electrophoto-production of Strangeness on Nucleons and Nuclei (Sendai03)", Sendai, Japan, June 16-18, 2003, Edited by K. Maeda, H. Tamura, S.N. Nakamura, O. Hashimoto, (World Scientific) 198-207.

New γ Beam Line at LNS Sendai

H. Shimizu

Proceeding of International Symposium on "Electrophoto-production of Strangeness on Nucleons and Nuclei (Sendai03)", Sendai, Japan, June 16-18, 2003, Edited by K. Maeda, H. Tamura, S.N. Nakamura, O. Hashimoto, (World Scientific) 301-312.

Comparison of the ^{12}C(e,e'p) Cross Sections at Low Momentum Transfer with a Relativistic Calculation.

T. Tamae,

EEP03: Internal Workshop Proceedings on "*Probing Nucleons and Nuclei via the (e,e'p) Reaction*", Grenoble, France, October 14-17, Edited by E. Voutier, J.-M. Laget, D.W. Higinboctham (2003) 103-109.

Search for Phenomena of Partial Restoration of Chiral Symmetry in a High Momentum-transfer Region.

H. Shimizu and T. Matsumura

YITP-RCNP Workshop on "Chiral Restoration in Nuclear Medium"

Prog. Theor. Phys. Suppl. **149** (2003) 112.

$2\pi^0$ Photoproduction Experiment at SPring-8.

T. Matsumura, J.K. Ahn, S. Date, M. Fujiwara, K. Hicks, T. Hotta, T. Ishikawa, J. Kasagi, H. Kawai, T. Kinoshita, H. Kohri, T. Mibe, M. Miyabe, N. Muramatsu, T. Nakabayashi, H. Nakamura, T. Nakano, M. Niiyama, Y. Ohashi, T. Ooba, D. Oshuev, C. Rangacharyulu, P.M. Shagin, Y. Shiino, Y. Sugaya, M. Sumihama, Y. Tajima, H. Yamazaki, T. Yorita, H.Y. Yoshida, R.G.T. Zegers, and H. Shimizu

Nucl. Phys. **A 721** (2003) 723c-726c.

Review

固体金属中の核融合：金属は核反応の特殊環境か？

笠木治郎太，結城秀行

日本物理学会誌 (BUTSURI)，**58** (2003) 190-194.

放射性同位元素をプローブとしてフラーレンに異原子挿入の可能性を探る.

大槻勤，大野かおる

アイソトープニュース（日本アイソトープ協会）**11** (2003) 2-8.

光核反応を用いた放射化学的研究(東北大学原子核理学研究施設).

大槻　勤

放射化分析 **15** (2003) 3-19.

VI. Approved Experiments

平成15年度前期採択課題一覧表

課題番号	課　　題　　名	申込責任者	採　択 シフト数
原子核関連分野			
2481	V系光子標識化装置エネルギー更正	前田　和茂	8
2482	CCD の電子線による放射線損傷の研究(2)	杉本　康博	4
放射光関連分野			
2483	フォトニック結晶からのスミス・パーセル放射スペクトル測定	近藤　泰洋	4
2484	Coherent TR による Prebunched FEL の基礎研究(5) －矩形閉鎖共振器その２－	柴田　行男	4
放射化学・物性関連分野			
2485	長寿命放射性核種の環境中移行における基礎化学反応研究	関根　　勉	2
2486	銅中の Be の拡散	藤川辰一郎	1
2487	宇宙化学的試料および環境試料の光量子放射化分析	海老原　充	2
2488	ファイバアンプ用ガラス中の軽元素の光量子放射化分析	鹿野　弘二	1
2489	標識化による金属内包フラーレン及びヘテロフラーレンの研究及びその応用	大槻　　勤	2
2490	^{229m}Th 及び ^{146}Smの製造と壊変特性の研究	中西　　孝	2
2491	電子ビームによるフリーラジカル生成の研究	結城　秀行	1
2492	Th-229m の製造とその崩壊特性	三頭　聡明	1
2493	金属及び半導体材料中の軽元素の定量のための分離・補集法の開発	桝本　和義	2

平成15年度後期採択課題一覧表

課題番号	課題名	申込責任者	採択シフト数
原子核関連分野			
2494	$2\pi^0$ photo-production in nuclei	清水　肇	10
放射光関連分野			
2495	Prebunched FEL の基礎研究(6)　コヒーレント放射の可干渉性	柴田　行男	4
2496	フォトニック結晶からのスミス・パーセル放射スペクトル測定(2)	近藤　泰洋	8
放射化学・物性関連分野			
2497	長寿命放射性核種の環境中移行における基礎化学反応研究	関根　勉	2
2498	ファイバアンプ用ガラス中の軽元素の光量子放射化分析	鹿野　弘二	1
2499	標識化による金属内包フラーレン及びヘテロフラーレンの研究及びその応用	大槻　勤	3
2500	金属及び半導体材料中の軽元素の定量のための分離・捕集法の開発	桝本　和義	2
2501	宇宙化学的試料および環境試料の光量子放射化分析	海老原　充	3
2502	^{229m}Th 及び ^{146}Sm の製造と壊変特性の研究	中西　孝	1
2503	Th-229m の製造とその崩壊特性	三頭　聰明	2
2504	電子ビームによるフリーラジカル生成の研究	結城　秀行	1
2505	銅における不純物拡散	藤川辰一郎	1

核理研研究報告　第37巻

2004年11月発行

発行所　東北大学大学院理学研究科
附属原子核理学研究施設
仙台市太白区三神峯1-2-1（郵便番号982－0826）
電話　022－743－3400

印刷所　株式会社　東北プリント
仙台市青葉区立町24番24号
TEL　022（263）1166㈹

RESEARCH REPORT OF
LABORATORY OF NUCLEAR SCIENCE
TOHOKU UNIVERSITY

Volume 37 November 2004

Laboratory of Nuclear Science, Tohoku University,
1-2-1, Mikamine, Taihaku, Sendai 982-0826, Japan

東北大学大学院理学研究科

原 子 核 理 学 研 究 施 設